THE ATOMIC MASS DEPENDENCE OF MASSIVE MUON PAIR PRODUCTION IN 225 GeV/c π^--NUCLEUS INTERACTIONS

BY

MORRIS L. SWARTZ

MARCH, 1984

THE UNIVERSITY OF CHICAGO

THE ATOMIC MASS DEPENDENCE OF MASSIVE MUON PAIR PRODUCTION IN 225 GeV/c π^--NUCLEUS INTERACTIONS

A DISSERTATION SUBMITTED TO
THE FACULTY OF THE DIVISION OF THE PHYSICAL SCIENCES
IN CANDIDACY FOR THE DEGREE OF
DOCTOR OF PHILOSOPHY

DEPARTMENT OF PHYSICS

BY

MORRIS L. SWARTZ

CHICAGO, ILLINOIS

MARCH, 1984

ACKNOWLEDGEMENTS

Modern high energy physics experiments are endeavors that require the efforts and skills of many people. The research that is presented within this document is no exception. Foremost among those sharing the credit (and the blame) for this work are my collaborators: Henry Frisch, Herb Greenlee, Carla Grosso-Pilcher, Kurtis Johnson, Mac Mestayer, Pierre Piroué, Bernard Pope, Lindsay Schachinger, Mel Shochet, David Stickland, and Dick Sumner. It is with great pleasure that I thank them for their hard work, for their many insights and suggestions, and for their good humor (most of the time). Several others deserve mention for their contributions. Nikos Giokaris and Jim Green both contributed to the planning and construction of the experiment. Chuck Whitmer was involved in both the planning of the experiment and the data acquisition. Gail Hansen worked with the group during the Spring 1981 data acquisition period. And Ryan Rohm was involved in detector simulation studies.

The experiment was blessed with exceptional technical support. I wish to thank Ken Stanfield, John Hawkins, Al Guthke, Ron Currier, Age Visser, and the staff of the Fermilab Proton Department for their very professional help in the construction of the apparatus and the operation of the P-West beam. The detector components were designed and built at Chicago and Princeton. Many thanks are due Dick Armstrong, Sollie Lucero, Richard Northrop, Rudy Gabriel, Robert (Archie) Ryan, Larry Fiscelli, and the late Cliff Brill of the EFI Engineering Services Group. Harold Sanders and the staff of the EFI Electronics Development Group deserve both thanks and praise for some truly outstanding work.

I also wish to thank Ann David, Marius Isaila, Howard Edwards, and the staff of the Elementary Particles Laboratory at Princeton.

Mel Shochet was my thesis sponsor and I thank him for his guidance, for his many helpful suggestions, and for my knowledge of Solid State Physics. His careful reading of this document and constructive comments have improved it in both form and content. This document has also benefited from many suggestions by Henry Frisch and I thank him for them.

Last, but not least, I thank Kathy Visak for typing this dissertation and for help with the rather formidable task of assembling it into its final form.

TABLE OF CONTENTS

LIST OF TABLES

LIST OF ILLUSTRATIONS

ABSTRACT

The production of massive muon pairs in 225 GeV/c π^--nucleus interactions has been studied for four nuclear targets. The dependence of the integrated cross section on atomic mass A was measured by comparing the relative cross sections for the targets. If one assumes that the cross section is proportional to A^{α}, a value of $\alpha = 1.00 \pm 0.06$ for muon pair masses between 4.0 GeV/c^2 and 8.5 GeV/c^2 was obtained. The Drell-Yan model predicts an additional dependence of the cross section on the proton fraction Z/A. If one parametizes the integrated cross section as $\sigma(Z/A)A^{\alpha'}$ where $\sigma(Z/A)$ is a function of the proton fraction that includes the effects of the Drell-Yan model, Fermi Motion, and secondary pion production, a value of $\alpha' = 0.97 \pm 0.06$ was obtained.

The dependence of the muon pair transverse momentum distribution on nuclear size was also investigated. The second moment of the distribution $\langle P_T^2 \rangle$ was found to be consistent with being independent of nuclear size. If the dependence of $\langle P_T^2 \rangle$ on nuclear size is parametized as $\langle P_T^2 \rangle = a + b\, A^{1/3}$ the coefficient b was found to be less than 0.015 GeV^2/c^2 with 90% confidence.

CHAPTER I

INTRODUCTION

The Drell-Yan Model

The first lepton pair experiment was performed at the Brookhaven Alternating Gradient Synchrotron in 1969 by a Columbia Brookhaven collaboration.[1] The experiment was a search for intermediate vector bosons and heavy vector mesons via the reaction

$$p + U \Rightarrow \mu^+ + \mu^- + \text{anything}$$

Among the mysterious results of the experiment was the presence of a continuum of muon pair masses ranging from 1 to 6.7 GeV/c^2. The following year, a parton model motivated explanation was published by Drell and Yan.[2] Their model attributed the muon pair continuum to the electromagnetic annihilation of quarks and antiquarks in the beam and target hadrons. A number of the features of the Drell-Yan model have since been confirmed by several experiments.[3] It is well established that electromagnetic production is responsible for the muon pair continuum at masses above 4 GeV/c^2. The Drell-Yan model fails to account for other aspects of the continuum. It appears that these "failures" are due to the simplicity of the parton model approach and that strong interaction corrections may account for all experimental observations. The deviations of the muon pair continuum from the expectations of the

simple model have attracted a great deal of interest as a means of testing the current theory of strong interactions, Quantum Chromodynamics (QCD). The hadronic production of lepton pairs (generically referred to as the Drell-Yan process) is the experimentally cleanest process used to test QCD with initial state hadrons.

The Drell-Yan model for the process

$$A + B \Rightarrow \mu^+ + \mu^- + X$$

is shown diagramatically in Figure 1. The momenta of the beam and target hadrons are labelled P_A and P_B, respectively. The variables x_A and x_B are the longitudinal momentum fractions of the annihilating quarks. The transverse momenta of the annihilating quarks relative to the hadron directions are represented as $\vec{k}_T^A$ and $\vec{k}_T^B$. The scale of the intrinsic quark momenta is given by the uncertainty principle as

$$|\vec{k}_T| \sim \hbar/r_h \qquad (1)$$

where r_h is a typical hadron size ~ 1 fermi. Therefore, one would expect that the intrinsic quark transverse momenta to be of the order of 200 MeV/c. The longitudinal quark momenta (in the hadron center of mass) required to produce muon pairs of mass 4 GeV/c^2 or more are at least an order of magnitude larger than the intrinsic transverse momenta. The intrinsic transverse momenta can therefore be neglected when calculating muon pair kinematic quantities. In this approximation, one can write the invariant mass squared, M^2, as

$$M^2 = s\, x_A\, x_B \qquad (2)$$

where $\sqrt{s}$ is the center of mass energy of the hadronic system. The Feynman scaling variable of the muon pair, x_F, can be written as

$$x_F \equiv P_{\parallel}^*/P_{\parallel max}^* = x_A - x_B \tag{3}$$

where $P_{\parallel}^*$ is the longitudinal momentum of the muon pair in the hadron center of mass frame and $P_{\parallel max}^*$ is the maximum P* that is kinematically allowed. The differential cross section (integrated over lepton pair center of mass angles) for the process shown in Figure 1 is

$$\frac{d^4\sigma}{dM^2 dx_F d^2P_T} = \frac{4\pi\alpha^2}{3M^4[x_F^2 + 4M^2/s]^{1/2}} \sum_i 1/3\ Q_i^2 \int d^2k_T^A d^2k_T^B\ [x_A\ \bar{q}_i^A\ (x_A, \vec{k}_T^{A2})$$

$$x_B q_i^B(x_B, \vec{k}_T^{B2}) + (A \leftrightarrow B)]\delta^2(\vec{k}_T^A + \vec{k}_T^B - \vec{P}_T) \tag{4}$$

The quantities in equation 4 are as follows: $\vec{P}_T$ is the muon pair transverse momentum relative to the beam direction; the sum over the index i indicates a sum over quark flavors; Q_i is the charge (in units of e) of the ith quark flavor; the functions $q_i(x, \vec{k}_T^2)$ and $\bar{q}_i(x, \vec{k}_T^2)$ are probability distributions of finding a quark or antiquark of flavor i with momentum fraction x and transverse momentum $\vec{k}_T^2$ in each of the hadrons. Equation 4 is usually presented in a P_T integrated form,

$$\frac{d^2\sigma}{dM^2 dx_F} = \frac{4\pi\alpha^2}{3M^4[x_F^2+4M^2/s]^{1/2}} \sum_i 1/3 Q_i^2 [x_A \bar{q}_i^A(x_A) x_B q_i^B(x_B) + x_A q_i^A(x_A) x_B \bar{q}_i^B(x_B)] \tag{5}$$

where the quark structure functions are defined as

$$q_i(x) = \int d^2k_T\ q_i\ (x, \vec{k}_T^2). \tag{6}$$

Several features of equations 4 and 5 are worthy of mention. The factor Q_i^2 has been multiplied by a factor of 1/3. This is necessary because the constituent quarks manifest the color degree of freedom. The probability that any annihilating quark-antiquark pair forms a color singlet (necessary for electromagnetic processes) is 1/3. Equation 4 implies that the muon pair transverse momentum distribution should

reflect the intrinsic transverse momentum distributions of the constituent quarks. It follows from a simple calculation that the mean square of the muon pair transverse momenta, $\langle P_T^2 \rangle$, should be related to the mean squares of the quark transverse momenta, $\langle k_T^2 \rangle$,

$$\langle P_T^2 \rangle = \langle k_T^{A2} \rangle + \langle k_T^{B2} \rangle \tag{7}$$

By the estimate given above, one would expect that $\langle P_T^2 \rangle$ should be of the order of 0.1 GeV^2/c^2 at most. The structure functions defined by equation 6 are, within the context of the parton model, functions of the dimensionless scaling variable x only. One can, therefore, integrate equation 5 over x_F and write the result as

$$M^3 \frac{d\sigma}{dM} = F(M^2/s) \tag{8}$$

The quantity $M^3 d\sigma/dM$ is expected to scale as some function F of the quantity $\tau = M^2/s$.

It is convenient, at this point, to specialize equation 5 to a particular hadronic initial state. The process

$$\pi^- + N \Rightarrow \mu^+ + \mu^- + X$$

where N is a nucleon will be considered. It is customary to regard each hadron as consisting of valence quarks and a "sea" of virtual quark-antiquark pairs. Only up, down, and strange quarks will be considered (the heavier quark flavors are present in the sea but have smaller probability of interacting due to their large mass). It is also assumed that the sea distributions are flavor SU(3) symmetric (u, d, and s sea quarks have the same probability distribution). Isospin invariance enables one to relate the valence quark probability distributions of the proton and neutron. If $u^p(x)$, $d^p(x)$, $u^n(x)$, and $d^n(x)$ are the up and

down quark structure functions of the proton and neutron, respectively, one can write that

$$xu^p(x) = xd^n(x) = U(x)$$
$$xd^p(x) = xu^n(x) = D(x) \tag{9}$$

Similarly, isospin and charge conjugation invariance require the equality of the pion valence structure functions $\bar{u}^\pi(x)$ and $d^\pi(x)$

$$x\bar{u}^\pi(x) = xd^\pi(x) = V_\pi(x) \tag{10}$$

Note that the new structure functions $U(x)$, $D(x)$, and $V_\pi(x)$ have been defined to include a factor of x. They are therefore momentum distributions and not number distributions. Consider the generic nucleon N as part of some nucleus having atomic number Z and atomic mass A. The probability that N is a proton is the ratio Z/A. Equation 5 can then be written as

$$\frac{d^2\sigma}{dM^2dx_F} = \frac{4\pi\alpha^2}{9M^4[x_F^2 + 4\tau]^{1/2}} [V_\pi(x_A)G_N(x_B) + S_\pi(x_A)H_N(x_B)] \tag{11}$$

where: $S_\pi(x)$ is the pion sea quark momentum distribution; the functions $G_N(x)$ and $H_N(x)$ are defined as

$$G_N(x) = \frac{1}{9}[4\frac{Z}{A}U(x) + 4(1-\frac{Z}{A})D(x) + 5\ S_N(x)]$$
$$H_N(x) = \frac{1}{9}[(1 + 3\frac{Z}{A})U(x) + (4 - 3\frac{Z}{A})D(x) + 12\ S_N(x)] \tag{12}$$

and $S_N(x)$ is the nucleon sea quark momentum distribution. The Drell-Yan model is based on the same parton model ideas that had been previously applied to deep inelastic charged lepton and neutrino scattering. It is not surprising then, that the nucleon structure functions $G_N(x)$ and $H_N(x)$ are closely related to the deep inelastic nucleon structure function $F_2(x)$. Using the same approximations made above, the deep

inelastic structure functions are

$$F_2^{\ell N}(x) = \frac{1}{9}\left[\left(1+3\,\frac{Z}{A}\right) U(x) + \left(4 - 3\,\frac{Z}{A}\right) D(x) + 12\, S_N(x)\right]$$
$$F_2^{\nu N}(x) = U(x) + D(x) + 6\, S_N(x) \qquad (13)$$

where $F_2^{\ell N}(x)$ is the structure function for charged lepton scattering and $F_2^{\nu N}(x)$ is that for neutrino scattering. Note that the structure function for charged lepton deep inelastic scattering is exactly the same function as that which interacts with the pion sea in the Drell-Yan model (i.e. $F_2^{\ell N}(x) = H_N(x)$). The pion and nucleon quark structure functions have been measured by a number of groups.[4-5] It is sufficient for the purposes of this document to state that the measured structure functions are in good agreement with theoretical expectations. The results of one such determination are listed in Table 1.[6]

In practice, muon pair experiments are usually performed with heavy nuclear targets rather than nucleon targets. One might ask how equation 11 should be modified for this case. It is customary to multiply nucleon cross sections by the atomic mass number raised to some power

$$\sigma(\text{nucleus}) = \sigma(\text{nucleon})A^{\alpha} \qquad (14)$$

where α is some exponent. The choice of the power α is certainly not obvious. It is well established[7] that at low P_T, hadronic final state processes scale with atomic mass as $A^{2/3}$. This has the simple interpretation that the incident hadron "sees" the projected area of an opaque nucleus. On the other hand, hard scattering processes such as the high transverse momentum production of single hadrons[8] and jets[9] scale in atomic mass with exponents significantly larger than 1. This behavior,

though not well understood, is probably due to multiple interactions or collective effects. The naivest expectations for the Drell-Yan process would be to ignore both nuclear absorption and possible collective effects and to assume that all quarks in the nucleus are exposed to the same flux of beam quarks. Actually, these assumptions are probably not that naive. The collective effects that have been observed in large P_T, hadronic processes occur with cross sections that are as small or smaller than the electromagnetic Drell-Yan cross section. Therefore, the probability that some sort of collective hadronic process occurs followed by an annihilation into a photon is vanishingly small. The screening of nuclear interiors by surface nucleons seems, at first glance, to be a large effect. The total hadron-nucleus cross section is larger than the projected area of the nucleus. One should keep in mind, however, that strong interactions do not absorb the quarks in the incident hadron. There is some evidence that the hadronization distance for quarks in high energy hadron-nucleus collisions is comparable to the size of the nucleus.[10] A physical picture of a typical low P_T collision is as follows. The quarks in the beam particle scatter softly once or several times as they pass through the target nucleus. Since most of the collisions are soft, the quarks retain most of their incident momenta even though they may be slightly off shell. The quark-antiquark luminosity is therefore essentially unchanged as the hadron and nucleus pass through each other. The Drell-Yan cross section should then scale with the number of quarks in the nucleus or linearly in A. Applying equation 14 to equation 11, the cross section for $\pi^- A \Rightarrow \mu^+ \mu^- X$ is

$$\frac{d^2\sigma}{dM^2 dx_F} = \frac{4\pi\alpha^2}{9M^4[x_F^2 + 4\tau]^{1/2}} [V_\pi(x_A)\, G_N(x_B, \frac{Z}{A}) + S_\pi(x_A)\, H_N(x_B, \frac{Z}{A})]\, A^{\alpha'} \quad (15)$$

where Z is the atomic number and α' is expected to be 1.

The Drell-Yan model, as outlined above, confronts experiment with varying degrees of success. Measurements of the nucleon structure functions are consistent with those measured in deep inelastic scattering experiments. The M^2/s scaling of the mass spectrum (see equation 8) has been verified at the 5% level.[3,11] The lepton pair center of mass angular distributions (not mentioned above in the interest of brevity and lack of pertinence to this work) are in excellent agreement with the expectations of the model.[12] Indeed, they are the most persuasive evidence for the electromagnetic production mechanism. The measured transverse momentum distributions are not in accord with the expectations of the model.[13] It has been observed that the mean square of the P_T^2 distribution is typically 1.5 to 2.0 GeV^2/c^2, about an order magnitude larger than expectations. The mean square of the distribution also seems linear in the square of the hadron center of mass energy,[14]

$$\langle P_T^2 \rangle = a + bs \quad (16)$$

where $a = 0.59\ GeV^2/c^2$ and $b = 2.3 \times 10^{-3}$. This observation contradicts the idea that the lepton pair P_T is due to the intrinsic transverse momenta of the annihilating quarks and implies a dynamical origin of the observed spectrum. Finally, the normalization of the Drell-Yan cross section seems in doubt. In early 1981, at the time that this work was begun, normalized measurements of the high mass muon pair continuum had been published by two groups. One group, the Chicago-Illinois-Princeton

collaboration,[15] had measured an anomalous A dependence exponent of $\alpha = 1.12 \pm 0.05$. Using this value to convert their nuclear cross section into a nucleon cross section, they found a result that was consistent with the Drell-Yan model. The other group, the CERN NA3 collaboration,[16] found an A dependence exponent of $\alpha = 1.00 \pm 0.02$ and a normalization of the nucleon cross section that was larger than the predictions of the model by a factor of 2.2 ± 0.4. It should be noted that the nuclear cross sections measured by the two groups were in agreement. The normalization discrepancy was due to the values of α used in the extraction of the nucleon cross sections. More recently, a number of groups have measured the normalized cross section for continuum muon pair production with various beams and targets and all find the Drell-Yan model too small by a factor of 1.5 to 2.5 (with typical systematic uncertainties of 0.4).[17]

QCD Corrections

The successes of the Drell-Yan model have lead theorists to conclude that its failures are due to the simplicity of the approach rather than any fundamental flaw. It is natural then to attempt to extend the model by the application of the only known theory of strong interactions, QCD. QCD treats the quark color degree of freedom as a dynamical SU(3) charge. The theory is just the unbroken $SU(3)_{color}$ Yang-Mills gauge theory and contains 8 vector gauge fields, the gluons. The strong coupling nature of the theory makes the calculation of static hadron properties extraordinarily difficult. However, the non-Abelian nature of the theory leads to a running coupling constant that becomes effectively smaller at large momentum transfers. This feature,

known as asymptotic freedom, leads to the hope that a perturbation expansion might converge at high energy. The standard renormalization group expression for the strong coupling constant is

$$\alpha_s(q^2) = \frac{12\pi}{(33-2f)\ \ln\ (q^2/\Lambda^2)} \tag{17}$$

where: q^2 = four momentum transfer squared; f is the number of quark flavors; and Λ is the energy scale of the q^2 evolution (Λ has been determined by measurement to be in the range 10 to 500 MeV). For q equal to typical muon pair masses and Λ taken to be 200 MeV, α_s is in the range 0.2 to 0.3. It is therefore conceivable that perturbative QCD has some validity. Using the work of Politzer,[18] Sachrajda[19] has shown that all QCD corrections can be absorbed into the structure functions in leading log approximation. In this treatment, the QCD perturbation series for equation 5,

$$M^4\frac{d^2\sigma}{dM^2dx_F} = F_o(\tau, x_F) + F_1(\tau, x_F, M^2)\ \alpha_s + F_2(\tau, x_F, M^2)\ \alpha_s^2 + \ldots \tag{18}$$

is further approximated by expanding each coefficient in a power series in $\ln(M^2/\Lambda^2)$,

$$F_n(\tau, x_F, M^2) = a_n(\tau, x_F)\ \ln^n(M^2/\Lambda^2) + b_n(\tau, x_F)\ \ln^{n-1}(M^2/\Lambda^2) + \ldots \tag{19}$$

and retaining only the leading term in equation 19. The quark structure functions acquire the same scale breaking terms that deep inelastic structure functions acquire in QCD (with the identification $|Q^2_{dis}| = M^2$). Therefore, equation 5 can be rewritten as

$$M^4\frac{d^2\sigma}{dM^2dx_F} = \frac{4\pi\alpha^2}{9[x_F^2 + 4\tau]^{1/2}} \sum_i Q_i^2 [x_A \bar{q}_i^A(x_A, M^2)\ x_B q_i^B(x_B, M^2) + (A\leftrightarrow B)] \tag{20}$$

It is clear from equation 20 that the prediction of scaling is expected to be violated. However, the violations are expected to be small for most of the data in existence. The value of x_B is typically of order $M/\sqrt{s} \sim 0.2$ to 0.25, the kinematic region in which the deep inelastic structure functions show essentially no scaling violation.

The leading log treatment of the Drell-Yan process does not address the normalization problem alluded to above. The next to leading log terms can be included, to first order in α_s, by calculating the lowest order QCD diagrams (see Figure 2). The calculation has been performed[20] and, for small τ, the result is

$$\frac{d\sigma}{dM^2} = \left(\frac{d\sigma}{dM^2}\right)_{\text{leading log}} \left[1 + \frac{\alpha_s}{2\pi} \frac{4}{3} \pi^2\right] + \ldots \qquad (21)$$

The correction to the leading log cross section is quite large, a factor 1.63 for $\alpha_s = 0.3$. It has been suggested by some[21] that the terms in square brackets in equation 21 form the lowest order part of an exponential series. This, however, remains to be proven. The standard representation for the effect of higher order log terms on equation 20 is

$$\frac{d^2\sigma}{dM^2 dx_F} = K(\tau, x_F, s) \left(\frac{d^2\sigma}{dM^2 dx_F}\right)_{\text{leading log}} \qquad (22)$$

where K seems to be of order 2 and is a weak function of the parameters in the region of τ, x_F space away from kinematic boundaries.

The first order diagrams shown in Figure 2 have also been used to calculate the P_T spectrum for the Drell-Yan process.[22] The calculations diverge at $P_T = 0$ and must be combined with the intrinsic quark k_T distributions to "regularize" the low P_T behavior. This procedure yields the form of the observed scaling of $\langle P_T^2 \rangle$ with s (see equation 16)

but encounters two difficulties. The first problem is that the normalization of this first order QCD calculation seems low by about a factor of 2.[23] Second order calculations[24] renormalize the first order result by a new factor K' ~ 2. However even with the second order corrections, the second difficulty remains. Enormous values of the quark intrinsic transverse momenta are required to fit the data.[25] Most analyses require $\langle k_T^2 \rangle$ to be about 1 GeV^2/c^2. This is in sharp contrast with expectations and indicates that low order perturbative approaches are not adequate to describe the P_T distribution in the observed range (P_T between 0 and 5 GeV/c).

A new class of QCD corrections has recently been studied by Bodwin, Brodsky, and Lepage (BBL).[26] These corrections, referred to collectively as initial stage interactions, involve gluon exchanges between the annihilating (active) quarks and spectator quarks present in the beam particle-target nucleus system. An example of one such process is shown diagramatically in Figure 3. These corrections have a number of interesting consequences. The form of the Drell-Yan cross section, equation 22, remains valid with one important adjoinder. The structure functions in equation 22 are not the same structure functions as those that describe deep inelastic scattering. This is a statement of "weak factorization" and is a theoretical matter of some controversy. It is claimed by other authors[27] that such corrections do not alter the apparently process independent nature of the structure functions (strong factorization). Another prediction of BBL is that initial state interactions with spectators within the active hadrons introduce color correlations between the active quarks. The effect is to increase the

normalization of the cross section by as much as a factor of 9. This is another possible source of the normalization discrepancy bewteen experiment and the simple Drell-Yan model. The normalization correction is expected to be strongly mass dependent and to vanish at large lepton pair masses ($M > 10$ GeV/c^2). The physical picture expounded by BBL is a formalization of the heuristic explanation of the linear A dependence given earlier. The incident beam quark is viewed as undergoing multiple soft interactions with the hadronic matter of the target nucleus. Since the collisions are soft, the quark is more or less on shell and its longitudinal momentum distribution is not strongly affected. Therefore, one expects a more or less linear A dependence of the P_T integrated cross section. The multiple soft collisions are expected to broaden the lepton pair P_T distribution. This effect is expected to scale linearly with the size of the target nucleus,

$$\delta\langle P_T^2\rangle \cong \lambda^2 A^{1/3} \tag{23}$$

where λ is estimated to be in range 100 to 500 MeV/c.

The physical picture treated more or less formally by BBL also serves as the basis of a phenomenological quark multiple scattering model by Michael and Wilk.[28] Their model has been developed as an explanation of the anomalous A dependence of high P_T hadronic processes. When applied to the Drell-Yan process, the authors expect a nearly linear A dependence of the P_T integrated cross section. Like the BBL prediction, the second moment of the P_T distribution is expected to increase with $A^{1/3}$. The dependence of $\langle P_T^2\rangle$ on $A^{1/3}$ is not exactly linear but can be approximated by equation 23 with λ = 200 MeV/c.

The predictions of the dependence of $\langle P_T \rangle$ on nuclear size are very accessible to experimental test. In the BBL publication, the authors have analyzed the published data of the Chicago-Illinois-Princeton collaboration and find "good" agreement with their expectations. Michael and Wilk have analyzed data from the Columbia-Fermilab-Stony Brook collaboration and are similarly gratified by the results. Published values of $\langle P_T^2 \rangle$ measured on H_2 and Pt targets by the CERN NA3 collaboration[29] show no such effect.

Fermilab Experiment 326

This document reports on some of the results of a high sensitivity muon pair search performed by a Chicago-Princeton collaboration at the Fermi National Accelerator Laboratory. This experiment, FNAL Experiment 326, studied the high mass muon pair continuum produced in the process

$$\pi^- + A \Rightarrow \mu^+ + \mu^- + X$$

where A was usually a heavy nuclear target (tungsten to be precise). Some of the running during the Spring 1981 run was devoted to muon pair production on several "short" nuclear targets of varying atomic mass. The remainder of this document describes an analysis of those data.

The motivations for such a study were described above. The A dependence of the Drell-Yan cross section which was somewhat controversial, has interesting physical implications both as a phenomenon in it's own right and as it affects the normalization of nucleon cross sections extracted from data on heavy nuclear targets. In addition, the dependence of the mean square of the transverse momentum distribu-

tion upon nuclear size has implications on the relative significance of initial state corrections to the Drell-Yan process. It is, therefore, important input into the factorization controversy and on the origins of the normalization corrections to the theory.

The work that follows is organized into three chapters. Chapter II contains a description of the apparatus used to perform the measurements. Chapter III describes the techniques used to reconstruct the muon pair signal and separate it from background. And finally, Chapter IV describes how the signal was converted into results of physical interest.

CHAPTER II

THE EXPERIMENT

The experiment was performed in the Proton West High Intensity Area of the Fermi National Accelerator Laboratory. The apparatus is shown in Figure 4. A high-intensity beam of negatively charged pions was focused on one of several nuclear targets. A 48-foot-long magnetic spectrometer was located immediately downstream of the target. The spectrometer consisted of a steel collimator followed by seven solid iron toroidal magnets. The gap between each pair of magnets was instrumented with a scintillation counter hodoscope and four planes of drift proportional chambers. A 20 milliradian conical vacuum pipe transported the non-interacted beam and the target produced hadronic debris through the center of the spectrometer to a dump located downstream of the apparatus.

Muons produced in the target were identified by penetration through at least four magnet modules (the probability for a hadron to traverse this much iron, approximately 30 absorption lengths, without interacting is about 1×10^{-14}). As the muons moved through the spectrometer, they were deflected by the azimuthal magnetic field. The negative particles were focused toward the spectrometer axis and the positive particles were defocused away from the axis. The scintillation hodoscopes were used to determine that an event had occurred. The drift chambers provided precision measurements of the particle trajectories

and, thereby, of the muon momentum vectors.

Each of the major detector components is described below.

The Beam

This experiment utilized the Proton West high-intensity charged hadron beam. A layout of the 740-foot-long beam line is shown in Figure 5. The following is a schematic description of the beam line function (a more complete description exists elsewhere).[30] A 400 GeV/c primary proton beam was extracted from the Fermilab Main Ring synchrotron and transported about one mile to the beryllium production target shown in the figure. Charged hadrons produced in the forward direction were accepted by a dipole magnet immediately downstream of the production target and focused by a quadrupole triplet onto a momentum selection slit (a large steel collimator). The momentum selected hadrons were transported downstream by a one-to-one imaging system (known as a FODO channel) consisting of three dipole bending magnets and four quadrupole focusing magnets. A second quadrupole triplet was then used to focus the beam onto the E326 experimental target. The magnetic fields in the beam line elements were adjusted to transport 225 GeV/c negatively charged hadrons. The result of a Monte Carlo calculation[31] of the beam momentum spectrum is shown in Figure 6. The beam actually had a central momentum of 221 GeV/c and a width of 20 GeV/c FWHM. The yield of secondary hadrons was measured to be approximately 3×10^{-4} particles/incident proton. The beam size at the experimental target was typically 0.3 inches FWHM in the horizontal dimension and 0.5 inches FWHM in the vertical dimension. The beam composition was never measured but has

been inferred from the measurements of others.[32] The beam was calculated to consist of approximately 94.7% pions, 4.7% kaons, and 0.7% anti-protons. The beam was also accompanied by a considerable muon "halo". Since iron is nearly transparent to high energy muons, off momentum muons were transported through the iron yokes and flux returns of the beam line elements (even wrong sign muons accompanied the beam). The dominant sources of the muon background were the decay of low momentum pions and kaons near the production target and the decay of on-momentum pions in the beam. A system of ten spoiler magnets was used to reduce the halo flux impinging on the spectrometer from about 10% of the total hadron flux to about 1% of the total hadron flux. The number of on-momentum muons actually transported with the hadron flux was about 0.1% of the total flux (this is trivially estimated from the pion lifetime, the length of the beam line, and the momentum acceptance of the beam).

In actual operation, the accelerator delivered a one second spill of 2-4 X 10^{12} protons every ten to fifteen seconds. This produced a secondary beam of 0.5-1.0 X 10^{9} particles per spill, 60% of which was incident on the experimental target. The particle flux was not uniform in time but was produced with the accelerator time structure of two nano-second "RF" buckets repeated every 18.3 nanoseconds during the one second spill.

The beam was monitored each pulse with a number of devices. The profiles and positions of both the primary proton beam and the secondary hadron beam were measured with segmented wire ionization chambers (referred to as SWIC's). The primary proton beam intensity was provided by two secondary emission monitors (SEM's). The integrated secondary

beam intensity was measured by two cylindrical ionization chambers (IC's). The ionization chambers, IC710 and IC711/712/713, were located immediately upstream of the experimental target. The upstream chamber, IC710, integrated the entire beam flux passing through a four inch diameter circular area. The downstream chamber, IC711/712/713, had a segmented anode which integrated the beam flux passing through three concentric rings with radii from 0 in. to 0.25 in., from 0.25 in. to 0.75 in., and from 0.75 in. to 2.0 in. The ionization chambers were calibrated by several techniques. Since the absolute calibration was not required for the work presented within this document, the reader is referred to Reference 30 for an excellent account of that work. The beam flux that was incident upon the experimental target was directly measured by the innermost channel of IC711/712/713. A second monitor was provided by two scintillation counter telescopes (referred to as Monitor East, ME, and Monitor West, MW) which viewed the target from 90 degrees with respect to the beam direction and counted large angle, target produced charged particles and photons. Finally, the beam spill quality was monitored by scaling the accidental coincidence rate of signals from Monitor East and a single scintillation counter (referred to as JOE) located about 150 feet downstream of the spectrometer.

The Targets

One of the aims of this experiment was to investigate nuclear effects in the production of massive muon pairs. Four nuclear targets were chosen to sample the entire periodic table: beryllium; copper; tin; and tungsten. The targets were 0.5 inch diameter solid cylinders of

varying lengths. They were mounted in a remote transporter which enabled one to change targets with essentially no loss of beam time. The measured target densities are presented in Table 2. As shown in the table, the measured densities agree well with published[33] values for all targets except tungsten. The tungsten target was composed of a sintered material in which tungsten crystals were bound in a matrix composed chiefly of nickel (some iron and copper were also present). Using published values for pure tungsten and nickel, one can infer that the composition of the target material was 94.3% tungsten and 5.7% nickel. The target lengths were chosen to be approximately 0.5 nuclear absorption lengths. This minimized systematic differences in beam absorption and spectrometer acceptance.

The Magnets

The main component of the spectrometer was the seven module iron toroidal magnet. The general specifications of each module are presented in Table 3. The upstream two magnets were 56 inch long cylinders of radii 24 inches and 35 inches, respectively. The downstream five magnets were octagonal prisms built from C magnets that were once part of the Brookhaven Cosmotron. Each magnet was approximately 56 inches in length and had major and minor radii of 51 inches and 47 inches, respectively. In order to accomodate the central conical vacuum pipe, the inner radii of the seven magnets increased from 2.5 inches for the most upstream module to 15 inches for the most downstream module.

Each module was constructed with an array of 4 in. x 8 in. magnetic induction loops embedded in its midplane. The radial and

longitudinal shape of the magnetic field was measured by integrating the voltage induced in each loop as the field direction in each module was reversed. The field was also calculated by numerically solving Laplace's equation with the appropriate boundary conditions and with measured values of the magnetic permeability of the Cosmotron iron. The measurements and calculations were consistent to within 2%. The field varied from approximately 23 kG. near the inside of TM1 to 15.5 kG. near the outside edges of the 5 Cosmotron magnets. The field had little longitudinal variation and radial components were small everywhere except very near the octagonal corners of the downstream magnets.

The Trigger Hodoscopes

The spectrometer was triggered with information from seven scintillation counter hodoscopes. The hodoscopes were mounted on magnetic shield plates attached to the upstream faces of magnet modules TM2, A, B, C, D, E, and the iron backscatter shield downstream of module E. Each hodoscope was segmented azimuthally into eight octants (following the symmetry of the Cosmotron magnets) and radially into a varying number of elements. The specifications of each counter plane are presented in Table 4. Figure 7 is a representation of the arrangement of the forty counters in the third plane. The octants were numbered from one to eight starting with the top octant and proceeding clockwise as one faced downstream. The radial elements were numbered from one starting with the counters nearest the vacuum pipe and proceeding radially outward. Each of the trapezoidal counters was machined from 0.25 inch thick Nuclear Enterprises #110 plastic scintillator. The

counters were viewed through long lucite light guides by Amperex 2232B or 56AVP photomultiplier tubes. The high voltage to each PMT base was adjusted to produce a signal of 75 mV into 50 ohms when the counter was illuminated by photons from a Co60 source.

The Veto Hodoscopes

The dominant source of trigger background was the intense muon halo that accompanied the beam. The accidental trigger rate was reduced, somewhat, by the inclusion of information from two upstream veto hodoscopes in the trigger (at a small price in spectrometer livetime). Muons that were moving parallel to the beam axis and fired counters in both hodoscopes were not allowed to trigger the spectrometer. Since the distribution of the halo muons was concentrated on the west side of the beam line, the 12 in. x 18 in. hodoscopes were located 6 inches to the west of the beam axis. Each array consisted of four 4.5 in. x 12 in. scintillation counters that were constructed from the same materials as the trigger counters. As is shown in Figure 8, the hodoscopes were located 20 feet and 32 feet upstream of the experimental target. For future reference, the upstream counters were labelled HU1 through HU4 and the downstream counters were labelled HD1 through HD4.

The Trigger

One of the technical challenges involved in operating an experiment to detect final state muons in a secondary hadron beam is the rejection of the muon halo that invariably accompanies such a beam. The

experiment utilized a beam of 5 X 10^8 to 1 X 10^9 secondary hadrons per second. Even with special muon spoiler magnets, a beam associated muon flux of 5 X 10^6 to 1 X 10^7 particles per second was incident on the spectrometer. Since the rate of interesting events under these conditions was less than one per spill, it was advantageous to build an apparatus that "saw" only target produced muons. Figures 9 and 10 are pictures of a real event and of an accidental coincidence of two halo muons. Represented are cross-sectional slices of two octants of the spectrometer. Fitted muon tracks are drawn as solid curves with drift chamber hits represented as single lines or asterisks and struck scintillation counters as darkened rectangles. In the former figure, the muon tracks originate in the target and enter the spectrometer at "large" angles with respect to the beam axis (at least 30 milliradians). The muon tracks shown in the latter figure enter the spectrometer essentially parallel to the spectrometer axis and are well removed from the experimental target. Detection of this class of events was suppressed greatly by the use of a selective hardware trigger.[34]

A block diagram of the trigger is shown in Figure 11. Signals from each of the 273 scintillation counters were discriminated by fast ECL discriminators (30 mV threshold) and split three ways. A 10 nanosecond wide pulse was distributed to a multiplexor channel for scaling, a 100 nanosecond delay line, and the first level trigger logic. The first level trigger used information from the first four hodoscope planes to make a fast decision on the presence of "target" muons in any of a preset list of octant permutations. It operated at the full 53 MHz RF bucket frequency of the beam without incurring any deadtime. It was the

function of the first level trigger to reduce the raw accidental coincidence rate to a level manageable by a more sophisticated second level trigger and to provide precise timing information to the drift chamber electronics. If the first level trigger was satisfied, the discriminated counter information that had been stored in the 100 nanosecond delay lines was latched. The output of the first level trigger was also used to form a logical AND with information from the veto hodoscopes. If a veto was present, the latches and first level trigger were reset. If no veto was present, a stop pulse was sent to the drift chamber encoding system and the second level trigger was started. The second level trigger utilized latch information from all seven hodoscope planes and was somewhat more powerful than the first level trigger. If the latched counter information indicated that the first level trigger had indeed been caused by a valid muon pair, the data acquisition computer was interrupted and all event related information was logged on magnetic tape. If the event was rejected by the second level trigger, the trigger logic and drift chamber encoding system were reset.

The first level trigger consisted of twenty-four fast coincidence matrices and a device referred to as the post matrix logic or PML. The matrices for one spectrometer octant are shown schematically in Figure 12. Each matrix was an 8 X 8 set of ECL coincidence gates, each of which could be independently enabled under computer control. There were three such matrices for each octant of the spectrometer. The first matrix, M12, required coincidences of signals from the plane 1 discriminators with those from the plane 2 discriminators. Since there were five counters in each octant of plane 1 and seven counters in each plane 2

octant, there were thirty-five possible coincidence combinations. A Monte Carlo simulation indicated that particles originating in the experimental target could fire only sixteen of the thirty-five combinations. The sixteen allowed combinations are indicated by circles in Figure 12 and, of course, were the only combinations that were enabled in actual operation. The second matrix, M23, formed coincidences of the seven plane 2 counters with the five plane 3 counters of each octant. The Monte Carlo indicated that target associated tracks could satisfy nineteen of the thirty-five combinations which are, again, indicated by circles in Figure 12. The third matrix, M4, formed coincidences of the plane 4 counters with a set of inputs that were permanently turned on. The effect was to form the logical "OR" of all plane 4 counters. The output signals from all twenty-four coincidence matrices were processed by the post matrix logic which is shown schematically in Figure 13. The three matrix outputs from each octant were connected to a triple input coincidence gate forming the logical "AND", M12*M23*M4. This was the definition of a muon for the first level trigger. The outputs from each of the octant AND gates were used to form an 8-bit address for a 256 X 1-bit random access memory. Each permutation of 0 to 8 octants having valid muons therefore addressed a different memory cell in the RAM. If an addressed memory cell contained a digital 1, the circuit produced a trigger. In practice, all octant permutations of two or more muons were accepted. Two types of trigger signals were produced. One type was synchronized to the RF signal from the accelerator to provide precise timing for the drift chamber encoding system. The second type was a latched level requiring an external reset.

A diagram of the veto hodoscope logic is shown in Figure 14. The signal from each of the four upstream counters was required to be coincident with its downstream counterpart. This selected particles travelling parallel to the beam axis. The 12 foot separation of the two hodoscope planes insured that particles travelling backwards from the experimental target would generate signals that were out of time by twice the flight path (24 nanoseconds). The output signals from the four coincidence gates were logically "OR"ed and the resulting signal was used in the trigger logic as shown in Figure 11.

A schematic diagram of the second level trigger is presented in Figure 15. It consisted of two parts, the trigger processor and the final decision logic. The trigger processor was nothing more than a hardware lookup table. There were thrity-four trigger counter latches for each octant of the spectrometer. While the number of mathematical permutations of thirty-four two-state objects is enormous (2^{34} > 17 billion), the number of counter permutations corresponding to target produced tracks of any angles and momentum is fairly small, 291 to be exact. The trigger processor functioned by comparing each of the 291 patterns to the actual pattern of latched counters in an octant. The processor analyzed all 8 octants in parallel. It consisted of a control unit, a 1024-word X 32-bit memory, and eight comparison/latch cards. The 291 patterns were stored in the memory module. Since legal patterns contained at most one counter latch per hodoscope plane, it was possible to store a pattern in 21 rather than 34 bits. The remaining 11 bits of the trigger processor memory word were used to store information about each pattern. The muon charge associated with the pattern was usually

unique. Three of the 11 information bits were used to indicate the charge as positive, negative or ambiguous. Patterns corresponding to very large transverse momentum (P_T) muons were flagged with a fourth bit. The seven remaining information bits were used to assign a sequence number to each pattern. In actual operation, the memory was loaded with the set of 291 patterns before a data run. The patterns were sequenced such that the most desirable patterns (the longest and largest P_T) were the last to be addressed. If the first level trigger was satisfied and no veto was present, the control module received a start pulse. It proceeded to sequentially address all patterns in the memory. As each pattern was addressed, the 21 pattern bits were simultaneously applied to one input of the eight comparison cards and the information bits were similarly applied to an 11-bit latch located on each card. If the pattern was matched by the 34 data bits for that octant, the 11-bit information word was stored. A pattern match required that all counters that were part of the pattern be present in the data but not the converse. In this way, additional struck counters did not cause trigger inefficiencies. After all 291 trigger patterns had been cycled, the information latches contained the 11-bit characteristic word for the last and most "desirable" match, if any. The control unit then signalled the final decision logic to examine the contents of the eight information latches. The final decision logic was programmable and flexible in its requirements (similar to the PML). In practice, it was always set to require that pattern matches had been found in two octants and that the muon charges were opposite (or ambiguous) or that matches had been found in more than two octants (no sign requirements). If these requirements

were satisfied, the online computer was interrupted to begin data acquisition, otherwise the trigger and readout systems were reset. The time required for the second level trigger to cycle all trigger patterns and reset the system was about 15 microseconds.

The performance of the trigger for a typical data run is summarized in Table 5. One should keep in mind that the actual number of reconstructed events per 1 second spill was about 0.025. Essentially all of the triggers were accidental coincidences of uncorrelated muons. Note that the effect of the veto was a 20% reduction in the first level trigger rate and the second level trigger further reduced the trigger rate by a factor of twenty.

The Drift Chambers

The reconstruction of the trajectories of muons which satisfied the trigger required more precise position information than was provided by the scintillation counters. A system of 112 drift chambers with 3360 sense wires was used for this purpose.[35] Each octant of the seven instrumented gaps in the spectrometer magnets contained two trapezoidal drift chambers (see Figure 4). The upstream or "straight" chamber contained two planes of sense wires, the orientation of which was perpendicular the radial bisector of the octant. The downstream or "skew" chamber contained two planes or wires that were inclined by 100 milliradians with respect to those of the upstream chamber. The dimensions and number of wires of the chambers varied from gap to gap and are summarized in Table 6. The internal construction of all chambers was identical. A side view of several drift cells is shown in Figure 16.

Each 2.0 inch X 0.75 inch cell was constructed of aluminum I-beam cathodes that were insulated from a grounded aluminum center plate. A 0.001 inch diameter gold plated tungsten sense wire was mounted in the center of each cell. A second plane of wires was mounted on the reverse side of the center plate but with the cells staggered by half a cell width to resolve the left-right ambiguity inherent in symmetric drift cell arrangements. An aluminum outer shell provided both a gas seal and a second ground plane above each cell. The chambers were operated with a gas mixture of 50% Argon and 50% Ethane. The I-beam cathodes were held at a potential of -1200 volts and the sense wires at +2300 volts. This produced an electric field that was sufficient to saturate the electron drift velocity and provide adequate electron multiplication at the sense wires. The drift velocity was measured to be 0.020 inches per 9.3 nanoseconds (the choice of units will become apparent). The spatial resolution of the chambers was measured in a test beam to be approximately 0.012 inches per single plane measurement. One often encounters, in documents similar to this one, a statement to the effect that the efficiencies of all drift chamber wires were measured to be better than 98%. While such a statement is true for the majority of the wires in this system, it is definitely not true for many others. The reader is referred to the "Systematics" section of the succeeding chapter for further discussion.

A block diagram of the drift chamber electronics is presented in Figure 17. Signals from the sense wires were conveyed along 100 ohm twisted pair transmission lines to 8-channel amplifier/discriminator cards located along the outer edges of the chambers. Each amplifier/

discriminator channel, shown in Figure 18, consisted of two ECL 10216 integrated circuits. The first IC was wired as a three-stage amplifier having a gain of about 100 and a bandwidth of 100 MHz. The second IC was configured as a discriminator which produced a 75 nanosecond differential ECL output pulse. The threshold of the amplifier/discriminator was approximately 1 millivolt across the 100 ohm input impedance. The output stage of each discriminator was connected to the time encoding system via 50-foot-long twisted pair cables. The encoding system, shown in Figure 17, was composed of eight-channel encoder cards organized into crates of sixteen encoders and one clock card. Each encoder channel consisted of digital timing logic and a 6-bit X 16-word memory stack. A diagram of the timing logic is shown in Figure 19. The discriminated amplifier signal was received and distributed to the clock inputs of six fast latches. This caused the latches to record the states of five timing signals and an input wired to be always true. Every 74.4 nanoseconds, the state of all latches was recorded on the rotating memory stack. Four of the latched timing signals, labelled A through D, were used to divide each 74.4 nanosecond major memory cycle into eight 9.3 nanosecond bins (see Figure 20 for a timing diagram of all signals). The fifth timing signal, labelled 2T, was available to disentangle memory location ambiguities that could arise for hits arriving immediately before the latch information was recorded in memory. The last bit, labelled hit flag, was only present if a hit had arrived during the memory cycle and was used to indicate such. The time of arrival of a hit could thus be reconstructed from its location in the memory stack and the state of the timing phases. The encoding system was always

alive, logging all hits which had occurred within the previous 16 X 74.4 nanoseconds = 1.2 microseconds (hits occurring earlier were overwritten).

When a trigger occurred, a stop pulse was sent from the first level trigger logic to the encoding system. The signal was delayed to insure that all drift chamber hits associated with the trigger had been logged (the maximum drift time was approximately 500 nanoseconds). The stop pulse was distributed to each of the twenty-eight encoder crates in the system. It served two functions: it was treated as an ordinary hit and encoded as outlined above; and it caused the clock card in each crate to cease generating timing signals, thus preventing any of the hits associated with the trigger from being overwritten. If the second level trigger was not satisfied, a reset pulse was applied to all clock cards causing them to resume generation of timing signals and the encoders to resume logging of hits. If the second level trigger was satisfied, the data acquisition computer instructed each of seven 8X300 microprocessors to begin processing the drift chamber information. Each microprocessor was connected to four encoder crates through their clock cards. The clock cards served as ports that enabled the microprocessor to search all memory locations of all channels for hit flags. The microprocessor first reconstructed the arrival time of the stop pulse and then repeated the procedure for all flagged hits. The 8X300 subtracted the hit times from the stop time and stored the net times and channel addresses in a 16-bit X 64-word FIFO (first-in, first-out) memory. The memory was accessable by the data acquisition computer via a serial CAMAC link. After all data had been processed, the microprocessors were instructed to restart all clock card timing signals and

resume data logging. The microprocessors were capable of scanning the entire system and processing the 300 hits typically recorded in about 3 milliseconds.

The Data Acquisition System

The preceding sections have described the components of the spectrometer and how the various systems detected and measured muon pair final states. The remaining function of the apparatus was to record this information for further analysis. A block diagram of the data acquisition system is shown in Figure 21. The main element of the system was a Digital Equipment Corporation PDP-9 minicomputer. The PDP-9 communicated with all hardware through a 5-crate CAMAC system. Data transfer to and from three of the crates, located near the PDP-9 in the E326 Portakamp, was via a standard CAMAC highway. The trigger logic and drift chamber electronics were located adjacent to the spectrometer, some 350 feet away. Since timing and signal attenuation considerations limit parallel highway lengths to about 50 feet, a CAMAC serial highway was used to communicate with two crates located near the spectrometer. The PDP-9 logged data with an 800 BPI, nine track tape drive. In addition, the data was stored temporarily in a 256K-word bulk memory. The memory was accessed asynchronously by a PDP-11/45 computer which was used to monitor the experiment and generate displays that were more involved and time consuming than those generated by the PDP-9.

The PDP-9 exercised essentially complete control over the experiment. Before data runs, the computer was used to turn on and set the remote high voltage system for the scintillation counters. It

loaded the trigger processor patterns into the trigger processor memory and programmed the matrices, the PML and the FDL. During actual data logging, the computer generated a number of video and storage scope displays of the status of the experiment. About 200 milliseconds before a beam spill, the display generation was interrupted to perform various initialization tasks. During the spill, each trigger caused an interrupt. The PDP-9 instructed the seven 8X300 microprocessors of the drift chamber encoding system to begin processing information and then proceeded to read all fixed data for the event. The fixed data consisted of twenty-four words (24-bit CAMAC words) of scintillation counter latch information, eight words of trigger processor information, twenty-four words of TDC information, and eight words of ADC information. The terms TDC and ADC refer to Time to Digital Converter and Analog to Digital Converter. Such devices were used to monitor various pieces of hardware during the operation of the experiment. The computer then read the variable amount of data from the seven drift chamber FIFO memories. As each different type of data was received, it was organized into logical blocks of less than 128 16-bit words. Sequences of logical blocks were then assembled into physical blocks of less than 1024 words and written onto magnetic tape. After all data for the event had been logged, the trigger, drift chamber encoders, and livetime gates were all reset and the computer resumed display generation. At 200 milliseconds after a beam spill, the PDP-9 was interrupted by a signal indicating that the Fermilab control system had beam monitor and beamline information available. The computer proceeded to read 136 channels of scaler information and the control system information and log an additional five logical blocks of data onto magnetic tape.

The time required to log a typical event was about 30 milliseconds. This was dominated by the slow speed of the CAMAC serial highway in transferring the 300 words of drift chamber information that typically occurred. Since the trigger rate was approximately six to seven triggers per second, the livetime was about 80%.

CHAPTER III

THE ANALYSIS

At the conclusion of the 1981 run of E326, the data that were used for this work existed as twenty-eight magnetic tapes. The process of converting the information stored on those tapes into a physical result was divided into two parts. The first part was the generation of a muon pair signal from the raw information. The second part was the physical interpretation of the signal. This chapter deals exclusively with the former task. It is divided into the following sections: the reconstruction of events; the separation of the signal from backgrounds; the calculation of any remaining backgrounds; the normalization of the signal; and a study of systematic uncertainties.

Operationally, the event reconstruction was performed by a large computer program which processed the primary data tapes and produced secondary disk files which contained both raw data and information about the reconstructed events. The secondary disk files were organized by target type and consolidated onto high density magnetic tapes (referred to as DSTs). A series of small computer programs operated from a single batch job was then used to apply event selection criteria, calculate the backgrounds and normalization, and correct the signal for known systematic problems.

In the analysis of the data, a cylindrical coordinate system was

used to describe the spectrometer. The origin of this coordinate system was the nominal target position that was located 6 inches upstream of the collimator. The z axis was concurrent with the beam and spectrometer axes. The positive direction was defined to point downstream. The x axis was defined to point horizontally to the west and the y axis to point vertically upward. This defined a right handed cartesian system from which the polar system was defined. The azimuthal or phi angle of any point was the angle of rotation from the x axis proceeding in a positive sense (toward the y axis). The radial coordinate of any point was the distance from the z axis.

The Reconstruction Program

The reconstruction program processed data in a pulse oriented fashion. All of the raw data corresponding to one accelerator spill was read from magnetic tape, unpacked, and stored on a disk file. The program then sequentially processed all of the data associated with each trigger. The latch and drift chamber information was unpacked and sorted by octant and detector plane. The latch data was then compared with the list of 291 processor patterns. Unlike the hardware trigger processor, the program remembered all patterns matched in up to three octants (the fraction of triggers with more than three triggering octants was less than 0.1%). The logical "OR" of all matched patterns was used to determine the region of each octant to be searched for drift chamber hits. These "counter roads" included all drift chamber wires that were sensitive to the region defined by the trigger counter(s) plus an additional two wire zone on either side of the counter(s).

A local coordinate system was defined for each triggering octant. The local x axis bisected the octant and was perpendicular to the sense wires of the straight drift chambers. The local u axis was inclined by 100 milliradians with respect to the x axis and was perpendicular to the stereo view chamber sense wires. The local y axis was perpendicular to the x axis and coincident with the global phi axis at the octant center. The first step in the spatial hit reconstruction was to reconstruct x and u coordinates from the straight and skew chamber information. The half cell staggered chamber geometry (see Figure 16) implied that the drift times measured by two adjacent wires in response to the passage of a trigger associated particle were correlated. The sum of the raw drift times was in fact a constant for normally incident particles and varied somewhat with track angle (detailed expressions for the spatial hit reconstruction are available in Appendix I). The reconstruction program paired all permutations of adjacent wire hits and calculated a sum of times for each pair. If the sum of times was within fifteen time encoder bins of nominal, the program calculated a spatial x or u position for the pair (this sum of times requirement is rather loose and is discussed in more detail in Appendix I). Note that a raw hit was allowed to pair to an arbitrary number of adjacent hits. All hits which successfully participated in some pairing were then deleted from the list of hits within the counter road. The x or u positions of all remaining hits were calculated allowing for the unresolved left-right ambiguity. The x and u hits were then paired to form 3-space points in the global spectrometer coordinate system. Since the small angle stereo reconstruction involved a 10-fold magnification in the local y direction,

the azimuthal coordinate was very sensitive to track angle effects (see Appendix I). A correction was made for this by using trigger pattern information. Each pattern was tagged with a set of most probable track angles for each detector plane. The track angles associated with the most desirable pattern match were used to do a first-order correction of both the azimuth and radius of each hit. All x-u pairings that produced spatial hit coordinates within 4 inches of the active drift chamber volume were accepted.

After all x, u, and 3-space hit coordinates had been reconstructed for each counter road, the track finding phase of the program began. Since muons produced on or near the spectrometer axis move at fixed aximuth in the toroidal magnetic field, the track finder searched for azimuthal clusterings of hits. Each octant with a counter road was divided azimuthally into sixteen wedges of 50 milliradians width. The presence of hits with phi coordinates within a given wedge at each of the seven gaps was represented by setting a bit in one of sixteen seven-bit words (one word per wedge). The program searched for azimuthal clusters by forming all groups of four adjacent wedges. It required that at least one of the thirteen possible groups contain at least three gaps with hits. If this was the case, a search was made for local maxima in the number of gaps with hits. The program tried to increase the number of gaps in the local maxima by expanding the groups to adjacent wedges. Overlapping groups were then concatenated. This procedure ultimately resulted in as many as three azimuthal regions or "phi roads" per octant to be searched for tracks.

As was mentioned in the previous chapter, the efficiencies of

the drift chambers in the first spectrometer gap were rather poor. It was decided not to require 3-space hits in gap 1, which implied the existence of both x and u information, but to allow x or u hits provided that a 3-space hit had been found in gap 2. In this case the radial hit coordinates at gap 1 were reconstructed using the azimuth from the downstream portion of the track. Each of the phi roads was therefore required to contain at least four gaps with hit information or, if there were no 3-space hits in gap 1, to contain hits in gap 2 and two other gaps. The program then cataloged all 3-space hits in each phi road and if gap 2 was present, identified all unpaired x and u hits in gap 1. The next step was to call the track fitting routine for all permutations of hits in each road (the track fitting procedure is described in Appendix II). The permutation sum was arranged so that the sum over gap 1 hits was innermost. If unpaired gap 1 x or u hits were present, this permitted recovery of gap 1 hits via a two-stage fitting procedure. The program fit each permutation of downstream hits and extrapolated the fit to the gap 1 chamber planes. Radial positions were reconstructed for all unpaired x or u hits within 3.5 inches of the extrapolated track position and added to the list of existing gap 1 3-space hits (if any existed). The program then refit the track including each of the gap 1 hits. All fit information corresponding to the hit permutation with the best total chi-squared, χ^2, was retained. If no permutation had a χ^2 less than 2.0 (which was quite poor; see the following section), the program attempted to discard gaps from the fit to obtain an acceptable χ^2. A minimum of four gaps of information was required at all times. An acceptable fit found in any phi road was defined as a muon.

The program required at least two muons to continue processing the event. If two muons were found, the reconstruction program recorded all raw data and track reconstruction information associated with the event on an output file (referred to as a DST file). The track finding procedure was then repeated but with the fitting routine set to constrain all tracks to originate at the center of the experimental target. This second pass could find entirely different tracks and was useful in testing the hypothesis that tracks found by the first pass were target associated. Additionally, the resolution of the track fit parameters for target associated tracks was improved by the procedure. The result of the second track finding pass was recorded on the DST file regardless of the outcome.

The reconstruction program also transferred additional raw data such as scaler and control system information to the DST file. The effect of the program was to reduce the number of triggers by approximately a factor of three and to reduce the number of tape blocks by a factor of two.

Event Selection

The reconstruction program produced a sample of 63,000 event candidates. Only about 400 of these were real, prompt muon pairs. This section describes a series of selection criteria that were applied to the data sample to enhance this rather miserable signal-to-noise ratio. The utility of the selection criteria will be demonstrated in the following section which describes the techniques used to measure and subtract residual backgrounds. The reader should keep in mind that the

ensuing physics analysis involves the comparison of data produced by interactions in four different targets. The absolute efficiency of the selection criteria does not affect the comparison except in a statistical sense. One must be careful, however, to avoid creating any acceptance edges that could lead to systematic differences in detector efficiency for different length targets.

Table 7 summarizes the effect of each of the selection criteria on the data sample. The event total corresponding to each item in the list is the number of opposite sign dimuon and multimuon (more than two muons with no charge requirement) events that remained in the data sample after the listed cut was applied. Note that data from all targets are included in the sample. The first requirement was the track topology cut. The reconstruction program required that the coordinates of all tracks be measured in at least four of the seven instrumented gaps in the spectrometer. The topology cut required that at least four track measurements occur in the first five spectrometer gaps. This had the effect of suppressing strange background events and of improving the resolution of the reconstructed track parameters. The radial and transverse chi-squared (χ^2_R and χ^2_T) distributions for all tracks that satisfied the topology cut are presented in Figures 22 and 23. As described in Appendix II, the radial and transverse chi-squared functions were defined to be diagonal (the track residuals at each gap were assumed to be uncorrelated). The deviations were assumed to be dominated by multiple Coulomb scattering. Therefore, the square of each residual was weighted by the inverse cube of its distance from the target. This procedure maximized the resolutions of the fitted track angle and target plane

intercept but yielded chi-squared distributions with strange normalizations. Poorly fit tracks were removed from the data sample by requiring that χ^2_R be less than 0.15 and χ^2_T be less than 0.20.

The target plane radius is defined as the distance between the track and the z axis at z = -7 inches (the position of the target center). The distributions of positive and negative tracks satisfying the chi-squared cuts are shown in Figures 24 and 25. They are nearly identical, both showing a small enhancement near the target at zero radius and an enormous halo muon peak near a radius of 10 inches. The distributions of the fitted track angle at the target for the same positive and negative muons are presented in Figures 26 and 27. Both distributions peak near 10 milliradians but otherwise have very different shapes, reflecting the different spectrometer acceptances for focused and unfocused tracks. The scintillation hodoscopes and drift chambers subtended a minimum angle of about 30 milliradians with respect to the beam axis. One would therefore expect that target associated tracks must have angles at least as large. Figures 28 and 29 are reconstructed track angle distributions of events produced by a fairly sophisticated Monte Carlo simulation. The simulation will be described in some detail in the succeeding chapter. It is sufficient for purposes here to state that the performance of the spectrometer is well described by the simulation. Note that even with resolution smearing, the spectrometer has no acceptance for positive muons with reconstructed track angles less than 25 milliradians and negative muons with reconstructed angles less than 45 milliradians. Using this information as a guide, it was required that the reconstructed track angle of each positive muon, θ_+, be larger than

25 milliradians and the reconstructed angle of each negative muon, θ_-, be larger than 45 milliradians. The sensitive reader may find himself (or herself) staring at Figures 26 and 27 in disbelief. It appears that extremely restrictive cuts are being placed at the edges of very steep distributions and that these cuts are justified solely by a calculation. This is definitely not the case. The track angle cuts are extremely powerful and will be demonstrated to be rather conservative.

The target radius distribution for all tracks from events satisfying the angle requirements is presented in Figure 30. Comparing Figure 30 with either of Figures 24 or 25, one will note the enormous suppression of the large radius halo distribution. Figure 31 is a scatter plot of the target radius of the positive muon, R_+, versus that of the negative muon, R_-, for all dimuon events in Figure 30. A strong clustering is evident near $R_+ = R_- = 0$ indicating the presence of a correlated signal. Using Figures 30 and 31 as a guide, it was required that the absolute value of the target radius be less than 5 inches.

As is indicated in Table 7, some 455 events remained after the preceding series of cuts. One such event contained three muons and was discarded. A rather artificial requirement was made of the remaining events. The reader will recall that all trigger processor patterns were labelled as positive, negative, or ambiguous, reflecting the probable charge of the triggering particle. The patterns labelled originally as ambiguous were assigned a definite charge (the most probable charge). All events were then required to pass a software trigger requirement. It was required that the processor patterns in the triggering octants of each event define an opposite sign dimuon. Furthermore, it was required

that the sign of the reconstructed muon agree with the trigger pattern charge. This had the effect of removing two events from the data sample but of greatly simplifying the background calculation to be discussed in the following section.

A requirement was made of the radial chi-squared from the target constrained fit, χ_c^2. A plot of this quantity for both muons of each of the remaining events is shown in Figure 32. Figure 33 is a scatter plot of χ_c^2 for the positive muon versus that for the negative muon of each event. It was required that χ_c^2 for both muons be less than 0.3.

There were several runs during the course of the experiment for which a single octant of the spectrometer experienced some hardware difficulty. The nature of these difficulties will be discussed later in this chapter. The simplest method of dealing with such runs was to eliminate the afflicted octant from the analysis. All events from the affected runs with muons in the bad octant were removed from the data sample. As is shown in Table 7, three events were lost. Figure 34 is a plot of the reconstructed masses of the 396 events that remained after all cuts had been applied. There is a clear peak in the psi region and a high mass continuum extending to 11.5 GeV/c^2.

At this point it is useful to reexamine the distributions to which cuts have been applied. No distribution should appear to be truncated if acceptance edges are to be avoided. The unconstrained radial and transverse chi-squared distributions of the 396 events in the final data sample are shown in Figures 35 and 36. Both distributions drop rather comfortably toward zero before the cuts are encountered. Figures 37 and 38 are similar plots of the target radius distributions

of the positive and negative muons, respectively. There are some small edges in the negative muon distribution but nothing that a small background subtraction didn't cure. Figures 39 and 40 are plots of the track angle distributions of the positive and negative muons, respectively. Note the conspicuous absence of edges at small angles. One can conclude that the selection criteria achieve the goal of an enhanced signal to noise ratio without an undue loss of efficiency. These conclusions will be strengthened somewhat by the results of the succeeding section.

Background Calculation

The only method of determining the efficacy of the selection criteria was to measure the residual contamination of the signal. The backgrounds can be characterized as accidental or prompt. The former category includes all "events" formed from the random coincidence of uncorrelated target muons. The term "target muon" refers to any reconstructed track that satisfies the selection criteria. Possible sources of such tracks are: beam halo; prompt production of muons in the target; decays of long lived hadrons produced in the target; and misidentified beam halo caused by additional drift chamber hits. The prompt background category includes all sources of correlated opposite sign muon pairs that were not produced in the experimental target (any correlated pair that was produced in the target is defined as signal regardless of the production mechanism). The dominant production site for such backgrounds was the steel collimator that was located 13 inches downstream of the target. The measurement of the prompt background signal was also subject

to contamination by accidentals. Therefore, the accidental background measurement will be discussed first.

The event selection criteria all involve requirements made of individual tracks. There are no requirements that correlate the two muons in each event (except for electric charge). This feature enables one to infer the rate of accidental coincidences of two target muons from the coincidence rate of a single target muon with a clearly uncorrelated track. The essential premise of the analysis that follows is that all events found with a target muon in one octant and a halo track in another are accidentals. To insure that this was indeed the case, the definition of a halo track was made fairly restrictive. It was required that each halo track satisfy the following criteria: the track had to satisfy the topology cut; the radial and transverse chi-squared functions had to be less than 0.15 and 0.20, respectively; the track angle had to be less than 25 milliradians; and the target radius had to be larger than 5.0 inches. The opposite sign requirement resulted in target-halo events that usually contained either a negative target-positive halo combination or positive target-negative halo combination. The sign associated with a halo muon was that of the trigger pattern and not that of the reconstructed track. The presence of trigger patterns of ambiguous sign complicates the picture a bit. This complication was removed by assigning all trigger patterns a definite sign and requiring that all reconstructed target tracks agree in sign with the trigger pattern label. The accidentals analysis was performed by searching the DST tapes for target-halo and halo-halo events. The calculation of the rate of target-target accidentals is described below.

Let $N(T^+, H^-)_{ij}$, $N(T^-, H^+)_{ij}$, and $N(H^+, H^-)_{ij}$ be the number of positive target-negative halo, negative target-positive halo, and positive halo-negative halo events found in octants i and j, respectively. Since the events of these types are accidentals, they can be written in terms of single muon rates,

$$\begin{aligned} N(T^+, H^-)_{ij} &= T_i^+ H_j^- N_{RF} D(1-\delta_{ij}) \\ N(T^-, H^+)_{ij} &= T_i^- H_j^+ N_{RF} D(1-\delta_{ij}) \\ N(H^+, H^-)_{ij} &= H_i^+ H_j^- N_{RF} D(1-\delta_{ij}) \end{aligned} \tag{24}$$

where: $T_i^{\pm}$ is the effective rate of positive/negative target muons per RF bucket in octant i; $H_j^{\pm}$ is the effective rate of positive/negative halo muons per RF bucket in octant j; N_{RF} is the number of RF buckets in the sample; D is a duty factor that indicates the average fraction of RF buckets with mean rates T and H; and δ_{ij} is a Kronnecker delta, present to indicate that two distinct octants were required by the trigger. It is straightforward to solve equations 24 for the the $T_i^{\pm}$ rates and to extract the expected number of accidental positive target-negative target accidentals, $N(T^+, T^-)_{ij}$,

$$\begin{aligned} N(T^+, T^-)_{ij} &= T_i^+ T_j^- N_{RF} D(1-\delta_{ij}) \\ &= (1-\delta_{ij}) \frac{\sum_k N(T^+, H^-)_{ik} \sum_l N(T^-, H^+)_{jl} - \sum_k N(T^+, H^-)_{ik} N(T^-, H^+)_{jk}}{N(H^+, H^-)_{tot} + N(H^+, H^-)_{ij} - \sum_l [N(H^+, H^-)_{li} + N(H^+, H^-)_{jl}]} \end{aligned} \tag{25}$$

where $N(H^+, H^-)_{tot} = \sum_{i,j} N(H^+, H^-)_{ij}$ is the total number of halo-halo events in the sample. In practice, the above analysis was performed on a run-by-run basis to insure that the mean effective rates accurately reflected the accelerator duty cycle and that the spectrometer acceptance was constant (the runs with an octant removed from the analysis required

separate treatment). The expected number of accidentals for each octant combination was then summed over all runs for each target. The DST information for the single target muons from the target-halo events was stored on disk files. The information corresponding to the positive tracks was combined with that for the negative tracks to form background events. An event weight that was equal to the ratio of the expected number of accidentals to the number of generated events for that octant combination was appended to each such event. In this way it was straightforward to generate properly normalized, background distributions of any desired kinematic quantity. A background subtracted mass distribution of the entire data sample is presented in Figure 41. The normalized accidental background distribution is shown on the same logarithmic scale. A similar plot of the P_T distribution for all events with mass greater than 4.0 GeV/c^2 is shown in Figure 42. The expected contamination of the entire sample was 29.9±1.9 events or 7.6% of the total. The physics analysis involved only events with masses greater than 4.0 GeV/c^2. There were 320 events in this region (see Table 7). The accidentals background in the same mass region was 15.8±1.0 events or 4.9% of the total.

The prompt muon pair background was produced by hadrons from either of two sources interacting in the collimator. Approximately 9% of the incident hadron beam was measured (by the segmented ion chamber) to impinge on the collimator. Secondary hadrons produced in the experimental target also illuminated the collimator. This latter source can be entirely neglected. The minimum production angle necessary for target produced hadrons to intercept the collimator was 77

milliradians. Energetic hadrons are required to produce high mass muon pairs with any appreciable cross section. If one assumes that a minimum hadron momentum of 75 GeV/c is necessary (the cross section at 75 GeV/c is less than 20% that at 225 GeV/c), the secondary hadron must have a transverse momentum of at least 6 GeV/c. The cross section for the production large P_T secondary hadrons is quite small.[36] A crude estimate for the probability of producing such a secondary pion from the tungsten target is 2×10^{-10} per incident pion. This result implies that only the beam associated prompt background need be considered.

The beam associated background was directly measured by collecting data with the target removed. As was mentioned above, the target-removed signal could potentially be contaminated by the accidental background. An accidentals analysis, identical to that performed on the target-in data, was performed on the target-removed data. A summary of the data and calculated accidental background for the various targeting conditions is presented in Table 8. The event and background totals are listed for the entire data samples, for those events with mass greater than 4 GeV/c^2, and for those events with masses between 4 GeV/c^2 and 8.5 GeV/c^2. The total incident beam as scaled by the segmented ion chamber and corrected for detector livetime and removed octants is also listed. The target and collimator headings indicate the integrated beam that was incident on the experimental target and collimator for each targeting condition. Because the target-removed events were logged during separate runs, it was necessary to normalize the rate of such events to the incident beam flux. The net number of target removed events (accidentals subtracted) was normalized to the total flux that

was incident on the collimator. The expected number of prompt background events for each targeting condition was the product of this rate and the integrated collimator beam flux. The total number of raw events, accidental events, prompt background events, and net events are presented in Table 9 for all target samples and mass regions. The expected number of prompt background events was approximately the same as the expected number of accidentals.

A test of the event selection criteria and of the validity of the background subtraction techniques was performed by repeating the entire signal isolation analysis with less restrictive cuts. The unconstrained radial and transverse chi-squared functions were required to be less than 0.5 and 1.0, respectively. The track angle requirements were relaxed by 5 milliradians and the absolute values of the target radii were required to be less than 7 inches. No requirement was placed on the constrained radial chi-squared function. The definition of halo tracks was modified to insure that the angle and target radius requirements were complementary to the target track requirements. The event and accidental background totals for the five targeting conditions are presented in Table 10. The background corrected totals in each mass range for each target sample are listed in Table 11. The reader is strongly urged to compare the information in Tables 9 and 11. In all cases the increase in the number of raw events was compensated by an increased background subtraction. As an example, the uncorrected total number of events with mass greater than 4 GeV/c^2 increased from 320 to 435. The total background increased from 32.4 (10% of the raw total) to 143.5 (33% of the raw total). The net number of events for the two

sets of selection criteria differed by less than four. One can conclude that the event selection criteria are not excessively restrictive and that the background calculation techniques achieve their purpose.

Normalization and Systematics

The determination of the atomic mass dependence of the muon pair cross section will be discussed in detail in the succeeding chapter. The analysis involved a comparison of the cross sections for each of the four targets. Although absolute normalizations were not required, it was important that the relative normalizations of the separate data samples be consistent. The relative cross section normalizations relied on accurate measurements of the beam flux and corrections for differences in spectrometer efficiency.

The beam flux that was incident on each target was measured directly by the innermost channel of the segmented ionization chamber IC711/712/713. As was already mentioned, the absolute calibration of the ion chamber was of no relevance to this work. The stability of the ion chamber was, of course, extremely relevant. This was checked by comparing the total output from the three segments of IC711/712/713 with another ion chamber immediately upstream, IC710. Figure 43 is a plot of the ratio of the sum IC711+IC712+IC713 to the output of IC710 for all data runs in chronological order. Each target is represented by a different symbol. There appears to be a 0.5% systematic decline in the ratio with fluctuations of approximately the same magnitude about the mean. No target dependence is evident. The targets were quite close to

the ionization chambers. One might be concerned that backward travelling hadronic debris from the targets was counted as beam flux. Since the targets varied in length and density, this could lead to a target dependence of the flux measurements that might not appear in the ionization chamber ratio. Figure 44 is a plot of the ratio of the output of the innermost channel of the segmented ion chamber, IC712, to the output of the secondary emission monitor that measured the primary proton flux incident on the secondary beam production target, SE701. Again, the ratio is plotted for all runs in chronological order with different target runs represented by different symbols. This quantity was sensitive to the tune of the secondary beam and to the targeting of the primary beam. The step in pion yield that occurred between the third and fourth runs was the result of an extensive improvement in beam tune. The run to run fluctuations occurring thereafter were less than 2%. No systematic target dependence is evident. This supports the conclusion that if backward scattered hadrons are counted by the ion chambers, there is no target dependence of the effect.

There were a number of possible sources of target dependence of the spectrometer efficiency. They can be categorized as livetime effects or as hardware problems. The livetime effects had the virtue that they were monitored and appropriate corrections could be calculated. The three sources of spectrometer deadtime were the halo veto, the trigger processor, and the data acquisition system. The veto system was triggered approximately 160,000 times per one second spill. The trigger was dead for those 160,000 RF buckets which accounted for approximately 3 milliseconds of the 1 second spill. The trigger processor operated

typically 130 times during each spill incurring a total deadtime of 2 milliseconds. The deadtime was dominated by the data acquisition system. Approximately 30 milliseconds was required to log each of the five to seven event triggers that typically occurred during each spill. The data acquisition system gated off several scalers at the beginning of each event logging cycle and gated them on again at the end. This permitted a direct measurement of the data acquisition deadtime by comparing the measurements of some quantity by gated and ungated scalers. In practice, the triple coincidence rate of the west monitor telescope was used for this purpose. This had the feature that the livetime thus measured was automatically corrected for the accelerator duty factor. Corrections to the livetime for the veto and trigger processor were calculated from the scaled veto and trigger processor input rates. A plot of the monitored livetime for all runs is presented in Figure 45. The runs are grouped by target type and are chronologically ordered within each group. With one exception, the livetime was always better than 76%. There was some systematic dependence on target type. The incident beam flux for each run was corrected for the spectrometer livetime by taking the product of the ion chamber output and livetime shown in Figure 45.

The hardware problems can be characterized as temporary or permanent. The temporary problems were generally treated by fiducial cuts to eliminate data which might otherwise be difficult to interpret. The permanent problems must be addressed more directly. The problems in the former category will be considered first. There were several runs for which a drift chamber in the third octant of second gap was removed

because of high voltage problems. Additionally, the trigger processor latch inputs for octant one were miscabled for the duration of a target removed run. In both cases one octant had altered efficiency. The simplest solution was to remove the questionable octant from the analysis. The removal of one octant reduced the muon pair efficiency by 25%. The reduction was uniform over the entire acceptance since, by the symmetry of the detector, there were three equivalent octant pair permutations that remained for each permutation that was lost. The beam flux for the affected runs was reduced by 25% to account for the acceptance loss. Another problem that was temporary in the sense that only some of the data was affected was a noise problem in the trigger processor memory. No other problem vexed the E326 collaboration as did this one. No other problem caused as much consternation, loss of beam time, loss of sleep, and general anguish. The problem was simply that some fraction of the bits in the trigger processor memory were spontaneously altered. Before each data run, the memory was subjected to a battery of diagnostic tests to insure that all pattern and characteristic bits were correctly stored. During actual data taking, the PDP-11 event monitoring computer was run almost continuously in a trigger processor simulation mode. If memory problems were encountered, the trigger processor returned illegal pattern matches or incorrect characteristic bits. The PDP-11 indicated that things were amiss and the run was halted. Any of a number of remedies, ranging from scientific to mystical, were then applied to the hardware. A similar trigger processor simulation program was part of the reconstruction program. If trigger processor errors were suddenly encountered, the remainder of a run was removed from the analysis.

There were two permanent hardware problems. The first was that the eight M12 coincidence matrices were only about 80% efficient. This fact was established from special runs with an alternative trigger. The alternative trigger consisted of three large scintillation counters that were inserted into the first three gaps of some octant. The inefficiency appeared to be independent of beam intensity and due to a timing problem. The 7 nanosecond width of the discriminator output pulses required rather precise timing at the matrix coincidence gates. Although this was done quite carefully, it appears that a later decision to reduce the high voltage to the photomultipliers of first plane of counters caused sufficient time slewing to produce the observed inefficiency. Because the effect was independent of beam intensity and therefore, of the singles rate in the front hodoscope plane, one would not expect any target dependence of this effect. The matrix trigger rate for single muons, normalized to the incident proton intensity, is presented in Figure 46. Each run is represented by a single entry. As before, the entries are grouped by target and displayed in chronological order within each group. The singles rates for the spectrometer detection elements were always larger during runs with the heavy targets than during runs with the beryllium target. Although the lengths of all targets in hadronic interaction lengths were comparable, the lengths in radiation lengths varied greatly (see Table 2). The 0.5 radiation length beryllium produced considerably fewer electrons and photons than it's heavier counterparts. If the matrix efficiency were rate dependent, one would expect that the heavy targets show a reduction in trigger rate. The rates shown in Figure 46 do not support this scenario. The trigger rates

for the heavy targets are, if anything, larger by a few percent. While there is no evidence for any target dependence of the matrix efficiencies, there may be a temporal dependence. This effect will be incorporated into the estimate of the systematic errors of the result.

The second permanent hardware problem was alluded to in the previous chapter. The drift chambers in the upstream two spectrometer gaps operated with regions of significant inefficiency. The upstream chambers were subjected to an enormous flux of ionizing radiation. There was an accumulation of positive ions in many of the drift cells that reduced the electric field near the sense wires. This was a rate dependent effect and by the arguments of the above paragraph, possibly a target dependent effect. The efficiency of the chambers in each gap was measured by repeating the track finding procedure for selected runs with the gap removed from consideration. The reconstructed tracks were extrapolated into the selected gap and a search was performed for nearby hits. The chamber efficiency, averaged over several runs, is presented as a function of spatial position in Figures 47 and 48 for the chambers of gaps 1 and 2, respectively. The abcissa of both plots is the distance from the innermost wire. Note that in both cases, the efficiencies are poorest near the spectrometer axis and improve with increasing radius. The results of the efficiency measurements are summarized in Table 12. The average efficiencies of the x and u chambers for gaps 1 and 2 are listed by run and target. The gap 1 efficiencies do seem to show a small target dependent effect. The efficiencies for runs with the three heavier targets are consistent with each other. The efficiencies for the beryllium runs are larger by several percent. The effect of this on

the data was reduced somewhat since the reconstruction algorithm only required either the x or u chambers in gap 1 to fire. The efficiency of this logical "OR" is listed as the total gap 1 efficiency. Note that the magnitude of this target dependence is reduced to about 2%. The gap 2 chamber efficiencies were somewhat better than those of the gap 1 chambers and did not show any systematic target dependence. As with the matrix inefficiency, the effect of the target dependence of the chamber inefficiencies will be considered in the calculation of the systematic errors for the physical results.

As a final check on the self consistency of the data samples for each target, the ratio of the number of background-subtracted events (the signal) to the corrected pion flux for each run is presented in Figure 49. Each run is represented by a separate entry and is grouped by target type. There is considerable fluctuation within each group due to the poor statistics associated with any single run. A chi-squared test of the hypothesis that each group could be characterized by a constant rate was performed. The results are listed in Table 13. The chi-squared function did have acceptable values for each target group.

CHAPTER IV

INTERPRETATION

This chapter discusses the processes by which the muon pair signal was converted into measurements of the atomic mass dependence of the muon pair cross section and the P_T distribution. It might appear that all of the information necessary for these tasks was generated in Chapter III. After a moment's reflection, however, a number of practical difficulties and unanswered questions become apparent. The atomic mass dependence of the Drell-Yan model was defined by equation 15 in terms of a two-fold differential cross section. The coefficient of $A^{\alpha'}$ is a function of M and x_F (or x_A and x_B) that also depends on the proton fraction Z/A. The exponent α' can be measured by comparing the data for different targets in bins of M, x_F space and by applying appropriate corrections for the Z/A dependence of the model. This procedure is unworkable when one considers that the entire data sample consisted of 320 events with masses above 4 GeV/c^2. The obvious solution is to integrate equation 15 over the acceptance of the spectrometer and measure the A dependence of the integrated cross section. An understanding of the Z/A dependence of the coefficient of $A^{\alpha'}$ now requires a detailed knowledge of the acceptance of the spectrometer. It is also possible that the acceptance is not uniform over the length of the target. The different physical lengths of the targets may imply different ac-

ceptances. There are nuclear effects which might impact the measurement of α'. The nucleons within a nucleus are subject to Fermi motion. The center of mass energy of the beam hadron-target nucleon system will be smeared by such effects. Since the Fermi momentum for light nuclei differs from that for heavier (A > 12) nuclei, the beryllium cross section could be affected relative to that for the heavier targets. Another effect that requires investigation is the production of muon pairs by secondary hadrons that were produced in the target itself. Some of these considerations apply to the measurements of $\langle P_T^2 \rangle$ for the various targets. In fact, a knowledge of the shape of the transverse acceptance is required to normalize the measurements.

The question of backgrounds from sources that were distinct from the experimental target was considered in Chapter III. The contamination of the data sample from physics processes in the target has not been addressed. The psi and upsilon families of resonances have muon pair decay modes and must be eliminated from any measurement of continuum processes. The above considerations were all addressed by performing a Monte Carlo simulation of the experiment. A discussion of this calculation follows.

The Monte Carlo Simulation

The Monte Carlo program was a software simulation of the experiment. The simulation procedure involved several steps. About 1.2 million event trials were randomly generated in a 13-dimensional space for each target. The thirteen dimensions can be enumerated as follows.

Six independent quantities are required to specify a two particle final state. Those chosen for this analysis were: the muon pair mass, M; the muon pair longitudinal momentum in the hadron pair center of mass frame, $P_{\parallel}^{*}$; the transverse momentum of the muon pair, P_T; the azimuthal direction of the transverse momentum, ϕ_T; the cosine of the angle that is defined by the negative muon and the beam particle quark in the muon pair center of mass frame, cos (θ^*); and the aximuthal direction of the negative muon relative to that of the beam particle quark in the muon pair center of mass frame, ϕ^*. Three more quantities were required to specify the momentum vector of the target nucleon in the lab frame. Using spherical coordinates, the quantities are P_N, θ_N, and ϕ_N. Three cartesian coordinates were used to describe the position of the interaction vertex: x_T; y_T; z_T. Finally, the energy of the interacting pion was specified by E_π. The thirteen quantities uniquely specified the momenta and positions of the muons at the interaction vertex for each event trial.

The muon trajectories were simulated by propagating tracks through a hypothetical spectrometer. The measured magnetic field map was used to step each track in 4 inch circular segments through the spectrometer. The track angle was randomized before each step using a Gaussian multiple Coulomb scattering distribution that included Moliere tails. Similarly, the momentum of each muon was corrected for energy loss before each step. An energy loss distribution[37] that included ionization and radiative processes was used for this purpose. If the track passed within the fiducial volume of any detector plane, the track coordinates and struck scintillation counters were stored. Of the 1.2 million trials, only about 200,000 contained two muons which penetrated

the software spectrometer to the fourth instrumented gap. These events were stored on magnetic tape for processing by the reconstruction program. The reconstruction program first applied the trigger processor requirement to each event. If the trigger requirement was satisfied, the drift chamber inefficiencies were simulated by randomly eliminating track coordinates in accord with the measured efficiencies. The track finding and fitting algorithm was then applied to the remaining coordinates. All events with two reconstructed muons were stored on another magnetic tape. About 90,000 simulated events remained after this step.

The final step in the event simulation procedure was to weight each event in accord with the 6-fold differential cross section, the nucleon momentum distribution, and the joint distribution of beam intensity and energy. The weight assigned to each event was

$$w = \frac{1}{\rho_{MC}(\xi)} \; n_\pi(\vec{x}_T, E_\pi) \; \rho_M N_o \; |\Phi_N(\vec{P}_N)|^2 A^{\alpha'-1} \; \frac{d^6\sigma}{dq^6}(q, E_\pi, \vec{P}_N) \qquad (26)$$

where: w is the event weight; q represents the six kinematic variables describing the final state that were defined above; ξ represents all thirteen randomly distributed quantities; $\rho_{MC}(\xi)$ is the density of generated trials in the 13-dimensional space; $n_\pi(\vec{x}_T, E_\pi)$ is the beam flux per unit beam energy at the interaction point $\vec{x}_T$ and beam energy E_π; ρ_M is the mass density in grams per cubic centimeter of the target material; N_o is Avogadro's number; $|\Phi_N(P_N)|^2$ is the nucleon momentum density; α' is the A dependence exponent; and $d^6\sigma/dq^6$ is the 6-fold differential cross section.

The beam flux density, $n_\pi(\vec{x}_T, E_\pi)$ was taken to be uniform over the circular cross section of the targets. A z_T dependent beam energy

distribution was evolved from the incident beam energy distribution, accounting for the effects of absorption and secondary pion production in the target. The calculation is described in more detail in Appendix III. The resulting distributions for the upstream and downstream ends of the beryllium and tungsten targets are shown in Figures 65 and 66. The nucleon momentum distribution $|\Phi_N(\vec{P}_N)|^2$ is defined as the probability density of encountering a nucleon in the volume element d^3P_N about the momentum $\vec{P}_N$. The choice of distribution function was somewhat unclear and two extreme cases were tried. A conservative guess was a simple T=0 Fermi gas model,

$$|\Phi_N(\vec{P}_N)|^2 = \begin{cases} (\frac{4\pi}{3} P_F^3)^{-1} & |\vec{P}_N| \leq P_F \\ 0 & |\vec{P}_N| > P_F \end{cases} \tag{27}$$

where the Fermi momentum, P_F, was taken from electron scattering experiments[38] to be 0.195 GeV/c for beryllium and 0.260 GeV/c for the heavier target materials. A less conservative model was that used to correct the deep inelastic scattering data of the CCFR group.[39] Power law tails were appended to a T=0 Fermi gas model to yield the following distribution

$$|\Phi_N(\vec{P}_N)|^2 = \begin{cases} \frac{3}{4\pi P_F^3}\left[1 - 6\left(\frac{2P_F}{\pi}\right)^2\right] & |\vec{P}_N| \leq P_F \\ \frac{3}{4\pi P_F^3}\ \frac{2}{(1-P_F/4)}\left(\frac{2P_F}{\pi}\right)^2\left(\frac{P_F}{|\vec{P}_N|}\right)^4 & P_F < |\vec{P}_N| < 4\ \text{GeV/c} \end{cases} \tag{28}$$

where the choices for P_F were the same as for the simple model.

The six-fold differential cross section in equation 26 was taken to be a hybrid of the simple Drell-Yan model and a measured P_T distribution. The Drell-Yan cross section, as presented in equation 15, has

been integrated over the lepton pair center-of-mass angular variables $\cos(\theta^*)$ and ϕ^*. The simple electromagnetic annihilation model would predict a $1+\cos^2(\theta^*)$ behavior for the former and a flat distribution for the latter. Both features have been observed and any deviations occur only in regions of very small cross section. The shape of the P_T distribution was taken to be that measured by the CERN NA3 collaboration for π^--platinum interactions,

$$F(P_T) = 1.39 \times 10^4 \, P_T \, (1 - M_T/\sqrt{s})^{11.05}/M_T^{4.07} \qquad (29)$$

where $M_T = (17.22 + 4 P_T^2)^{1/2}$. The normalization of equation 29 is such that the integral of $F(P_T)$ over P_T between 0 and 7.5 GeV/c is unity. The dependence of the cross section on ϕ_T is, of course, trivial. The six-fold differential cross section as used in equation 26 is therefore

$$\frac{d^6\sigma}{dq^6} = \frac{2}{\sqrt{s}} \frac{8\pi\alpha^2}{9M^3[x_F^2 + 4\tau]^{1/2}} [V_\pi(x_A)G_N(x_B) + S_\pi(x_A)H_N(x_B)] \left(\frac{1}{2\pi}\right)^2 \times \frac{3}{8}(1 + \cos^2\theta^*) \; F(P_T) \qquad (30)$$

where the relationship $dM^2dx_F = 2M \frac{2}{\sqrt{s}} dMdP_{||}^*$ has been applied to equation 15.

The weighted, reconstructed Monte Carlo events were subjected to exactly the same event selection criteria as were applied to the data. Comparisons of reconstructed mass and P_T distributions to the accidentals-subtracted-data are presented in Figures 50 through 53 for masses larger than 4 GeV/c^2. For the sake of brevity, only distributions for the beryllium and tin targets are presented. The Monte Carlo distributions are shown. The normalization of the Monte Carlo has been adjusted to yield a best fit to the data. The agreement is quite good and does not depend on the choice of nucleon momentum distributions. It was

generally true that varying the nucleon momentum distribution did not appreciably affect the shape of any kinematic distribution. The normalization, however, was sensitive to the choice of nucleon momentum distribution. The number of weighted events differed by approximately 12% for the two choices. The difference was not target dependent and does not affect any of the ensuing analysis.

The structure of the Monte Carlo program facilitated the calculation of the spectrometer acceptance. Input spectrum tapes were generated for each target by appending event weights to randomly generated event trials. The acceptance as a function of any or all of the thirteen generated quantities could be calculated by taking the ratio of the output spectrum to the input spectrum. For example, the acceptance as a function of the z coordinate of the interaction vertex, z_T, was defined as

$$\varepsilon(z_T) = N_{out}(z_T)/N_{in}(z_T) \qquad (32)$$

where $N_{out}(z_T)$ and $N_{in}(z_T)$ are the number of weighted output and input events in bins of 0.8 inches. A plot of the z_T acceptance for the beryllium target is shown in Figure 54. Note that the acceptance is quite flat in z_T. The effect of resolution smearing for reconstructed quantities was easily included by binning the output spectrum in terms of the reconstructed quantity.

The psi and upsilon families of resonances were simulated by repeating the above procedure with several changes. The generated mass distribution reflected the natural line widths of the $\psi(3100)$, $\psi(3865)$, $\Upsilon(9460)$, $\Upsilon(10020)$, and $\Upsilon(10350)$. The differential cross section for the $\psi(3100)$ was taken to be the product of separate P_T and x_F distributions

that had been measured by the CERN NA3 collaboration.[41] It is well established[12,42] that the lepton pair center of mass angular distributions are flat for hadronically produced $\psi(3100)$s. Hence, the differential cross section was

$$\frac{d^5\sigma}{dq^5} = \text{Constant } F1\ (P_T)\ F2\ (x_F)\ \left(\frac{1}{2\pi}\right)^2 \frac{1}{2} \qquad (31)$$

where: $F1\ (P_T) = P_T\ (1-2P_T/\sqrt{s})^{5.56}\ [1+(P_T/3.66)^2]^{-6.01}$;

$$F2(x_F) = \begin{cases} (1-x_F)^3 & x_F > 0.54 \\ 0.53 \exp\left[-8.2(x_F-0.08)^2\right] & 0.54 \geq x_F > -0.06 \\ 1.92\ (x_F+0.3) & -0.06 \geq x_F \geq -0.3 \\ 0 & x_F < -0.3 \end{cases}$$

and the normalization has been chosen to produce the measured product of the total cross section and the muon pair branching ratio. The cross section for the $\psi(3685)$ was assumed to have the same functional form as that for the $\psi(3100)$. The functional form of the cross section for the upsilon family was assumed to be the same except that the x_F distribution was shifted by 0.10 (reflecting an observation of the CERN NA3 collaboration). The cross section normalizations were adjusted to agree with the measured ratio of the product of branching ratio and total cross section for each resonance to that for the $\psi(3100)$.[41,42]

A comparison of the reconstructed Monte Carlo psi resonances to the accidentals subtracted data is shown in Figure 55. The normalization of the Monte Carlo has been adjusted to agree with the $\psi(3100)$ peak in the data. The shapes of the distributions do not agree well. The simulation seems to fall too steeply at small masses and perhaps not steeply enough at larger masses. There are several possible reasons for the

discrepancy. The low mass continuum has not been included in the comparison and is quite substantial for muon pair masses below the psi family. The acceptance of the spectrometer in the psi region is quite steep and quite small and may not be well understood. And finally, the input cross sections for the resonances are not well measured. The purpose for the inclusion of the resonances in the Monte Carlo simulation was to estimate the level of contamination of the continuum sample. The disagreement of the Monte Carlo psi peak with the data at larger masses becomes somewhat worse if the Monte Carlo continuum is added to the comparison. The Monte Carlo tends to predict more events in the 3.5 - 4.0 GeV/c^2 region than is observed. The effect is to make the psi contamination estimate a bit more conservative. The fraction of psi family events with reconstructed masses larger than 4 GeV/c^2 is (7.6±2.5)%. The expected level of psi contamination of the data sample is 6.2±2.2 events or about 1.9% of the total sample with masses larger than 4 GeV/c^2.

The result of the calculation for the upsilon family was that the ratio of resonance to continuum for masses between 8.5 and 11.0 GeV/c^2 was (24.2±0.8)%. The expected number of upsilons in the total data sample was approximately eleven. This was adequate to spoil the agreement of the mass distributions of the continuum Monte Carlo and the data (Figures 50 and 52). The same Monte Carlo calculation appears to overestimate the level of upsilon production for a much larger data sample from a more recent run of E326 by roughly a factor of two. This is not surprising given the large uncertainties in both the form and normalization of the production cross section. The estimates given above are therefore likely to be too large. Figure 56 is a Monte

Carlo mass plot for the upsilon family only. A mass cut at 8.5 GeV/c^2 was expected to reject 95.6% of the entire upsilon signal. The expected level of contamination by the upsilon family was therefore less than 0.5 events. Given the poor agreement of the Monte Carlo with the data, this estimate is undoubtedly somewhat conservative.

The A Dependence of the Muon Pair Cross Section

The most general form for the atomic mass dependence of the muon pair cross section would be to let the exponent α' be a function of five kinematic variables, $\alpha' = \alpha'(M, x_F, P_T, \cos(\theta^*), \phi^*)$ (any dependence of α' on ϕ_T would violate the rotational symmetry of free space). Unfortunately, the limited statistics of the data sample would make any such measurement extremely imprecise. The only practical approach was to measure the A dependence of the integrated cross section. Using the notation of the previous section, the expected number of events in some region of the 6-dimensional kinematic space is

$$N_{\mu\mu} = \int d^{13}\xi \; n_\pi(\vec{x}_T, E_\pi)\rho_M N_o |\Phi_N(\vec{P}_N)|^2 \; \varepsilon(\vec{x}_T, E_\pi, \vec{P}_N, q) \times \left[f_1 A_1^{\alpha'-1} \frac{d^6\sigma}{dq^6}(Z_1/A_1) + f_2 A_2^{\alpha'-1} \frac{d^6\sigma}{dq^6}(Z_2/A_2)\right] \tag{33}$$

where: $\varepsilon(\vec{x}_T, E_\pi, \vec{P}_N, q)$ is the 13-dimensional acceptance of the spectrometer; the integral over d^6q corresponds to the region of the measurement; and where the target has been permitted to be composite, consisting of the mass fractions f_1 and f_2 of the nuclei A_1 and A_2. The nucleon momentum distributions of the nuclei A_1 and A_2 are assumed to be identical (which is certainly true for the nickel-tungsten target). Equation

33 is the basis of the A dependence measurement. The only approximation that one need make is to factor $A_1^{\alpha'-1}$ and $A_2^{\alpha'-1}$ out of the integral and define α' as an average over the kinematic region. The Monte Carlo calculation then provides a knowledge of the integral for each target. A measurement of α' can be obtained by fitting the equation to the data.

It is also possible to make a model independent analysis by applying some well-founded approximations to equation 33. The proton fractions of the targets used in the experiment are quite similar, ranging from 0.402 for tungsten to 0.456 for copper. The Z/A dependence of the cross section can therefore be neglected. It was shown in the previous section that there is no variation of the acceptance over the length of the longest target. The measured Fermi momentum for the beryllium nucleus differs only by 20% from that for the heavier targets. To good approximation, one can ignore the target dependence of the nucleon momentum distribution. As is indicated in Appendix III, the deviations of the beam flux distribution from an exponential z_T distribution are quite small (typically 5% over the lengths of the targets). The energy broadening of the beam as it passes through the target is an effect of similar magnitude. Hence, to good approximation, one can write the beam flux distribution as

$$n_\pi(\vec{x}_T, E_\pi) = \frac{N_\pi}{\pi R^2} e^{-z_T/\lambda_{ABS}} \hat{n}(o, E_\pi) \qquad (34)$$

where: R is the target radius; N_π is the total number of incident pions; λ_{ABS} is the nuclear absorption length of the target material; and $\hat{n}(0,E_\pi)$ is the incident beam energy distribution. Substituting equation 34 into equation 33 and invoking the above approximations, one can derive the result

$$\sigma_{eff} \equiv \frac{N_{\mu\mu}}{N_{\pi}\rho_M N_o \lambda_{ABS}(1-e^{-4\lambda_{ABS}})} = \sigma_o[f_1 A_1^{\alpha-1} + f_2 A_2^{\alpha-1}] \qquad (35)$$

where: L is the length of the target; σ_o is a constant that is independent of all target related parameters; and α is the model independent exponent. The form of equation 35 is independent of the details of the muon pair production cross section. It depends only on the ansatz that the cross section scales with atomic mass as A^{α}. The left hand side of equation 35 defines an acceptance weighted, effective cross section per nucleon, σ_{eff}. If $\alpha = 1$, the effective cross section is independent of the target composition. If not, the effective cross section is a well defined function of the target constituents. Using the information listed in Tables 2 and 8, the effective cross section was calculated for the data sample corresponding to each target. Only events with masses between 4 GeV/c^2 and 8.5 GeV/c^2 were considered. The cross sections are listed in Table 14 and plotted in Figure 57. The units of presentation are arbitrary. The abcissae of the data points in Figure 57 are based on the nominal atomic mass of each target (even though the tungsten target has a 5.7% nickel impurity). Note that any target dependence of σ_{eff} is rather weak, indicating that α is near unity. A function of the form given by the right hand side of equation 35 was fit to the data. The tungsten target was treated as composite. The fit results are summarized in Table 15, labelled as "Model Independent Fit". The chi-squared value of 2.2 for 2 degrees of freedom is quite acceptable and the best estimate of α is in excellent agreement with unity. The best fit is displayed in Figure 57 for pure targets of the atomic mass given by the abcissa.

The near constant quantity, σ_{eff}, is a rather convenient way to express the data. The definition of σ_{eff} can also be applied to equation 33,

$$\sigma_{eff} = f_1\sigma'(Z_1/A_1)\, A_1^{\alpha'-1} + f_2\sigma'(Z_2/A_2)\, A_2^{\alpha'-1} \tag{36}$$

where the function $\sigma'(Z/A)$ is defined as

$$\sigma'(Z/A) = \frac{N_{\mu\mu}^{MC}}{N_\pi \rho_M N_o \lambda_{ABS}(1-e^{-L/\lambda_{ABS}})} \tag{37}$$

$$= \frac{1}{N_\pi \lambda_{ABS}(1-3^{-L/\lambda_{ABS}})} \int d^{13}\xi\; n_\pi(\vec{x}_T, E_\pi)|\Phi_N(\vec{P}_N)|^2\, \varepsilon(\xi)\, \frac{d^6\sigma}{dq^6}(Z/A)$$

and where $N_{\mu\mu}^{MC}$ is the number of Monte Carlo events for some target or target constituent having a proton fraction Z/A and the physical parameters given in Table 2. The values of $\sigma'(Z/A)$ for each of the four target materials and the nickel contaminant of the tungsten target are listed in Table 16 under the heading "Monte Carlo". Since the normalization is arbitrary and will be determined from the fit, the value of σ' for the beryllium target has been defined as 1. The value listed for nickel would be correct for a pure nickel target having the same mass density and absorbtion length as the composite tungsten target. The values of σ' were insensitive to the choice of nucleon momentum distribution. The values listed in Table 16 correspond to the more conservative parametization. This is not to say that the result is insensitive to Fermi motion. Naively, one would expect that σ' would be a function of Z/A only. The results of a calculation involving the Drell-Yan cross section with no other effects are listed in Table 16 under the heading "Simple Calculation". As one would expect, the magnitude of $\sigma'(Z/A)$

reflects the proton fraction of the target (protons have two u quarks to annihilate with the $\bar{u}$ quark of the π^-). The Monte Carlo result for the three heavier targets is about 12% larger than for the beryllium target. The discrepancy is due mostly to the difference in Fermi motion for beryllium as compared with that for the heavier targets. The values of σ' for the heavier targets do follow the trend of the simple calculation. The effective cross sections that are listed in Table 14 were fit to the function

$$\sigma_{eff} = C'[f_1\sigma'(Z_1/A_1)\ A_1^{\alpha'-1} + f_2\sigma'(Z_2/A_2)\ A_2^{\alpha'-1}] \qquad (38)$$

where C' is an arbitrary normalization constant. The results of fit are summarized in Table 15, labelled as "Model Dependent Fit". The value of chi-squared is a bit worse than before, 2.7 for 2 degrees of freedom, but still acceptable. The model dependent exponent α' is smaller than α by 0.03 but is still consistent with 1. One can conclude that the integrated muon pair cross section scales linearly with atomic mass. This conclusion is insensitive to the details of the Drell-Yan model, the nucleon momentum distribution, and secondary pion production in the experimental target.

The $\langle P_T^2 \rangle$ Measurement

The measurement of the second moments of the transverse momentum distributions for the various targets had the virtue that the results were self-normalizing. No knowledge of incident beam flux, detector livetime, secondary pion production, and the like was required. Unlike the A dependence measurement, the $\langle P_T^2 \rangle$ measurement did require a knowl-

edge of the spectrometer acceptance. The shape of the transverse momentum acceptance was required to properly normalize the result (the absolute magnitude of the acceptance divides out of the calculation, see equation 40). The P_T acceptance was calculated from the ratio of the Monte Carlo output spectrum to the input spectrum. Since the event reconstruction procedure had finite resolution, the acceptance was defined as the ratio of the number of events having a given reconstructed transverse momentum, $N^R_{\mu\mu}(P_T)$, to the number of events generated with the same P_T, $N^G_{\mu\mu}(P_T)$,

$$\varepsilon(P_T) = N^R_{\mu\mu}(P_T)/N^G_{\mu\mu}(P_T) \qquad (39)$$

This procedure corrects the data for resolution smearing but can yield anomalously large values for the acceptance near regions of steeply falling cross section. The transverse momentum acceptances for each of the four targets are presented in Figure 58. Within the statistical errors of the Monte Carlo, no target dependence is evident. This is a rather pleasing result since it permits the use of exactly the same acceptance correction for each of the four data samples. Any sample-to-sample differences can therefore be ascribed to physics sources. The acceptance calculation was completely insensitive to the choice of nucleon momentum distribution. One might be concerned that the poor efficiency of the upstream drift chambers could affect the acceptance. This question was addressed by reconstructing Monte Carlo events with an extremely optimistic parametization of the drift chamber efficiencies. Only the overall normalization and mass distribution were affected. The shapes of the transverse momentum distribution and acceptance were insensitive to the drift chamber efficiency distribution. The mean of the

acceptance calculations shown in Figure 58 was used in the following calculation and is presented in Figure 59.

The second moments of the transverse momentum distributions for the various targets were calculated in a model independent way. The squares of the transverse momenta of individual events were corrected for the spectrometer acceptance and summed. The background subtraction was also incorporated yielding the following expression,

$$\langle P_T^2 \rangle = \frac{\sum_{i=1}^{N_D} \frac{P_{Ti}^2}{\varepsilon(P_{Ti})} - \sum_{i=1}^{N_B} \frac{P_{Ti}^2 w_i^B}{\varepsilon(P_{Ti})}}{\sum_{i=1}^{N_D} \frac{1}{\varepsilon(P_{Ti})} - \sum_{i=1}^{N_B} \frac{w_i^B}{\varepsilon(P_{Ti})}} \qquad (40)$$

where: N_D is the number of events in a given data sample; N_B is the number of background events for the data sample; w_i^B is the weight assigned to a background event; and $\varepsilon(P_T)$ is the acceptance function evaluated at the measured P_T of the event. Equation 40 was used to evaluate $\langle P_T^2 \rangle$ for each target sample for events with masses between 4.0 GeV/c^2 and 8.5 GeV/c^2. The background events were those from the accidental background calculation only. There were only four prompt background events in the target removed data sample with masses in the considered range. Four events are not adequate to measure the shape of a distribution. The effect of the prompt background will be considered below. The values of $\langle P_T^2 \rangle$ that were calculated from equation 40 for each target sample are listed in Table 17 and plotted against $A^{1/3}$ in Figure 60. The tungsten target was assumed to be pure. The effect of the nickel contaminant is also considered below.

The data show little or no dependence on $A^{1/3}$. The prompt background and impurity corrections completely vanish if $\langle P_T^2 \rangle$ is independent of nuclear size. This hypothesis was tested by fitting the data to a constant value for $\langle P_T^2 \rangle$. The results of the fit are shown in Figure 60 and listed in Table 18 labelled as "Constant Fit". The χ^2 function is quite acceptable, 2.81 for 3 degrees of freedom, and the data are consistent with the hypothesis. The best estimate for the constant was $\langle P_T^2 \rangle = 1.69 \pm 0.10$ GeV^2/c^2 which is in good agreement with the value of 1.63 GeV^2/c^2 expected from equation 16 (for s = 450 GeV^2).

One would also like to test the hypothesis that $\langle P_T^2 \rangle$ has a linear dependence on nuclear size,

$$\langle P_T^2 \rangle = a + b\, A^{1/3} \tag{41}$$

Since the data are consistent with a constant value for $\langle P_T^2 \rangle$, the best estimate for the linear coefficient b will be consistent with 0. It is interesting, however, to obtain an upper limit for b. The effects of the prompt background and the tungsten target impurity must be considered to obtain such an upper limit. The measured value of $\langle P_T^2 \rangle$ for some target, $\langle P_T^2 \rangle_M$, is related to the true value, $\langle P_T^2 \rangle_T$, by the relation

$$\langle P_T^2 \rangle_M = (1-f_B-f_I)\, \langle P_T^2 \rangle_T + f_B\, \langle P_T^2 \rangle_B + f_I\, \langle P_T^2 \rangle_I \tag{42}$$

where: f_B and f_I are the fractions of background and impurity events present in the data sample for some target; and $\langle P_T^2 \rangle_B$ and $\langle P_T^2 \rangle_I$ are the second moments of the P distributions for the background and impurity sources. Substituting equation 41 into the right hand side of equation 42, one can express the measured value of $\langle P_T^2 \rangle_M$ as

$$\langle P_T^2 \rangle_M = a + b[(1-f_B-f_I)\, A_T^{1/3} + f_B\, A_B^{1/3} + f_I A_I^{1/3}] \tag{43}$$

where: A_T is the nominal atomic mass of the target; A_B is the atomic mass of the background source (the atomic mass of the iron in the collimator is $A_B = 55.9$); and A_I is the atomic mass of the target impurity (the atomic mass of the nickel impurity in the tungsten target is $A_I = 58.8$). Using the measured prompt background fractions from Table 9, the data were fit to equation 43. The results of the fit are presented in Table 18 labelled as "Linear Fit". The χ^2 function had a value of 1.64 for 2 degrees of freedom and the best estimate of the linear coefficient was $b = -0.079 \pm 0.073$ GeV^2/c^2. Assuming a Gaussian likelihood function, the linear coefficient b was found to be less than 0.015 GeV^2/c^2 with 90% confidence.

Systematic Errors

The errors that were quoted in the two preceding sections were purely statistical. The only advantage that accompanies the analysis of a limited data sample is that a detailed understanding of the systematic errors is usually unnecessary. If a conservative estimate of the systematic errors indicates that they are small compared with the statistical errors, one need not proceed any further. Such estimates for the A dependence and $\langle P_T^2 \rangle$ measurements are discussed below.

The A dependence measurement was dominated by the ratio of the effective cross section per nucleon for the beryllium target to that for the tungsten target. The beryllium and tungsten measurements were the most precise and provided the largest lever arm for the exponent fits. Using equation 35, one can write that

$$\alpha \simeq 1 + \frac{\ln[\sigma_{eff}(Be)/\sigma_{eff}(W)]}{\ln[A_{Be}/A_W]} = 1 - \frac{\ln R}{3.0} \qquad (44)$$

where: $A_{Be} = 9$; $A_W = 183.9$; and $R = \sigma_{eff}(Be)/\sigma_{eff}(W)$. The uncertainty in the exponent is therefore about one third of the fractional uncertainty in the ratio of cross sections,

$$\Delta\alpha \simeq -\frac{1}{3.0}\frac{\Delta R}{R} \qquad (45)$$

The systematic uncertainties that enter the measurement of the effective cross sections are (see equation 35) those associated with the spectrometer efficiency, flux measurements, target densities, absorbtion lengths, and target lengths. The absorbtion lengths for the target materials were calculated from the total inelastic cross sections and the measured target densities (see equation A25, Appendix III). The target densities were obtained by weighing each target and measuring its dimensions. Substituting equation A25 into equation 35, one can write the effective cross section for some target sample as

$$\sigma_{eff} = \frac{N^0_{ev}\,\varepsilon_s\,\sigma_{inel}}{N_\pi A[1 - \exp(\frac{-m}{a}\frac{N_0}{A}\sigma_{inel})]} \qquad (46)$$

where: N^0_{ev} is the number of events that would be detected with perfect spectrometer efficiency; ε_s is the average spectrometer efficiency; m is the target mass; a is the cross-sectional area of the target; and σ_{inel} is the total inelastic cross section. Note that all dependence on the target length has vanished. Assuming that the systematic uncertainties in efficiency, inelastic cross section, pion flux, target mass, and target area are all uncorrelated, it is trivial to derive the following expression for the uncertainty of the effective cross section,

$$\left(\frac{\Delta\sigma_{eff}}{\sigma_{eff}}\right)^2 = \left(\frac{\Delta N_\pi}{N_\pi}\right)^2 + \left(\frac{\Delta\varepsilon_s}{\varepsilon_s}\right)^2 + \left[1 - \frac{L/\lambda_{ABS}\, e^{-L/\lambda_{ABS}}}{(1 - e^{-L/\lambda_{ABS}})}\right]^2 \left(\frac{\Delta\sigma_{inel}}{\sigma_{inel}}\right)^2 + \left[\frac{L/\lambda_{ABS}\, \exp(-L/\lambda_{ABS})}{(1 - \exp(-L/\lambda_{ABS}))}\right]^2 \left\{\left(\frac{\Delta a}{a}\right)^2 + \left(\frac{\Delta m}{m}\right)^2\right\} \quad (47)$$

The various uncertainties that were used to calculate $\Delta\sigma_{eff}/\sigma_{eff}$ for each target sample are listed in Table 19. The beam flux and spectrometer efficiency measurements were discussed in Chapter III. The ion chamber measurements were observed to drift by 0.5% over the course of the experiment with fluctuations of about the same magnitude. To be conservative, a 1% systematic error was assigned to the flux measurements. The efficiency of the front chamber plane was measured to change by approximately 2% during the beryllium target runs. While no target dependence of the matrix efficiency was observed, there was a slow temporal drift of the matrix singles rate over the course of the experiment. This was probably due to changes in beam conditions, however, in the interest of conservatism, a 3% systematic error for matrix efficiency was assigned to each target. These two effects were added in quadrature and a 3.6% efficiency uncertainty was assigned to each target sample. The inelastic cross section measurements by A. S. Carroll et al. had quoted errors of about 3% for each target material. The measurement errors for the masses and cross-sectional areas of all targets are listed in Table 19 but are of negligable effect in comparison to the other sources of systematic error. The total systematic error for each target measurement was approximately 3.8%. A worst case scenario would be to let the beryllium cross section vary in one direction by 3.8% and let the tungsten cross section vary in the opposite direction by the

same amount. Using equation 44, the deviation in α would be 0.025 which is less than half the statistical error. The systematic errors are not large enough to affect the conclusions of the A dependence measurement.

Equation 44 was also used to estimate the effect of the residual psi contamination on α. The atomic mass dependence of the process $\pi^- + A \rightarrow \psi + x$ has been measured by several groups.[43] All measurements of the A dependence exponent are in the range 0.87 to 0.97. Assuming an exponent of 0.93 and using the event totals presented in Table 8, the effect of the psi contamination was to alter the measured value of α by $\Delta\alpha = 0.0014$.

The $\langle P_T^2 \rangle$ measurement was insensitive to everything except the shape of the transverse momentum acceptance. The acceptances for the various targets were the same to within the statistical errors of the Monte Carlo calculation. Similarly, the shape of the acceptance was insensitive to the drift chamber efficiency parametization (again to within statistical errors). One might be concerned that the Monte Carlo statistics are concealing what are real effects. This concern was addressed by repeating the $\langle P_T^2 \rangle$ calculation for two varied transverse momentum acceptances. The new acceptances were created by altering the acceptance shown in Figure 59. A "flat" acceptance was created by systematically increasing the mean acceptance for P_T less than 2.25 GeV/c and by systematically decreasing it for P_T larger than 2.25 GeV/c. The magnitude of the changes (in standard deviations) was increased linearly as one moved away from 2.25 GeV/c. The overall size of the effect was adjusted to increase chi-squared by one unit. In this sense, the "flat" acceptance represents a one standard deviation variation of the

acceptance. A "steep" acceptance was created by reversing the procedure (see the contours shown in Figure 59). The resulting values of $\langle P_T^2 \rangle$ for all target samples and acceptances are listed in Table 20. The effect of altering the acceptance was about 1.5% in the worst case. The flat acceptance had the effect of increasing the values of $\langle P_T^2 \rangle$ for each target and the steep acceptance had the opposite effect. The effect of the altered P_T acceptances on the 90% confidence limit for b was investigated. Equation 43 was fit to several permutations of the data. The results are summarized in Table 21. The data was refit with the values of $\langle P_T^2 \rangle$: decreased for beryllium; increased for tungsten; and decreased for beryllium and increased for tungsten. The last and worst case involved an increase in the 90% confidence limit on b from 0.015 GeV^2/c^2 to 0.021 GeV^2/c^2.

Conclusions

This document has presented data on the production of large mass muon pairs in 225 GeV/c π^--nucleus collisions. The atomic mass dependence of the integrated cross section for muon pair masses between 4.0 GeV/c^2 and 8.5 GeV/c^2 has been investigated. The model independent exponent α was determined to be 1.00±0.06. The model dependent exponent α' was determined to be 0.97±0.06. Thus the data are consistent with a linear scaling of the cross section with atomic mass. This conclusion is independent of the details of the Drell-Yan Model, the nucleon momentum distribution, and secondary pion production in the experimental targets.

The nuclear dependence of the second moment of the muon pair

transverse momentum distribution was also investigated. The data are consistent with the independence of $\langle P_T^2 \rangle$ of nuclear size. The average value of the second moment for muon pair masses between 4.0 GeV/c^2 and 8.5 GeV/c^2 is $\langle P_T^2 \rangle = 1.69 \pm 0.10$ GeV^2/c^2. If one parametizes the nuclear dependence of $\langle P_T^2 \rangle$ as $a + b\, A^{1/3}$, the upper limit for the linear coefficient b is 0.015 GeV^2/c^2 with 90% confidence. The initial state interactions predition of Bodwin, Brodsky, and Lepage (see equation 22) is that $b = \lambda^2$ where λ is predicted to be in the range 0.1 - 0.5 GeV/c. This corresponds to a prediction that b is the range 0.01 - 0.25 GeV^2/c^2. The above limit excludes most of the predicted range. The impact of this result on the importance or validity of the initial state corrections is difficult to assess. Just as the analysis of data is best done by those who acquire it, the interpretation of a model is perhaps best done by its architects. The model of Michael and Wilk predicts a dependence of $\langle P_T^2 \rangle$ on $A^{1/3}$ that is not linear but can be approximated in the beryllium to tungsten interval by equation 41 with b = 0.04 GeV^2/c^2. The data are not consistent with their model.

APPENDIX I

DRIFT CHAMBER HIT RECONSTRUCTION

This section describes the method by which spatial hit coordinates were reconstructed from raw drift chamber encoder information. The encoding system produced a channel address and 7-bit time for each hit. The channel address referred to one element of a 3594 element lookup table. Each element contained the plane, octant, and wire number of the hit. A longitudinal section of one octant of a detector plane is shown schematically in Figure 61. The sense wires of both the straight and skew chambers were numbered from one starting with the innermost wire and alternating between the upstream and downstream planes as one proceeded radially outward. The chambers were oriented such that wire #1 was always part of the upstream plane.

The condition for pairing hits from the upstream and downstream planes was that the sum of the encoder times be within ±15 encoder bins (9.3 nanoseconds per bin) of the nominal value. The expression for the sum of times is

$$T_1 + T_2 = 2T_D - (W + 2\Delta I s \ Tan\theta_X)/v_D \qquad (A1)$$

where: T_1 and T_2 are the encoder times of the upstream and downstream hits; T_D is the zero drift distance time; W is the wire spacing of the chamber (W = 1.00 inches for the straight chambers and W = 0.995 inches for the skew chambers); $\Delta I = I_1 - I_2$ are the wire numbers of the upstream

and downstream hits ($\Delta I = \pm 1$); s is the half depth of a drift cell (s = 0.438 inches); $\tan\theta_x$ is the projection of the polar track angle onto the x or u axis; and v_D is the drift velocity of the electrons in the drift cells (v_D = 0.020 inches per 9.3 nanosecond time bin). Equation A1 implies that the ±15 bin cut on the sum of times was equivalent to a cut of 330 milliradians on the local track angles. This was considerably larger than the spectrometer acceptance permitted. Note that equation A1 applies only for the smallest angle solution of the four that are possible when two wires fire (the track can pass on either side of each of the two wires). Only one of the remaining solutions corresponds to small enough angles to be realistic and only when the track passes very close to a wire. In this case, the error incurred by using the smallest angle solution is not significant. The origin of the local x-u coordinate system was taken to be the center of the first skew chamber wire. The x or u coordinate of some matched pair of hits was

$$x = w(I_1 - 1 - \Delta I/2) + \Delta I\ v_D\ (T_1 - T_2)/2 \qquad (A2)$$

where all quantities have been previously defined. The x or u coordinate of an unpaired hit was

$$x = w(I - 1) \pm v_D\ (T_D - T) \qquad (A3)$$

where I and T are the wire number and encoder time of the hit. As is obvious from equation A3, the encoder time measurements had a negative sense. The largest times corresponded shortest electron drifts. The z positions of reconstructed x or u hits were taken as the chamber centers for the paired hits and were displaced by ±s from the chamber centers for unpaired hits.

The final step in reconstructing the spatial hit coordinates

was to match the x and u hits in each octant and gap into points having the coordinates r, ϕ, z in the global cylindrical coordinate system. The condition for pairing some x and u hits was that the u coordinate fall between some limits $u_{MAX}(x)$ and $u_{MIN}(x)$ where the limits were

$$u_{MAX}(x) = x(\cos\Delta + \sin\Delta \tan\theta_0) + L_0 \sin\Delta + 0.45$$
$$u_{MIN}(x) = x(\cos\Delta - \sin\Delta \tan\theta_0) - L_0 \sin\Delta - 0.45 \quad \text{(A4)}$$

and where: $\Delta = 0.100$, the angle between the x and u axes; $\theta_0 = \pi/8$, the angle of the chamber sides with respect to the local x axis; and L_0 is the half length of the innermost chamber wire. The additional 0.45 inches added to the limits was to allow for track angle effects. Figure 62 shows the relationship of the local coordinate system in some octant and gap to the spectrometer axis and octant bisector. The dimensions labelled x_0 and y_0 are the distances from the spectrometer axis to origin of the local coordinate system in the local x and y directions (the nominal value of y was 0, nonzero values were indicated by a survey). The z position of the x, u pair was taken to be the mean of the z positions of the x and u hits. The track angle, either from the trigger pattern or from the first pass fit, was used to extrapolate the x and u coordinates from the z positions of their measurement to the mean z position. Typical "extrapolations" involved z displacements of one inch and track angles of 100 milliradians. The corrected x and u coordinates were then used to calculate the r, ϕ coordinates as follows

$$r = [(x' + x_0)^2 + (y + y_0)^2]^{1/2}$$
$$\phi = \tan^{-1}\left[\frac{y + y_0}{x' + x_0}\right] + \phi_0 \quad \text{(A5)}$$

where: x' is the track angle corrected x position; u' is the track angle corrected u position; $y = x' \cot\Delta = u' \csc\Delta$; and ϕ_o is the phi coordinate of the octant bisector.

APPENDIX II

TRACK FITTING

This section describes the track fitting procedure that was used by the reconstruction program. The fitting routine served two distinct purposes. The first was to supply some selection criterion to enable one to distinguish between charged particle tracks and random associations of drift chamber hits. The second function was to provide an estimate of the track parameters once the existence of a track had been established. Since the fitting routine was applied to all track coordinate permutations in each counter road, it was important that the fitting procedure not require much computer time. A number of approximations were made to accomplish this. Target associated tracks moved at fixed azimuth through the toroidal magnetic field. This enabled the radial and azimuthal track coordinates to be fit separately. The chi-squared function was defined in terms of the deviations of the measured track coordinates from an idealized path through the spectrometer. The deviations were dominated by multiple coulomb scattering in the spectrometer iron. This caused the deviations at different z positions to be correlated. The correct definition of the chi-squared function should therefore be non-diagonal. In the interest of speed and simplicity, a diagonal chi-squared definition was used. The total chi-squared was defined as

$$\chi^2 = \frac{1}{2}\,(\chi_R^2 + \chi_T^2) \tag{A6}$$

where χ_R^2 and χ_T^2, the radial and transverse chi-squared functions, were defined as

$$\chi_R^2 = \frac{1}{N-3} \sum_{i=1}^{N} \frac{[r_i - r(z_i)]^2}{\sigma_{R_i}^2} \tag{A7}$$

$$\chi_T^2 = \frac{1}{N-2} \sum_{i=1}^{N} \frac{r_i^2[\phi_i - \phi(z_i)]^2}{\sigma_{T_i}^2} \tag{A8}$$

and where: N is the number of hits on the track; r_i, ϕ_i, z_i are the coordinates of each hit; $r(z)$ is a three parameter function describing the radial motion of a charged particle in the toroidal magnetic field; $\phi(z)$ is a two parameter function describing the azimuthal motion of the particle; and σ_{R_i}, σ_{T_i} are suitably chosen standard deviations used to normalize the two chi-squared distributions. Note that χ_R^2 and χ_T^2 as defined in equations A7 and A8 are normalized to the number of degrees of freedom.

The function $r(z)$ was a function of three parameters: P_o, the momentum of the track at $z = 0$; θ_o, the polar angle of the track with respect to the z axis; and r_o, the radius of the track at $z = 0$. The function was composed of curved arcs in magnetized regions of the spectrometer and straight sections elsewhere. The shape of the curved segments was the approximate solution of the equations of motion for a highly relativistic charged particle in a uniform magnetic field with uniform energy loss,

$$(r - r_c)^2 + (z - z_c)^2 = \frac{c^2}{e^2B^2 + a^2}\,[P_I - a\,S\,(z)]^2 \tag{A9}$$

where:

$$r_c = r_I + \frac{P_I c}{e^2B^2 + a^2}\,[a \sin\theta_I + eB \cos\theta_I]$$

$$z_c = z_I + \frac{P_I c}{e^2B^2 + a^2}\,[a \cos\theta_I - eB \sin\theta_I]$$

a is the energy loss per unit track length; B is the azimuthal magnetic field in the iron; r_I, z_I, θ_I, and P_I are the track coordinates, polar angle, and momentum at entry into the iron; and S(z) is the arc length along the track at the point z. Equation A9 could have been used to generate a differential equation for the arc length S(z). This was unnecessary since a circular arc approximation adequately reproduced the track shape. The magnetic field used in the solution was the average field along the circular arc that was used to approximate S. The energy loss for muons traversing iron has been both calculated and measured. The probability distribution for the sum of the various loss mechanisms has a narrow maximum at approximately 30 MeV/inch with a long energy dependent tail (due chiefly to radiative processes). It was unclear whether the most probable value or the mean value was appropriate to use in equation A9. The solution was to generate a number of Monte Carlo tracks using the correct distribution and to fit equation A9 to the tracks by treating the energy loss as a free parameter. The results are shown in Figure 63. In general, a value of a = dE/dS that was intermediate between the most probable value and the mean best reproduced the Monte Carlo tracks.

The standard deviations used in the radial fit were derived from the well known expression for multiple coulomb scattering in a plane,

$$\sigma_R = \frac{1}{\sqrt{3}} \frac{0.015}{P} \frac{1}{\sqrt{x_o}} L^{3/2} \qquad (A10)$$

where: P is the particle momentum in GeV/c; x_o is the radiation length of the material (x_o = 0.693 inches for iron); and L is the length of material traversed.

The dependence of $r(z, P_o, \theta_o, r_o)$ on the parameters P_o and θ_o is very nonlinear. Therefore, the radial chi-squared function was minimized by Newton's method. The upstream three points on the track were used to generate a first guess for the fit parameters $\bar{P}_o$, $\bar{\theta}_o$, $\bar{r}_o$. These, in turn, were used to calculate a first guess chi-squared, $\bar{\chi}^2_R$. The true χ^2_R function can be expanded in a power series in the parameters about this point,

$$\chi^2_R(a) = \bar{\chi}^2_R + \sum_{i=1}^{3} \frac{\partial \chi^2_R}{\partial a_i} \Big|_{\bar{a}} (a_i - \bar{a}_i) + \frac{1}{2} \sum_{i,j=1}^{3} \frac{\partial^2 \chi^2_R}{\partial a_i \partial a_j} \Big|_{\bar{a}} (a_i - \bar{a}_i)(a_j - \bar{a}_j) \qquad A11)$$

where a_i refers to the parameters and all terms beyond second order were ignored. The extremum condition, that all first derivatives of vanish, leads to the solution

$$a_i = \bar{a}_i - \sum_{j=1}^{3} M_{ij} \left(\frac{\partial \chi^2_R}{\partial a_j}\right) \Big|_{\bar{a}} \qquad (A12)$$

where the matrix M_{ij} is defined as $M^{-1}_{ij} = \frac{\partial^2 \chi^2_R}{\partial a_i \partial a_j} \Big|_{\bar{a}}$. The quantities in equation M12 can be written in terms of r(z),

$$\frac{\partial \chi^2_R}{\partial a_j} \Big|_{\bar{a}} = \frac{-2}{N-3} \sum_{i=1}^{N} \frac{[r_i - r(z_i)]}{\sigma^2_{R_i}} \frac{\partial r(z_i)}{\partial a_j} \Big|_{\bar{a}} \qquad (A13)$$

$$M^{-1}_{jk} = \frac{2}{N-3} \sum_{i=1}^{N} \frac{1}{\sigma^2_{Ri}} \left[\frac{\partial r}{\partial a_j} \frac{\partial r}{\partial a_k} - (r_i - r(z_i)) \frac{\partial^2 r}{\partial a_j \partial a_k}\right] \Big|_{\bar{a}} \qquad (A14)$$

In practice, one can ignore the second derivative in equation A14. Equation A12 was the basis of an iterative solution. The new values of the parameters were used to recalculate and the process was iterated until the fractional improvement in χ^2_R was less than 1%. This typically required three iterations. The radial fitting routine also operated in target constrained mode. This involved removing the row and column of M^{-1} that corresponded to r_o and setting $r_o = z_{TGT}\theta_o$ (z_{TGT} was the z position of the target center).

The sensitive kinematic parameters of each track, P_o and were Θ_o determined solely from the radial fitting procedure. The purpose of the aximuthal fit was one of track definition. Therefore a number of simplifying approximations were made. It was decided to ignore energy loss and radial magnetic field components (the radial components were essentially 0 except near the octagonal edges of the downstream magnets). The azimuthal motion of a particle in the spectrometer is then described by a conservation of angular momentum equation,

$$r^2 \frac{d\phi}{dS} = V_y \qquad (A15)$$

where V_y is the angular momentum about the spectrometer axis. The solution of equation A15 is

$$\phi(z) = \phi_I + V_y F(z) \qquad (A16)$$

where ϕ_I is the azimuth of the track at z_I = 54.5 inches (immediately upstream of TM1) and F(z) is the integral

$$F(z) = \int_{z_I}^{z} \frac{dS}{r^2} \tag{A17}$$

Since energy loss was ignored, equation A17 was evaluated for a circular track shape. This was a fair approximation if the average momentum $\bar{P}$ and the average magnetic field $\bar{B}$ were used to calculate the radius of the circle, R,

$$R = \frac{\bar{P}C}{e\bar{B}} \tag{A18}$$

Note that R is a signed quantity. The sign of R reflects the sign of the charge of the particle. The coordinates of the center of the circle are

$$\begin{aligned} r_c &= r_I + R\cos\theta_o \\ z_c &= z_I - R\sin\theta_o \end{aligned} \tag{A19}$$

where $r_I = r_o + z_I \tan\theta_o$, the radius of the track at z_I. The points on the circle can be parametized in terms of the polar angle θ,

$$\begin{aligned} r &= r_c - R\cos\theta \\ z &= z_c + R\sin\theta \end{aligned} \tag{A20}$$

Using this parametization, the integral in equation A17 is trivially evaluated as

$$F(z) = \begin{cases} \frac{R}{\alpha^2}\left\{\frac{(z-z_c)}{r} - \frac{(z_I-z_c)}{r_I} + \frac{2r_c}{\alpha}\left[\tan^{-1}\left(\frac{\alpha\tan\theta/2}{r_c-R}\right) - \tan^{-1}\left(\frac{\alpha\tan\theta_o/2}{r_c-R}\right)\right]\right\} & R>0 \\ \frac{R}{\alpha^2}\left\{\frac{(z-z_c)}{r} - \frac{(z_I-z_c)}{r_I} + \frac{r_c}{\alpha}\ln\left[\left(\frac{\alpha\tan\theta/2+(r_i-R)}{\alpha\tan\theta/2-(r_c-R)}\right)\left(\frac{\alpha\tan\theta_o/2-(r_c-R)}{\alpha\tan\theta_0/2+(r_c-R)}\right)\right]\right\} & R<0 \end{cases} \tag{A21}$$

where $\alpha = (r_c - R^2)^{1/2}$.

The standard deviations used in equation A8 for the transverse chi-

squared were twice used in the radial fit. This was done to empirically normalize the radial and transverse distributions to the same mean. The difference was due, at least in part, to the fact that the transverse resolution of the drift chamber system was a factor of ten worse than the radial resolution and comparable to the multiple scattering.

The minimization of χ_T^2 was trivial since $\phi(z)$ is a linear function of the parameters ϕ_I and ν_y. Without further elaboration, the expressions for ϕ_I and ν_y are

$$\phi_I = \frac{1}{D}\left[\sum_{i=1}^{N}\frac{r_i^2\phi_i}{\sigma_{Ti}^2}\sum_{i=1}^{N}\frac{r_i^2F^2(z_i)}{\sigma_{Ti}^2} - \sum_{i=1}^{N}\frac{r_i^2F(z_i)\phi_i}{\sigma_{Ti}^2}\sum_{i=1}^{N}\frac{r_i^2F(z_i)}{\sigma_{Ti}^2}\right] \qquad \text{(A22)}$$

$$\nu_y = \frac{1}{D}\left[\sum_{i=1}^{N}\frac{r_i^2}{\sigma_{Ti}^2}\sum_{i=1}^{N}\frac{r_i^2\phi_iF(z_i)}{\sigma_{Ti}^2} - \sum_{i=1}^{N}\frac{r_i^2\phi_i}{\sigma_{Ti}^2}\sum_{i=1}^{N}\frac{r_i^2F(z_i)}{\sigma_{Ti}^2}\right] \qquad \text{(A23)}$$

where $$D = \sum_{i=1}^{N}\frac{r_i^2}{\sigma_{Ti}^2}\sum_{i=1}^{N}\frac{r_i^2F^2(z_i)}{\sigma_{Ti}^2} - \left[\sum_{i=1}^{N}\frac{r_i^2F(z_i)}{\sigma_{Ti}^2}\right]^2$$

The actual fitting procedure involved two passes. The coordinates of some permutation of hits were fit according to the procedure just outlined. The track angles at each detector plane were then calculated and used to correct the x-u matching as outlined in Appendix I. The new cylindrical coordinates were then refit, again using the above procedure. The effect of the angle correction was to dramatically improve the chi-squared distributions and the resolution of the parameter estimation.

APPENDIX III

SECONDARY PION PRODUCTION AND BEAM ENERGY BROADENING

The effect of inelastic pion scattering in the experimental target was considered for an incident beam having the energy distribution shown in Figure 6. Let $\frac{d\sigma}{dE}(E, E')$ be the differential cross section for a pion of energy E' to inelastically scatter to energy E. It is straightforward to derive the following equation for the beam flux density $n_\pi(\vec{x}, E)$,

$$\frac{\partial n}{\partial z}_\pi(\vec{x}, E) = - \frac{1}{\lambda_{ABS}} n_\pi(\vec{x}, E) + \frac{\rho_M N_o}{A} \int_E^{E_{MAX}} dE' \; n_\pi(\vec{x}, E') \frac{d\sigma}{dE}(E, E') \qquad (A24)$$

where E_{MAX} is the maximum energy of the incident beam and λ_{ABS} is the total inelastic absorbtion length. The absorbtion length[44] is related to the total inelastic cross section $\sigma_{inel}(E)$ by the expression,

$$\lambda_{ABS}^{-1} = \frac{\rho_M N_o}{A} \sigma_{inel}(E) \qquad (A25)$$

The total cross section is approximately independent of energy. This enables one to write the flux density as

$$n_\pi(\vec{x}, E) = \frac{N\pi}{\pi R^2} e^{-z/\lambda_{ABS}} \hat{n}(z, E) \qquad (A26)$$

where the assumption of uniform illumination has been invoked and where: N_π is the total number of pions incident upon the target; R is the radius

of the target; z is the distance measured from the upstream end of the target; and $\hat{n}(z, E)$ is an evolution function. Substituting equation A26 into equation A24, an equation for $\hat{n}(z, E)$ is readily attained,

$$\frac{\partial \hat{n}}{\partial z}(z, E) = \frac{\rho_M N_o}{A} \int_E^{E_{MAX}} dE' \; \hat{n}(z, E') \frac{d\sigma}{dE}(E, E') \tag{A27}$$

At high energies (E > 10-20 GeV) the inelastic cross section has weak energy dependence and is a function only of the ratio x = E/E'. In this approximation, equation A27 can be rewritten as

$$\frac{\partial \hat{n}}{\partial z}(z, E) = \frac{\rho_M N_o}{A} \int_{E/E_{MAX}}^{1} dx \; \frac{1}{x} \frac{d\sigma}{dx} \hat{n}(z, E/x) \tag{A28}$$

Equation A28 was used to numerically evolve $\hat{n}(z, E)$ in z and E. The inelastic cross section for pion scattering has been measured by Fermilab M6 Single Arm Spectrometer Group.[45] Their measurements include data on both hydrogen and nuclear targets. The shape of the P_T integrated differential cross section $d\sigma/dx$ is well measured only for the hydrogen data. A plot of their measurements for x between 0.6 and 0.96 is shown in Figure 64. A fit to the form $xd\sigma/dx = x[a(1-x) + b(1-x)^{-1}]$ is also shown. This shape was then normalized to the nuclear cross section scaled with atomic mass as $A^{0.6}$. Using the best estimates for a and b obtained from the fit shown in Figure 64, the cross section used in equation A28 was

$$\frac{d\sigma}{dx} = [24.5(1-x) + 1.00(1-x)^{-1}] \, A^{0.6} \text{ millibarns} \tag{A29}$$

The evolution function evaluated at z = 0, $\hat{n}(0, E)$, reflected the

incident beam energy distribution and was normalized to unity,

$$\int_{E_{MIN}}^{E_{MAX}} dE \quad \hat{n}(0, E) = 1.0 \tag{A30}$$

where E_{MIN} was some convenient lower bound (set to 140 GeV for this calculation). For $z > 0$, the integral was larger than 1 indicating a departure from the purely exponential attenuation of the naive case, $\hat{n}(z, E) = \hat{n}(0, E)$. The typical increase was approximately 5% over the lengths of the targets. Since the A dependence of the large x inelastic cross section differed from the $A^{2/3}$ scaling of the total inelastic cross section, the z dependence of $n_{\pi}(\vec{x}, E)$ does not scale in absorbtion lengths and a different distribution was generated for each target. The results for the beryllium and tungsten targets are shown in Figures 65 and 66.

REFERENCES

1. J.H. Christenson et al., Phys. Rev. Lett. 25, 1523 (1970).

2. S.D. Drell and T.-M. Yang, Phys. Rev. Lett. 25, 316 (1970).

3. There are a number of excellent reviews of the Drell-Yan process in print. Several recent ones are: R. Stroynowski, Physics Reports C71, 1 (1981); E.L. Berger, ANL-HEP-82-68, November 1982; I.R. Kenyon, Rept. Math. Phys. 45, 1261 (1982).

4. The Drell-Yan process has been used to measure the nucleon valence and sea quark structure functions. See: J. Badier et al., Phys. Lett. 89B, 145 (1979) and Phys. Lett. 96B, 422 (1980); A.S. Ito et al., Phys. Rev. D23, 604 (1981); S.R. Smith et al., Phys. Rev. Lett. 46, 1607 (1981).

5. The structure functions of the pion are accessible only via Drell-Yan experiments. See: R. Barate et al., Phys. Rev. Lett. 43, 1541 (1979); C.B. Newman et al., Phys. Rev. Lett. 42, 951 (1979); J. Badier et al., CERN-EP/80-148, August 1980; M.J. Corden et al., Phys. Lett. 96B, 417 (1980).

6. The results listed in Table 1 are those of Badier et al. (see Ref. 7) that were obtained by constraining the nucleon structure functions to those measured in deep inelastic neutrino scattering by the CDHS collaboration, J.G.H. de Groot et al., Phys. Lett. 82B, 456 (1979) and Zeit für Physik C1, 143 (1979).

7. See, for example, the total inelastic cross sections given in Reference 43.

8. D. Antreasyan et al., Phys. Rev. D19, 764 (1979); H.J. Frisch et al., Phys. Rev. D27, 1001 (1983).

9. The observation of jets in fixed target experiments is fairly tenuous and the A dependence of such may be meaningless. Nonetheless, an anomalous A dependence was published by C. Bromberg et al., Phys. Rev. Lett. 42, 1202 (1979).

10. The evidence for the large hadronization distance of quarks in high energy interactions comes chiefly from studies of the multiplicities of secondary hadrons in proton-nucleus and nucleus-nucleus collisions. See: W. Busza et al., Phys. Rev. Lett. 34, 836 (1975); C. Halliwell et al., Phys. Rev. Lett. 39, 1499 (1977); J.E. Elias et al., Phys. Rev. Lett. 41, 285 (1978); T. Akesson et al., Nucl. Phys. B209, 321 (1982).

11. Some evidence for non-scaling of the Drell-Yan cross section was presented by the CERN NA10 collaboration at the 1983 Recontres de Moriond, La Plagne France, J. Varela, University of Paris preprint LPNHE/X 83-02 (1983).

12. M.J. Corden et al., Phys. Lett. 76B, 226 (1978); M.A. Abolins et al., Phys. Lett. 82B, 145 (1979); G.E. Hogan et al., Phys. Rev. Lett. 42, 948 (1979); D. Antreasyan et al., Phys. Rev. Lett. 45, 863 (1980); C. Koukemelis et al., Phys. Lett. 91B, 475 (1980); J. Badier et al., Zeit für Physik C11, 195 (1981).

13. K.J. Anderson et al., Phys. Rev. Lett. 42, 944 (1979); A.L.S. Angelis et al., Phys. Lett. 87B, 398 (1979); D. Antreasyan et al., Phys. Rev. Lett. 47, 12 (1981); J. Badier et al., Phys. Lett. 117B, 372 (1982). See also A.S. Ito et al. (Reference 4).

14. See I.R. Kenyon (Reference 3) and J. Badier et al. (Reference 13).

15. See K.J. Anderson et al. (Reference 13).

16. J. Badier et al., Phys. Lett. 104B, 335 (1981).

17. The K factor has been measured for various beams and targets by several techniques: J. Badier et al., Phys. Lett. 89B, 145 (1979); L. Lefrancois, Proc. XX Int. Conf. on High Energy Physics, Madison, 1980 (New York: AIP Conf. Proc. No. 68); D. Antreasyan et al., MIT Report 119, 1981; E. Anassontzis et al., Fermilab CONF-82/50-EXP, 1982. See also all entries in Reference 4 and C. Koukemelis et al. (Reference 12).

18. H.D. Politzer, Nucl. Phys. B129, 497 (1977).

19. C.T. Sachrajda, Phys. Lett. 73B, 185 (1978).

20. J. Kubar and F. Paige, Phys. Rev. D19, 221 (1978); G. Altarelli, R.K. Ellis, and G. Martinelli, Nucl. Phys. B157, 461 (1979); B. Humpert and W.L. Neervan, Phys. Lett. 89B, 69 (1979); J. Kubar, M. Le Bellac, J.L. Meunier, and G. Flaut, Nucl. Phys. B175, 251 (1979).

21. G. Curci and M. Greco, Phys. Lett. 92B, 175 (1980); G. Parisi, Phys. Lett. 90B, 295 (1980).

22. G. Altarelli, G. Parisi, and R. Petronzio, Phys. Lett. 76B, 351 and 356 (1978); H. Fritsch and P. Minkowski, Phys. Lett. 73B, 80 (1978); K. Kagante and R. Raitio, Nucl. Phys. B139, 72 (1978).

23. F. Halzen and D.M. Scott, Phys. Rev. D24, 2433 (1981).

24. R.K. Ellis, G. Martinelli, and R. Petronzio, Phys. Lett. 104B, 45 (1981).

25. P. Chiappetta and M. Greco, Phys. Lett. 106B, 219 (1981): F. Halzen and D.M. Scott, Phys. Rev. D21, 131 (1981).

26. G.T. Bodwin, S.J. Brodsky, and G.P. Lepage, Phys. Rev. Lett. 47, 1799 (1981) and SLAC-PUB-2927, May 1982.

27. W.W. Lindsay, D. Ross and C.T. Sachrajda, Southampton report SHEP 81/82-6 (1982).

28. C. Michael and G. Wilk, Zeit fur Physik C10, 169 (1981).

29. See J. Badier et al. (Reference 13).

30. N.D. Giokaris, Ph.D. thesis, University of Chicago, 1981, (unpublished).

31. J. Hawkins, private communication.

32. W.F. Baker et al., Fermilab PUB-74/13-EXP, 1974; H.W. Atherton et al., CERN 80-07, SPS Division, August 1980.

33. Particle Data Group, LBL-100 Revised UC-34d, April 1982.

34. A more complete description of the trigger can be found in the following publication, A. Halling, M. Isaila, and R. Sumner, IEEE Transactions on Nuclear Science, vol. NS-29, 437 (February 1982).

35. The drift chamber system is described in some detail in the following publication: H.J. Frisch et al., IEEE Transactions on Nuclear Science, vol. NS-27, 150 (February 180).

36. See H.J. Frisch et al. (Reference 8).

37. M. Mugge, private communication

38. E.J. Monitz et al., Phys. Rev. Lett. 26, 445 (1971).

39. A. Bodek and J.L. Ritchie, Phys. Rev. D23, 1070 (1981).

40. O. Callot, Ph.D. thesis, University of Paris, 1981.

41. J. Badier et al., CERN-EP/79-61, June 1979.

42. J. Badier et al., CERN-EP/80-149, August 1980.

43. Y.M. Antipov et al., Phys. Lett. 76B, 235 (1978). See also K.J. Anderson et al., (Reference 13) and J. Badier et al. (References 41 and 42).

44. The absorption lengths for all targets were calculated from the total inelastic cross sections measured by A.S. Carroll et al., Phys. Lett. 80B, 319 (1979).

45. A.E. Brenner et al., Phys. Rev. Lett. 37, 1724 (1976); Phys. Rev. Lett. 38, 880 (1977); Fermilab CONF-80/147-EXP, 1980; Fermilab PUB-81/82-EXP, December 1981.

TABLE 1

NA3 AND CDHS STRUCTURE FUNCTIONS

$F(x) = A\, x^{\alpha}\, (1-x)^{\beta}$

Structure Function	f(x)	A	α	β
Proton U Quark	U(x)	2.27	0.52	2.8
Proton d Quark	D(x)	1.29	0.52	3.8
Nucleon Sea	Sn(x)	0.27	0	8
Pion Valence	$V\pi(x)$	0.66	0.45	1.04
Pion Sea	$S\pi(x)$	0.25	0	5.4

TABLE 2

E326 A DEPENDENCE TARGETS

Target	Atomic Mass	Measured Density (g/cm^3)	Density of Pure Material (g/cm^3)	Length (inches)	Length (λABS)	Length (Rad. Lengths)
Beryllium	9.000	1.85	1.85	7.00	0.307	0.504
Copper	63.62	8.89	8.96	3.00	0.403	5.33
Tin	119.1	7.27	7.27	4.50	0.419	9.45
Tungsten	183.9	18.1	19.3	2.09	0.438	15.2

TABLE 3

E325 TOROIDAL IRON MAGNETS

Magnet	Shape	Inner Radius (inches)	Outer Radius (inches)	Length (inches)	Amp-Turns	Average Magnetic Field (KG)
TM1	Cylinder	2.50	24.00	55.88	24000	18.0
TM2	Cylinder	4.75	35.00	55.75	28800*	17.6
A	Octagonal Prism	6.69	47.00+	56.25	48000	18.4
B	Octagonal Prism	8.75	47.00+	56.25	48000	18.3
C	Octagonal Prism	10.81	47.00+	56.25	48000	18.2
D	Octagonal Prism	12.81	47.00+	56.25	48000	18.1
E	Octagonal Prism	14.88	47.00+	56.25	48000	17.7

+Minor Radius

*Includes the effect of a shorted coil assembly.

TABLE 4

TRIGGER HODOSCOPES

Plane	Radius[+] of Inner Edge (inches)	Radius[+] of Outer Edge (inches)	Number of Counters per Octant	Width of Counters (inches)	Total Number of Counters
1	5.125	23.625	5	4x4.00", 1x2.00" per Octant	40
2	7.250	34.500	7	6x4.00", 1x2.50" per Octant	56
3	9.250	46.625	5	7.38	40
4	11.125	46.625	5	7.00	40
5	13.250	46.625	4	8.25	32
6	15.250	46.625	4	7.75	32
7	17.250	46.625	4	7.25	32
			34		272

[+]Minor Radius

TABLE 5

TYPICAL HARDWARE TRIGGER RATES
(DURING THE ONE SECOND BEAM SPILL)

Beam Flux	5×10^8 sec^{-1}
Interactions in the Target	2.5×10^8 sec^{-1}
Muons in the Beam Halo	5×10^6 sec^{-1}
Plane 1 Scintillation Counters	$<1 \times 10^6$ sec^{-1} per counter
M12	1×10^5 sec^{-1} per octant
M23	1×10^5 sec^{-1} per octant
M4 ("OR")	1×10^6 sec^{-1} per octant
M12*M23*M4	1×10^4 sec^{-1} per octant
First Level Trigger	160 sec^{-1}
W/Veto (starts to trigger processor)	120 sec^{-1}
Final Trigger	6 sec^{-1}

TABLE 6

DRIFT CHAMBER DIMENSIONS

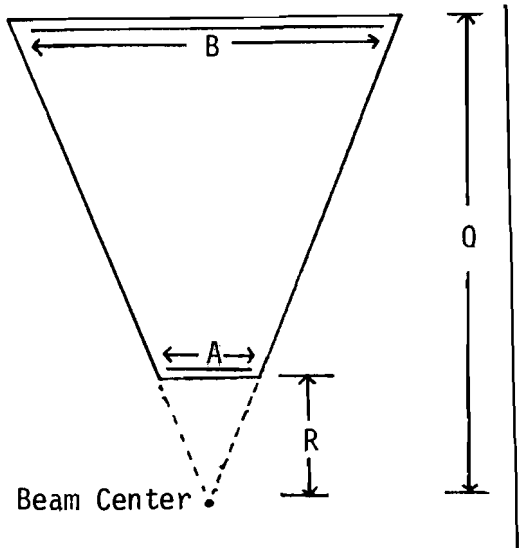

Gap	Number of Chambers	Number of Wires per Chamber	Radius of Inner Edge, R (inches)	Radius of Outer Edge, O (inches)	A (inches)	B (inches)
1	16	18	5"	24"	3.04	17.12
2	16	27	7"	35"	4.68	26.22
3	16	37	9"	47"	6.29	36.11
4	16	35	11"	47"	7.94	36.11
5	16	33	13"	47"	9.61	36.12
6	16	31	15"	47"	11.26	36.11
7	16	29	17"	47"	12.96	36.16

TABLE 7

EVENT SELECTION

	Events in Data Sample (All Targets)
Total Sample	63,131
Opposite Sign, >2 Muons	20,365
Topology Cut	18,197
Chi-Squared Cut	8,801
Target Angle Cut	809
Target Radius Cut	455
Multimuon Cut	454
Trigger Cut	452
Target Constrained Chi-Squared	399
Fiducial Octant Cut	396
Mass ≥ 4 GeV/c^2	320

TABLE 8

A DEPENDENCE DATA, NORMAL CUTS

Target	Target Ion Chamber	Collimator Ion Chamber	All Masses Events	All Masses Accidentals	Mass >4 GeV/c^2 Events	Mass >4 GeV/c^2 Accidentals	8.5 GeV/c^2>Mass>4 GeV/c^2 Events	8.5 GeV/c^2>Mass>4 GeV/c^2 Accidentals
Beryllium	342.747	47.231	170.0	15.52±1.33	135.0	7.92±0.68	115.0	7.79±0.67
Copper	58.285	7.907	51.0	4.93±0.84	41.0	2.94±0.50	32.0	2.80±0.48
Tin	57.247	7.658	71.0	2.60±0.54	60.0	1.50±0.31	50.0	1.46±0.30
Tungsten	93.356	13.695	104.0	6.88±0.98	84.0	3.46±0.49	75.0	3.36±0.48
Out	103.433	16.425	6.0	.87±0.25	4.0	.45±0.13	4.0	.44±0.13

TABLE 9

EVENT AND BACKGROUND TOTALS, NORMAL CUTS

Target	Target Ion Chamber	Events	All Masses Accidentals	Target Out	Total Events
Beryllium	342.747	170.0	15.52±1.33	14.76±7.08	139.72±14.90
Copper	58.285	51.0	4.93±0.84	2.47±1.19	43.60±7.29
Tin	57.247	71.0	2.60±0.54	2.39±1.15	66.01±8.52
Tungsten	93.356	104.0	6.88±0.98	4.28±2.05	92.84±10.45
All	551.634	396.0	29.93±1.93	23.90±11.47	342.17±21.85
			Mass >4 GeV/c^2		
Beryllium	342.747	135.0	7.92±0.68	10.21±5.76	116.87±12.99
Copper	58.285	41.0	2.94±0.50	1.71±0.96	36.35±6.49
Tin	57.247	60.0	1.50±0.31	1.66±0.93	56.84±7.81
Tungsten	93.356	84.0	3.46±0.49	2.96±1.67	77.57±9.33
All	551.634	320.0	15.83±1.02	16.54±9.33	287.64±19.39
			8.5 GeV/c^2 > Mass >4 GeV/c^2		
Beryllium	342.747	115.0	7.79±0.67	10.23±5.76	96.97±12.19
Copper	58.285	32.0	2.80±0.48	1.71±0.96	27.49±5.76
Tin	57.247	50.0	1.46±0.30	1.66±0.93	46.89±7.14
Tungsten	93.356	75.0	3.36±0.48	2.96±1.67	68.68±8.83
All	551.634	272.0	15.40±1.00	16.57±9.33	240.03±18.11

TABLE 10

A DEPENDENCE DATA, LOOSE CUTS

Target	Target Ion Chamber	Collimator Ion Chamber	All Masses Events	All Masses Accidentals	Mass >4 GeV/c Events	Mass >4 GeV/c Accidentals	8.5 GeV/c^2>Mass>4 GeV/c^2 Events	8.5 GeV/c^2>Mass>4 GeV/c^2 Accidentals
Beryllium	342.747	47.231	264.0	71.51±4.03	192.0	40.52±2.28	168.0	38.84±2.19
Copper	58.285	7.907	71.0	25.02±2.62	54.0	15.63±1.64	45.0	14.69±1.54
Tin	57.247	7.658	94.0	17.48±2.07	73.0	9.93±1.18	63.0	9.36±1.11
Tungsten	93.356	13.695	159.0	29.91±2.74	116.0	16.57±1.52	104.0	15.64±1.43
Out	103.433	16.425	19.0	5.46±0.92	16.0	2.92±0.49	14.0	2.83±0.48

TABLE 11

EVENTS AND BACKGROUND TOTALS, LOOSE CUTS

Target	Target Ion Chamber	Events	All Masses Accidentals	Target Out	Total Events
Beryllium	342.747	264.0	71.51±4.03	38.94±12.81	153.55±21.08
Copper	58.285	71.0	25.02±2.62	6.52±2.14	39.46±9.08
Tin	57.247	94.0	17.48±2.07	6.31±2.08	70.20±10.13
Tungsten	93.356	159.0	29.91±2.74	11.29±3.71	117.80±13.43
All	551.634	588.0	143.92±5.90	63.07±20.75	381.01±29.09
			Mass >4 GeV/c^2		
Beryllium	342.747	192.0	40.52±2.28	37.61±11.59	113.88±18.21
Copper	58.285	54.0	15.63±1.64	6.30±1.94	32.08±7.77
Tin	57.247	73.0	9.93±1.18	6.10±1.88	56.98±8.83
Tungsten	93.356	116.0	16.57±1.52	10.90±3.36	88.52±11.38
All	551.634	435.0	82.64±3.40	60.90±18.77	291.46±25.60
			8.5 GeV/c^2 > Mass >4 GeV/c^2		
Beryllium	342.747	168.0	38.84±2.19	32.11±10.85	97.06±17.04
Copper	58.285	45.0	14.69±1.54	5.38±1.82	24.94±7.12
Tin	57.247	63.0	9.36±1.11	5.21±1.76	48.43±8.21
Tungsten	93.356	104.0	15.64±1.43	9.31±3.15	79.05±10.77
All	551.634	380.0	78.53±3.23	52.00±17.57	249.47±23.84

TABLE 12

AVERAGE DRIFT CHAMBER EFFICIENCIES

Run	Target	Gap 1X	Gap 1U	Gap 1	Gap 2X	Gap 2U	Gap 2
600	W	0.62±.01	0.65±.01	0.87±.01	0.85±.01	0.86±.01	0.73±.01
601-602	Be	0.64±.01	0.68±.01	0.88±.01	0.85±.01	0.87±.01	0.74±.01
608	Be	0.65±.01	0.67±.01	0.89±.01			
609-610	Cu	0.62±.01	0.62±.01	0.86±.01			
611	Be	0.65±.01	0.68±.01	0.89±.01			
612	Sn	0.62±.01	0.63±.01	0.86±.01			

TABLE 13

CHI SQUARED TEST OF THE CONSTANT RATES HYPOTHESIS FOR FIGURE 49

Target	Mean Rate (arbitrary units)	χ^2/DOF
Beryllium	0.38	16.7/15
Copper	0.83	1.5/2
Tin	1.1	3.1/2
Tungsten	0.94	5.5/5

TABLE 14

EFFECTIVE CROSS SECTION PER NUCLEON

Target	Live Flux	Total Events	Cross Section (Arbitrary Units)
Beryllium	342.75	96.97±12.19	0.997±.125
Copper	58.29	27.49±5.76	0.847±.177
Tin	57.25	46.89±7.14	1.207±.184
Tungsten	93.36	68.68±8.83	0.946±0.122

TABLE 15

A DEPENDENCE FITS

Fit	χ^2/DOF	Normalization	Exponent
Model Independent	2.2/2	0.985±0.235	1.00±0.06
Model Dependent	2.7/2	1.05±0.25	0.97±0.06

TABLE 16

THE DRELL YAN MODEL FOR THE EFFECTIVE CROSS SECTION, $\sigma'(Z/A)$

Target	Z/A	Monte Carlo	Simple Calculation
Beryllium	0.444	1.00±0.02	1.00
Copper	0.456	1.14±0.03	1.01
Tin	0.420	1.10±0.03	0.99
Tungsten	0.402	1.09±0.03	0.97
Nickel	0.476	1.15±0.03	1.02

TABLE 17

$\langle P_T^2 \rangle$ FOR VARIOUS TARGETS

Target	$\langle P_T^2 \rangle$ (GeV^2/c^2)
Beryllium	1.83±.18
Copper	2.02±.32
Tin	1.50±.18
Tungsten	1.65±.18

TABLE 18

$\langle P_T^2 \rangle$ FITS

Fit	χ^2/DOF	a(GeV^2/c^2)	b(GeV^2/c^2)
Constant	2.81/3	1.69±0.10	----
Linear	1.64/2	2.02±0.30	-0.079±0.073

TABLE 19

SYSTEMATIC UNCERTAINTIES FOR THE A DEPENDENCE MEASUREMENT

(all numbers are in percent)

Target	$\frac{\Delta N_\pi}{N_\pi}$	$\frac{\Delta \epsilon}{\epsilon}$	$\frac{\Delta \sigma tot}{\sigma tot}$	$\frac{\Delta M}{M}$	$\frac{\Delta a}{a}$	$\frac{\Delta \sigma eff}{\sigma eff}$
Beryllium	1.0	3.6	3.0	.025	0.12	3.8
Copper	1.0	3.6	3.0	.012	0.12	3.8
Tin	1.0	3.6	3.0	.0095	0.20	3.8
Tungsten	1.0	3.6	3.0	.0021	0.32	3.8

TABLE 20

$\langle P_T^2 \rangle$ FOR VARIOUS ACCEPTANCES

Target	(all values in GeV^2/c^2) Normal Acceptance	Flat Acceptance	Steep Acceptance
Beryllium	1.83±0.18	1.85±0.18	1.82±0.18
Copper	2.02±0.32	2.03±0.33	2.00±0.32
Tin	1.50±0.18	1.50±0.18	1.49±0.18
Tungsten	1.65±0.18	1.66±0.19	1.64±0.18

TABLE 21

FITS TO $\langle P_T^2 \rangle = a + b\, A^{1/3}$ FOR VARIOUS SYSTEMATIC UNCERTAINTIES

Acceptance for							
Beryllium	Copper	Tin	Tungsten	χ^2/DOF	a(GeV^2/c^2)	b(GeV^2/c^2)	90% Confidence Limit on b(GeV^2/c^2)
Normal	Normal	Normal	Normal	1.64/2	2.02±0.32	-0.079±0.073	0.015
Steep	Normal	Normal	Normal	1.66/2	2.00±0.32	-0.074±0.073	0.019
Normal	Normal	Normal	Flat	1.68/2	2.02±0.32	-0.077±0.074	0.017
Steep	Normal	Normal	Flat	1.69/2	1.99±0.32	-0.072±0.073	0.021

Figure 1.--A typical Drell-Yan diagram for a meson nucleon interaction.

Fig. 1

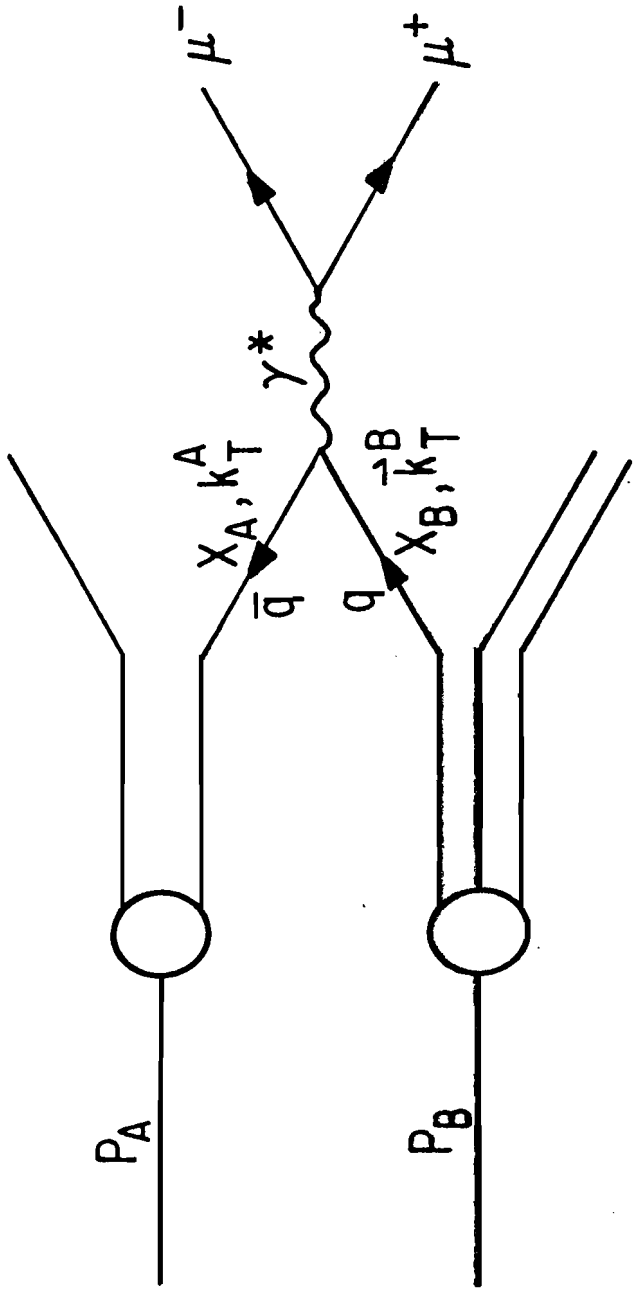

Figure 2.--The basic subprocess (top) along with some lowest order QCD subprocesses (below).

Fig. 2

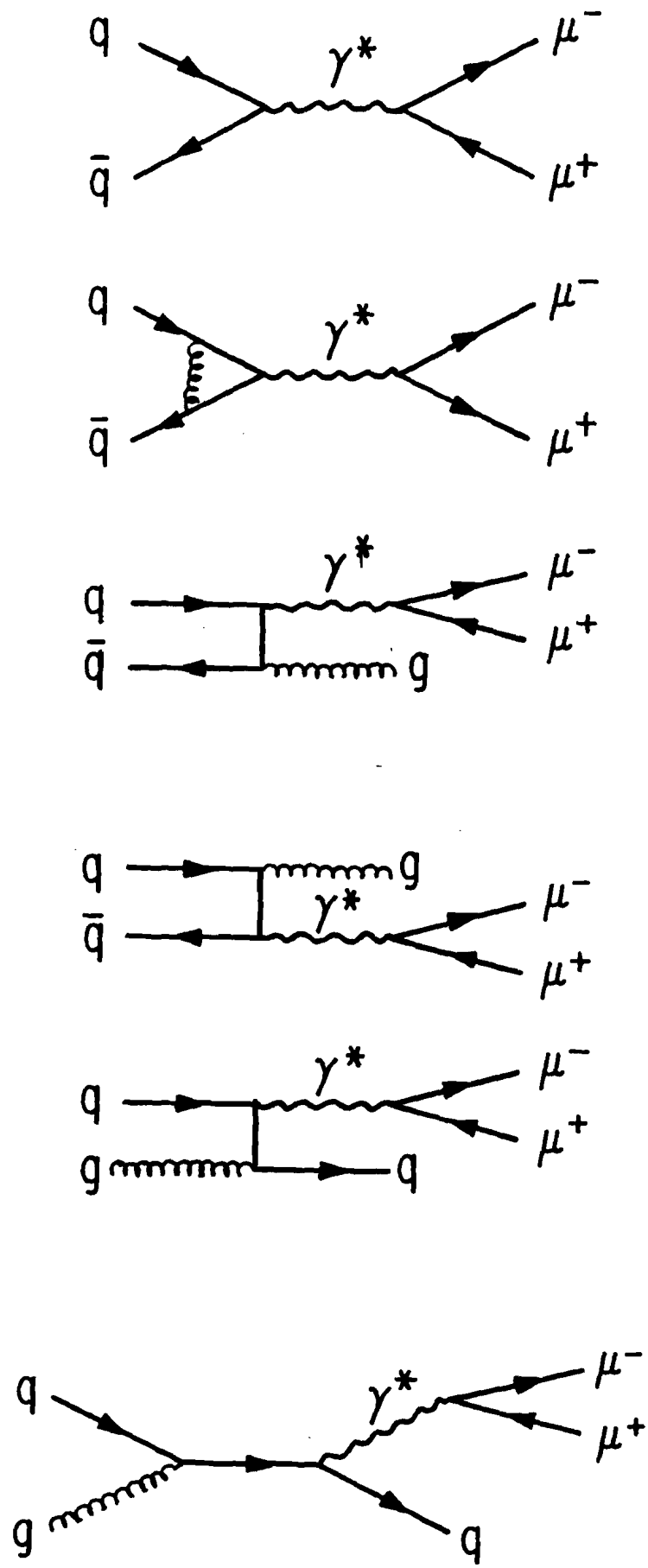
q
$\bar{q}$
γ^*
μ^-
μ^+
q
$\bar{q}$
γ^*
μ^-
μ^+
q
$\bar{q}$
γ^*
g
μ^-
μ^+
q
$\bar{q}$
g
γ^*
μ^-
μ^+
q
g
γ^*
q
μ^-
μ^+
q
g
γ^*
q
μ^-
μ^+

Figure 3.--An example of an active quark-spectator quark correction to the simple Drell-Yan model.

Fig. 3

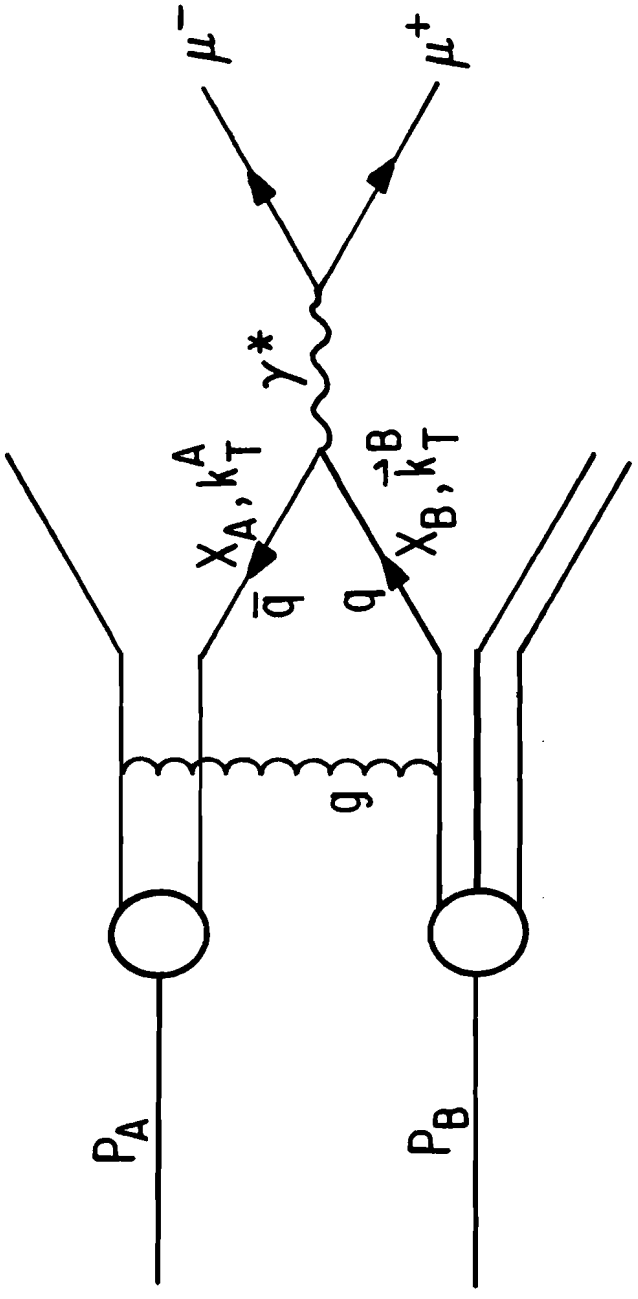

Figure 4.--A plan view of the E326 spectrometer. An end view (as seen by the beam) is shown in Section A-A'.

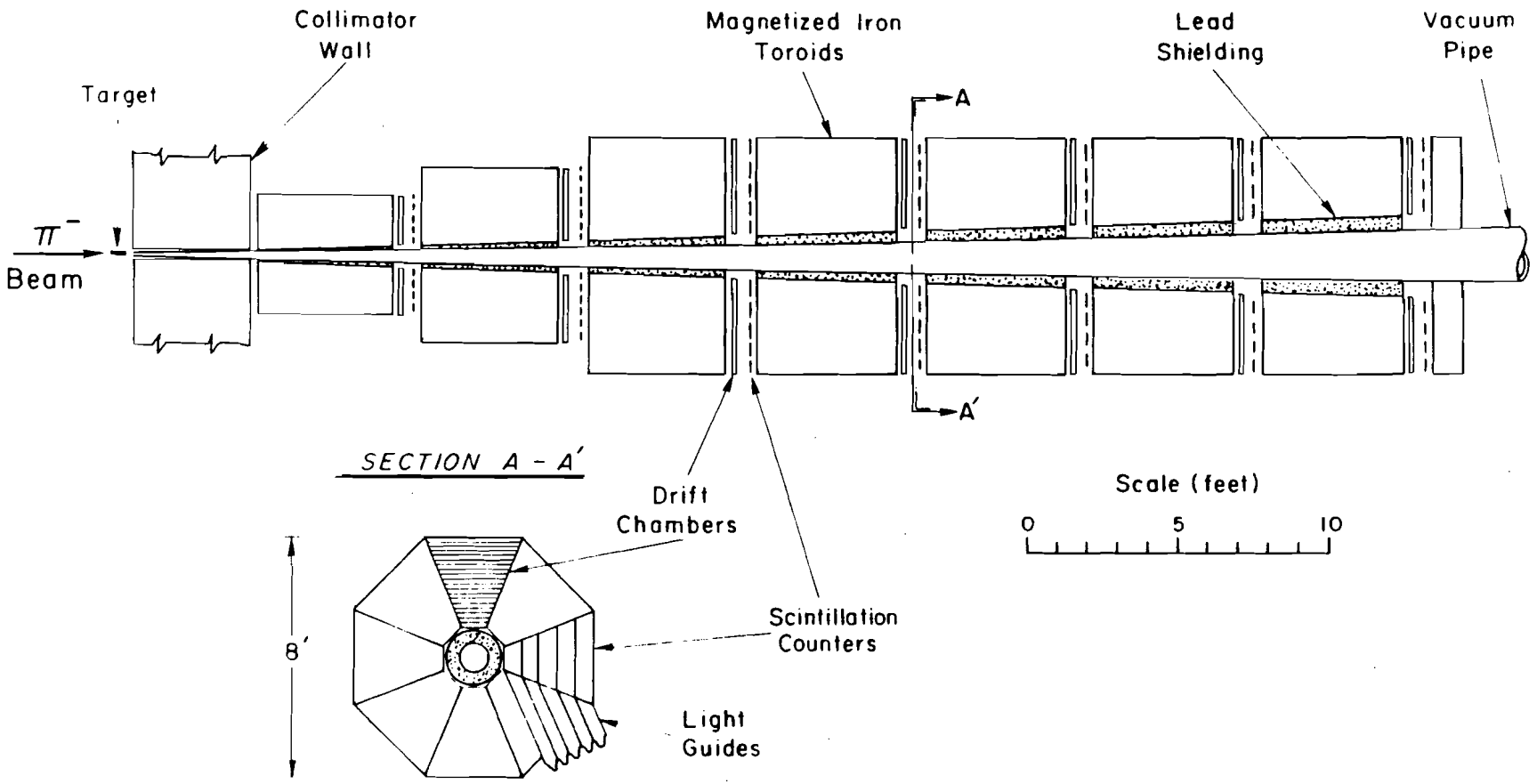
Collimator Wall
Magnetized Iron Toroids
Lead Shielding
Vacuum Pipe
Target
A
A'
π⁻ Beam
SECTION A - A'
Drift Chambers
Scintillation Counters
Light Guides
8'
Scale (feet)
0
5
10

Fig. 4

Figure 5.--Plan view of the P-West High Intensity Beam.

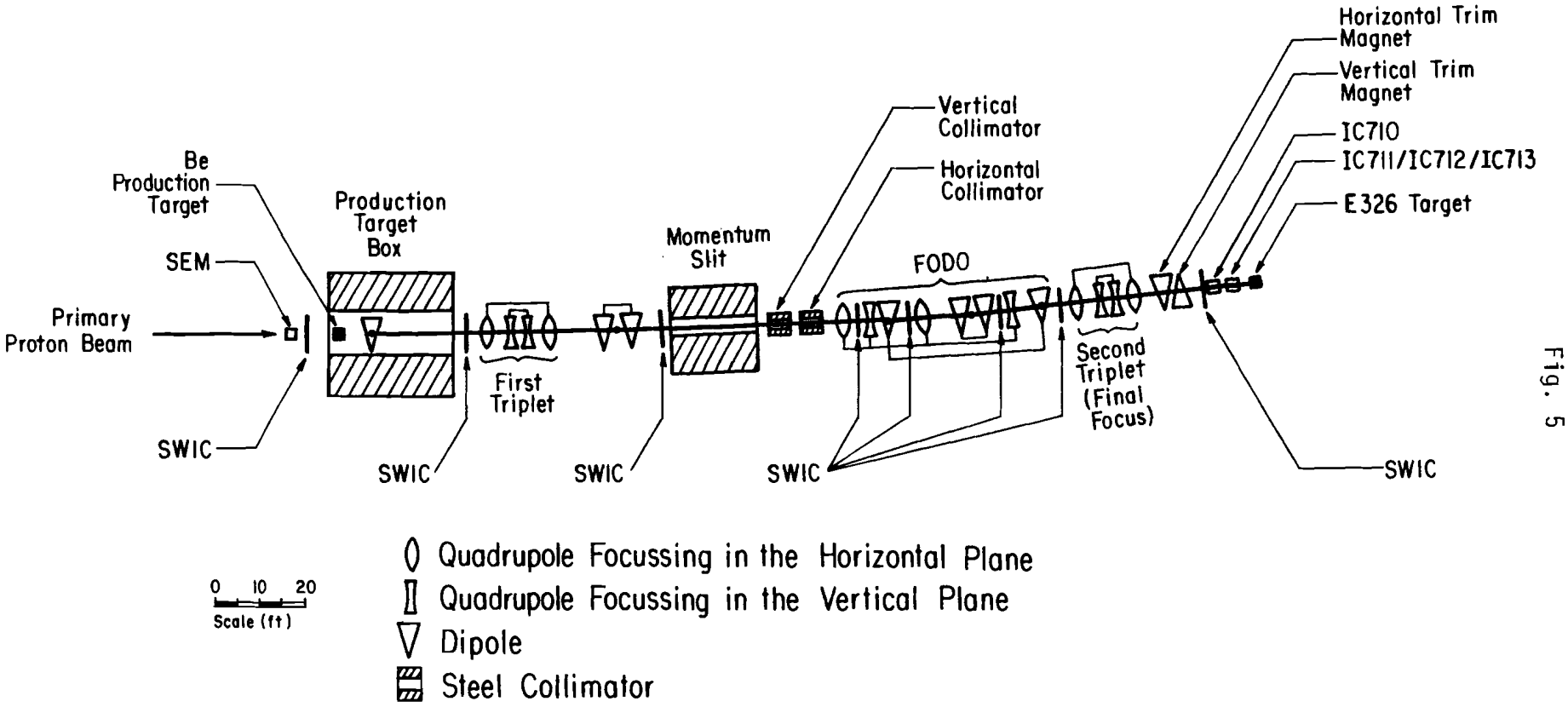
Be
Production
Target
SEM
Primary
Proton Beam
SWIC
Production
Target
Box
First
Triplet
SWIC
Momentum
Slit
SWIC
Vertical
Collimator
Horizontal
Collimator
SWIC
FODO
Second
Triplet
(Final
Focus)
Horizontal Trim
Magnet
Vertical Trim
Magnet
IC710
IC711/IC712/IC713
E326 Target
SWIC
0 10 20
Scale (ft)
Quadrupole Focussing in the Horizontal Plane
Quadrupole Focussing in the Vertical Plane
Dipole
Steel Collimator

Fig. 5

Figure 6.--P-West beam momentum distribution for the E326 225 GeV/c beam tube.

Fig. 6

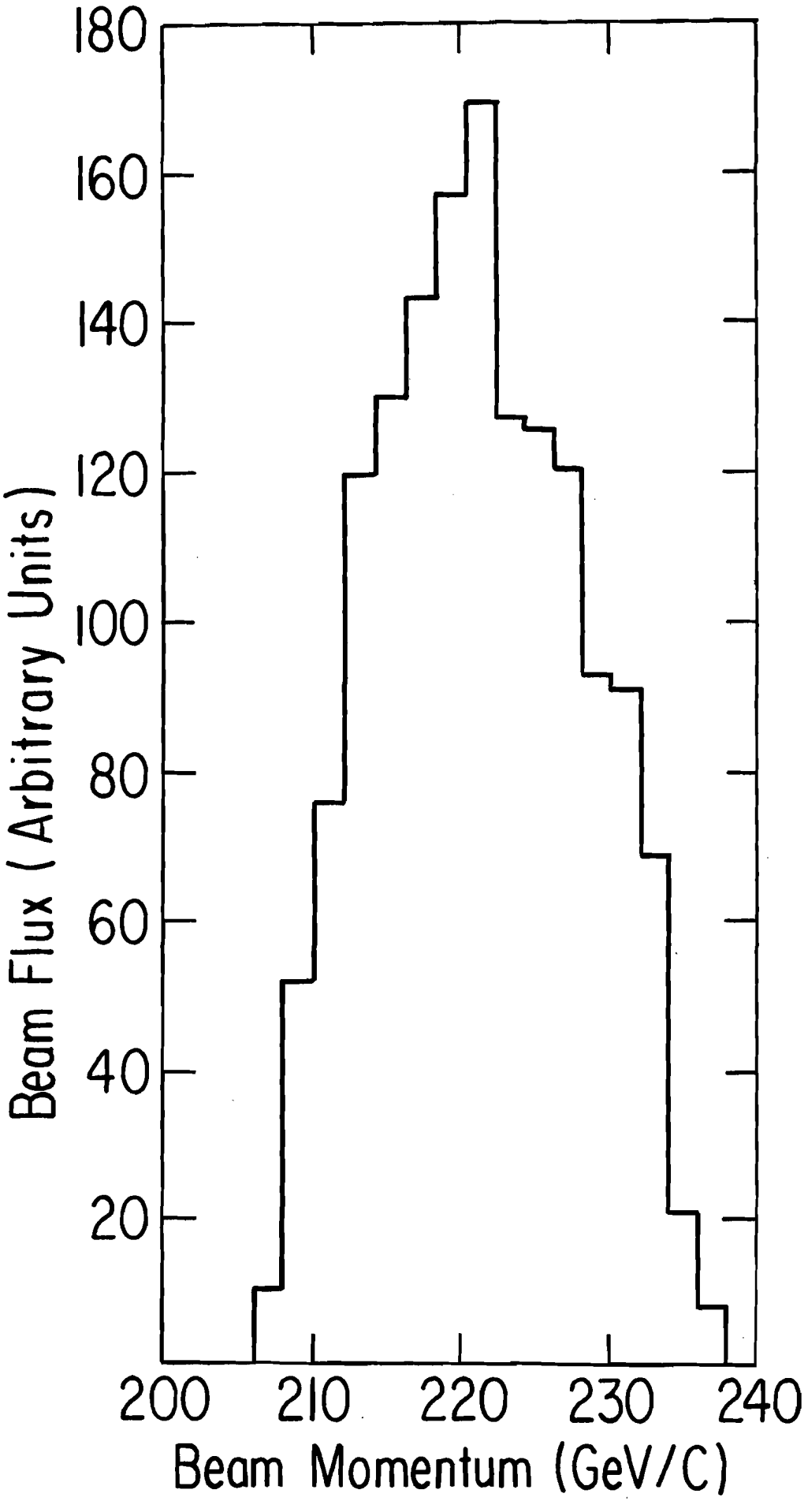
180
160
140
120
100
80
60
40
20
Beam Flux (Arbitrary Units)
200
210
220
230
240
Beam Momentum (GeV/C)

Figure 7.--Plane 3 trigger hodoscope (see section A-A' in Figure 4) illustrating the arrangement of counters and the numbering scheme.

Fig. 7

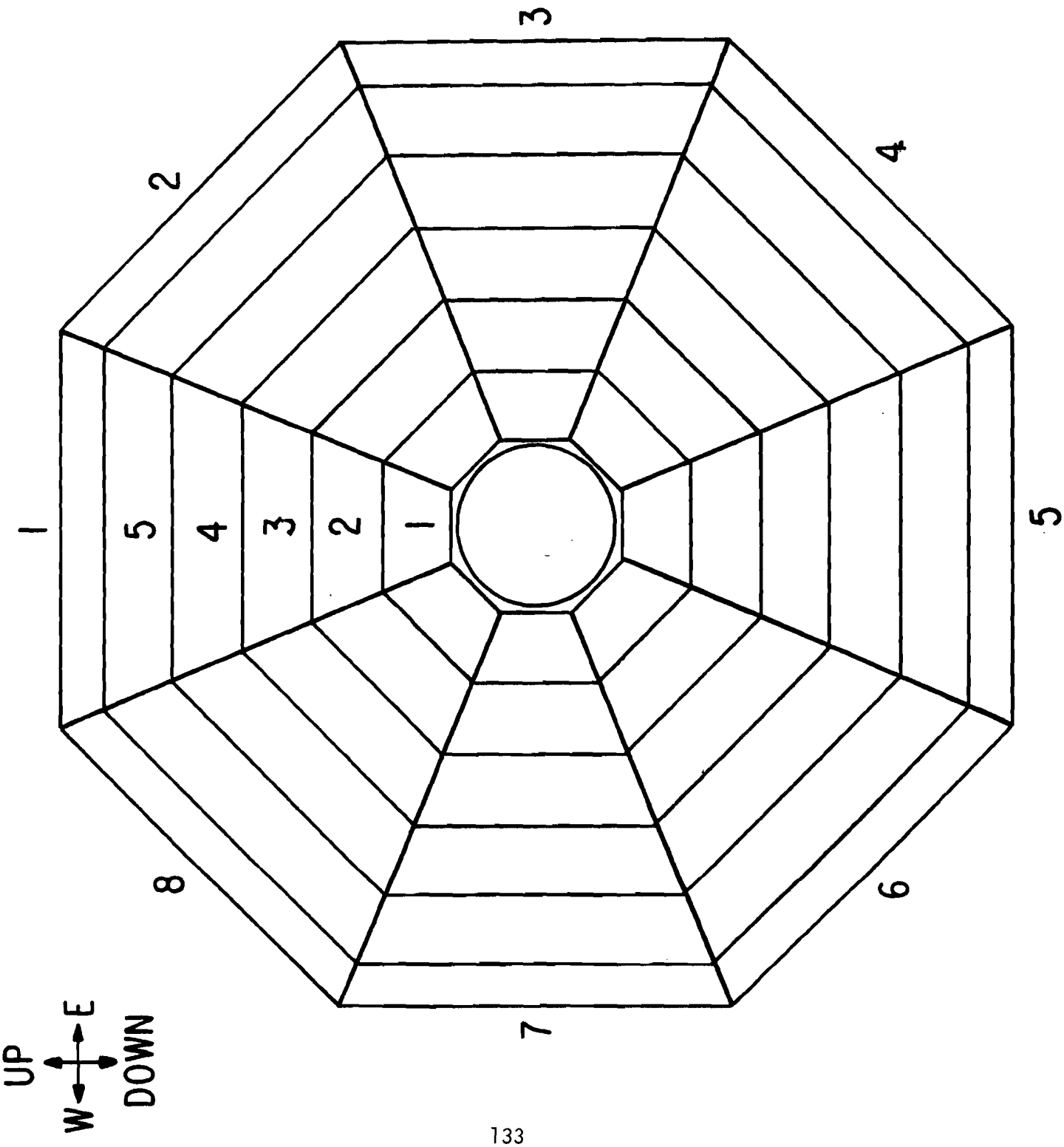

Figure 8.--Plan view of the veto hodoscopes.

Fig. 8

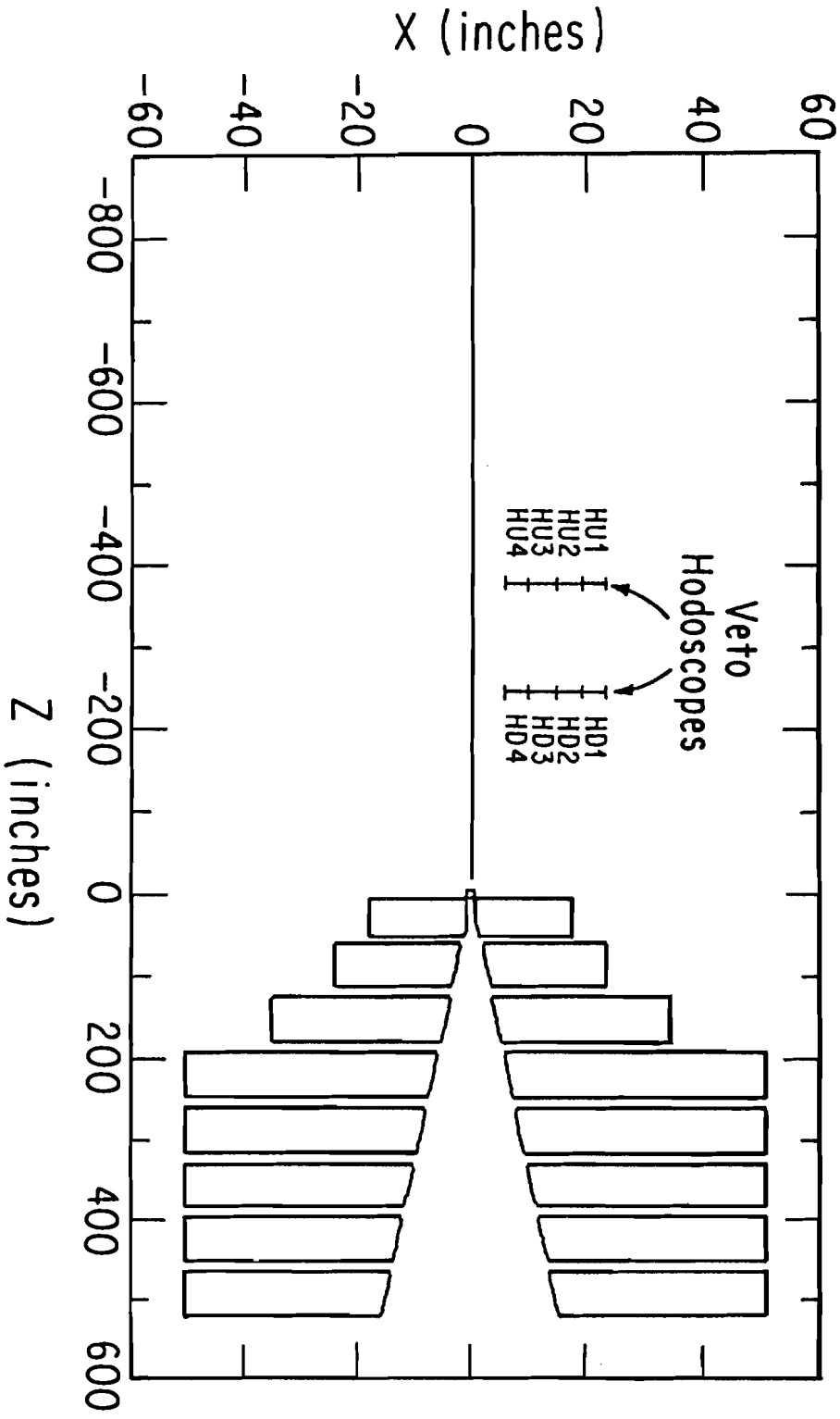
X (inches)
-60
-40
-20
0
20
40
60
Z (inches)
-800
-600
-400
-200
0
200
400
600
HU1
HU2
HU3
HU4
HD1
HD2
HD3
HD4
Veto
Hodoscopes

Figure 9.--An event picture of a typical opposite sign dimuon.

Fig. 9

RUN 959, EVENT 5325

OCTANT 2 OCTANT 6

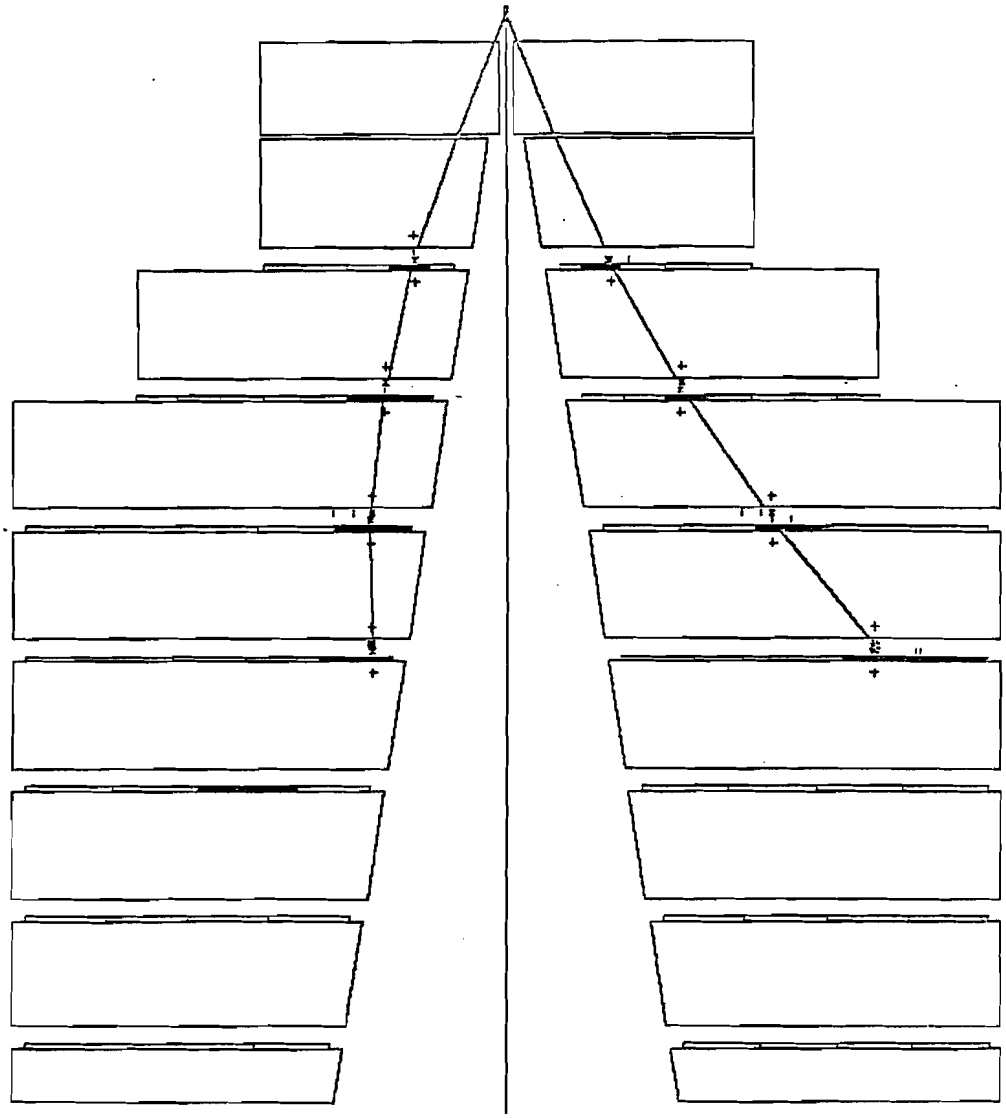

Figure 10.--An event picture of an accidental trigger caused by two "halo" muons.

Fig. 10

RUN 959, EVENT 715

OCTANT 6 OCTANT 8

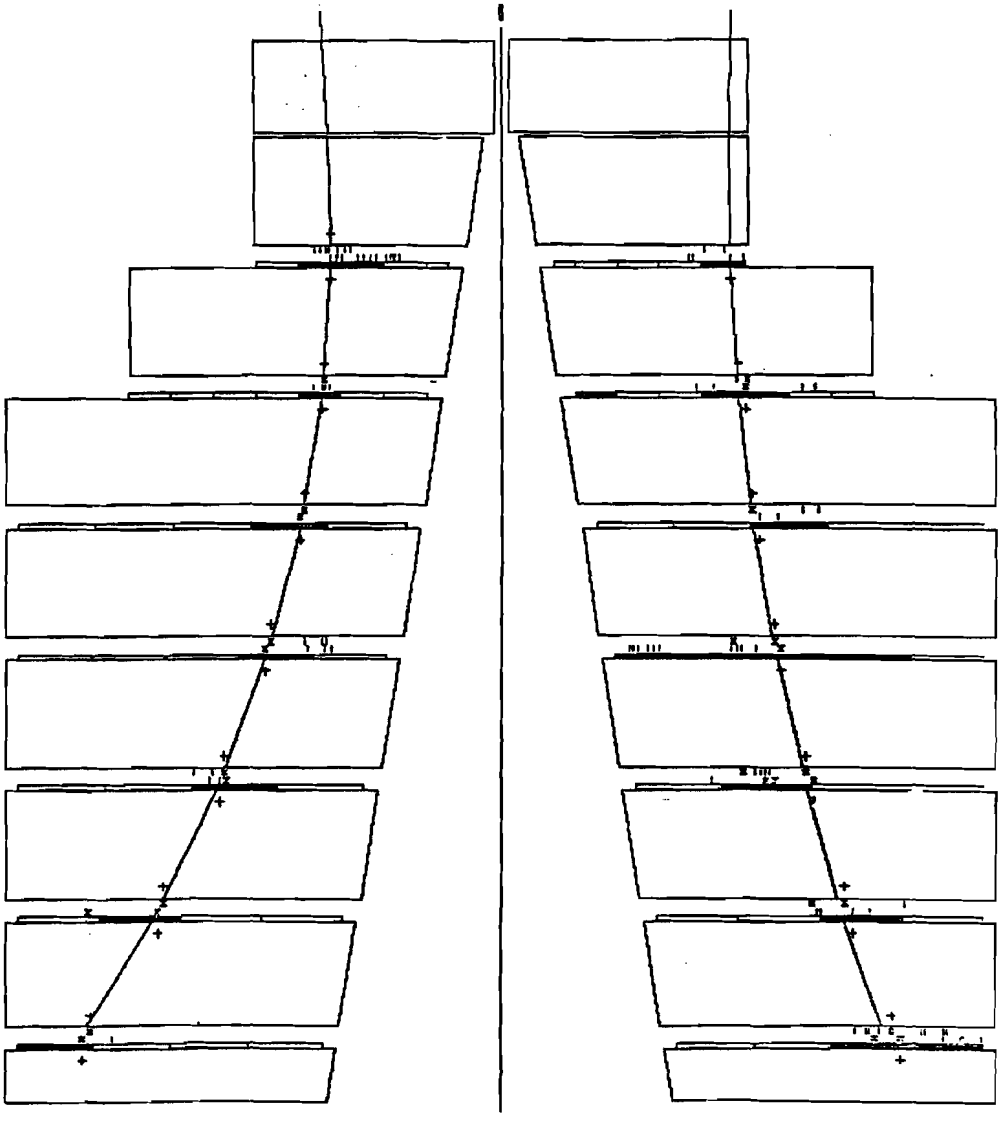

Figure 11.--Block diagram of the trigger.

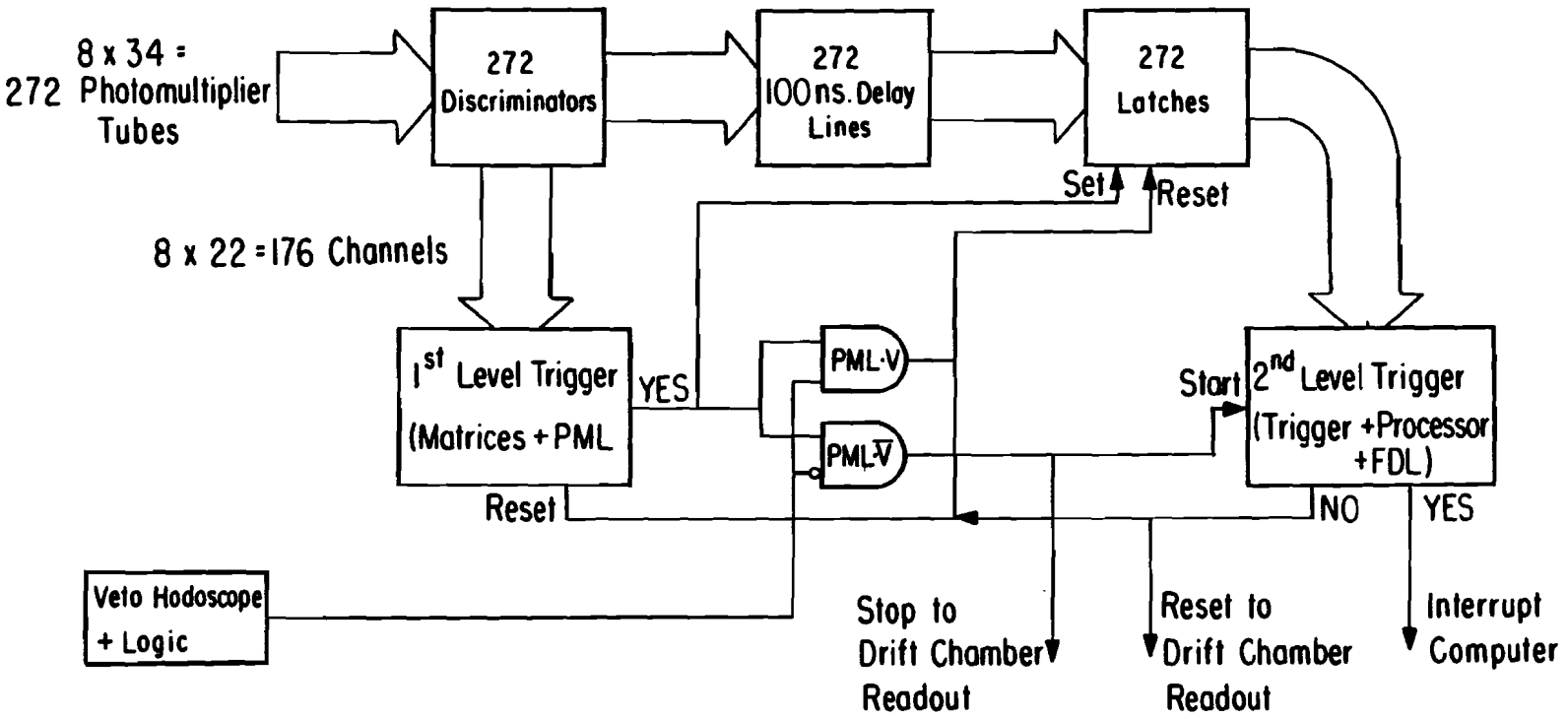
8 x 34 =
272 Photomultiplier
Tubes
272
Discriminators
272
100 ns. Delay
Lines
272
Latches
Set
Reset
8 x 22 = 176 Channels
1st Level Trigger
(Matrices + PML
YES
PML·V
PML·V̄
Start
2nd Level Trigger
(Trigger + Processor
+ FDL)
Reset
NO
YES
Veto Hodoscope
+ Logic
Stop to
Drift Chamber
Readout
Reset to
Drift Chamber
Readout
Interrupt
Computer

Fig. 11

Figure 12.--The front end trigger logic and matrices for one octant. The labels Pn Cm refer to the m^{th} scintillation counter of the n^{th} hodoscope plane. The labels MPX and DISC refer to a multiplexor (used to monitor the scintillation counters) and a discriminator.

Fig. 12

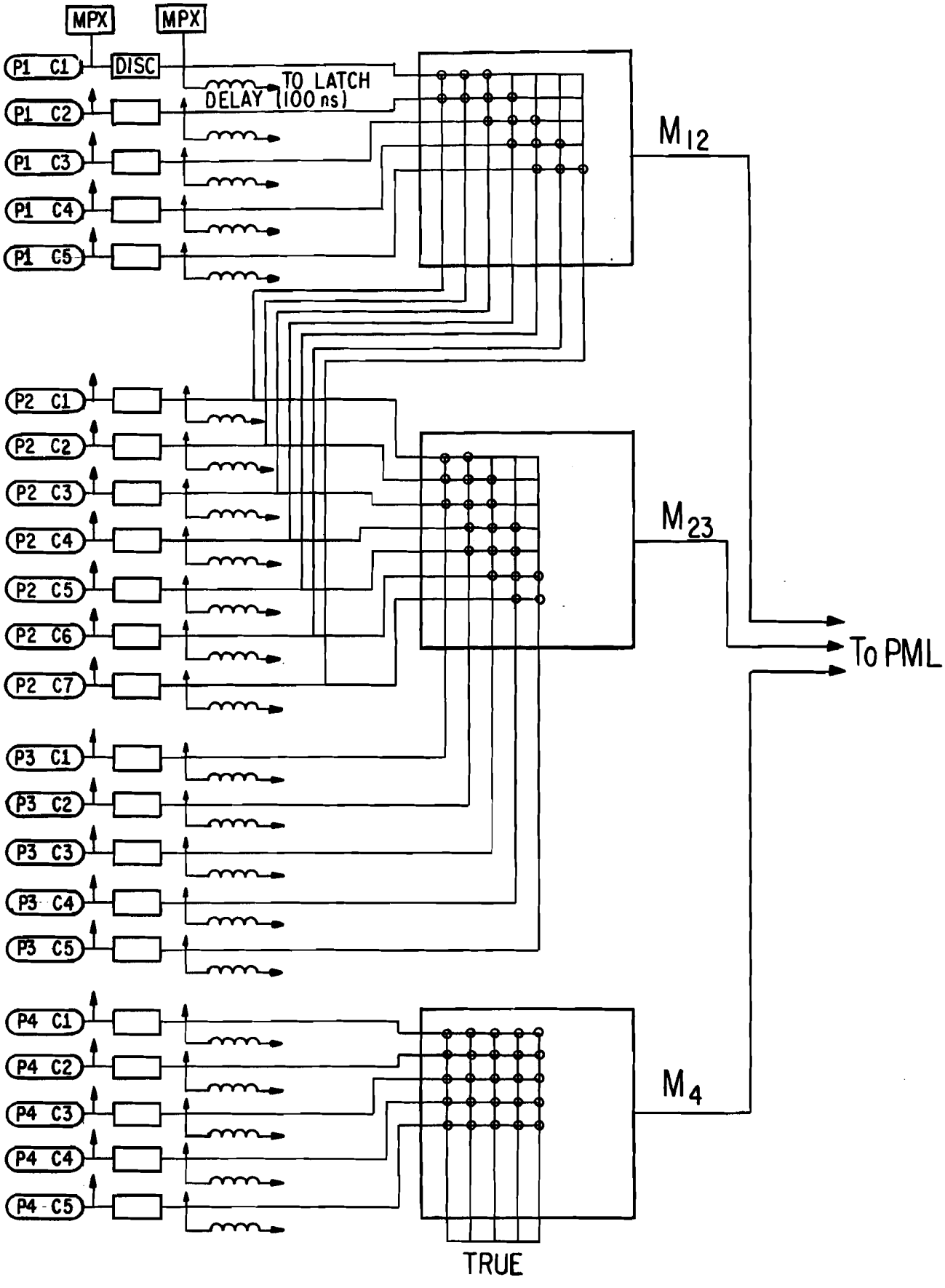
MPX
MPX
P1 C1
DISC
TO LATCH
DELAY (100 ns)
P1 C2
P1 C3
P1 C4
P1 C5
M12
P2 C1
P2 C2
P2 C3
P2 C4
P2 C5
P2 C6
P2 C7
M23
To PML
P3 C1
P3 C2
P3 C3
P3 C4
P3 C5
P4 C1
P4 C2
P4 C3
P4 C4
P4 C5
M4
TRUE

Figure 13.--A schematic diagram of the post matrix logic (PML). The label OCTn MIJ refers to the input from matrix MIJ (IJ = 12, 23, 4) in octant n.

Fig. 13

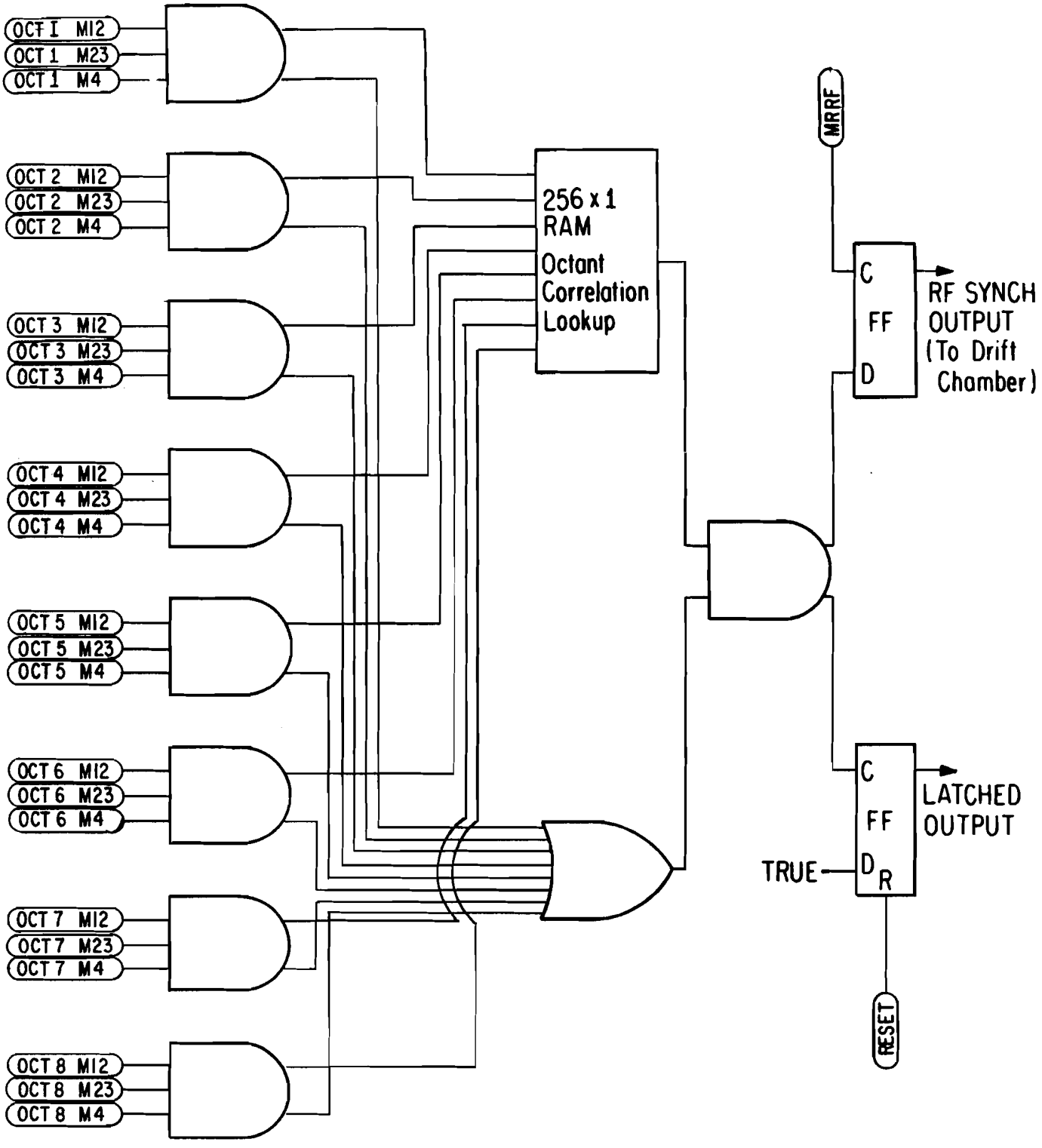
OCT 1 M12
OCT 1 M23
OCT 1 M4
OCT 2 M12
OCT 2 M23
OCT 2 M4
OCT 3 M12
OCT 3 M23
OCT 3 M4
OCT 4 M12
OCT 4 M23
OCT 4 M4
OCT 5 M12
OCT 5 M23
OCT 5 M4
OCT 6 M12
OCT 6 M23
OCT 6 M4
OCT 7 M12
OCT 7 M23
OCT 7 M4
OCT 8 M12
OCT 8 M23
OCT 8 M4
256 x 1 RAM
Octant Correlation Lookup
MRRF
C
FF
D
RF SYNCH OUTPUT (To Drift Chamber)
C
FF
D
R
LATCHED OUTPUT
TRUE
RESET

Figure 14.--Logic diagram for the veto hodoscope counters.

Fig. 14

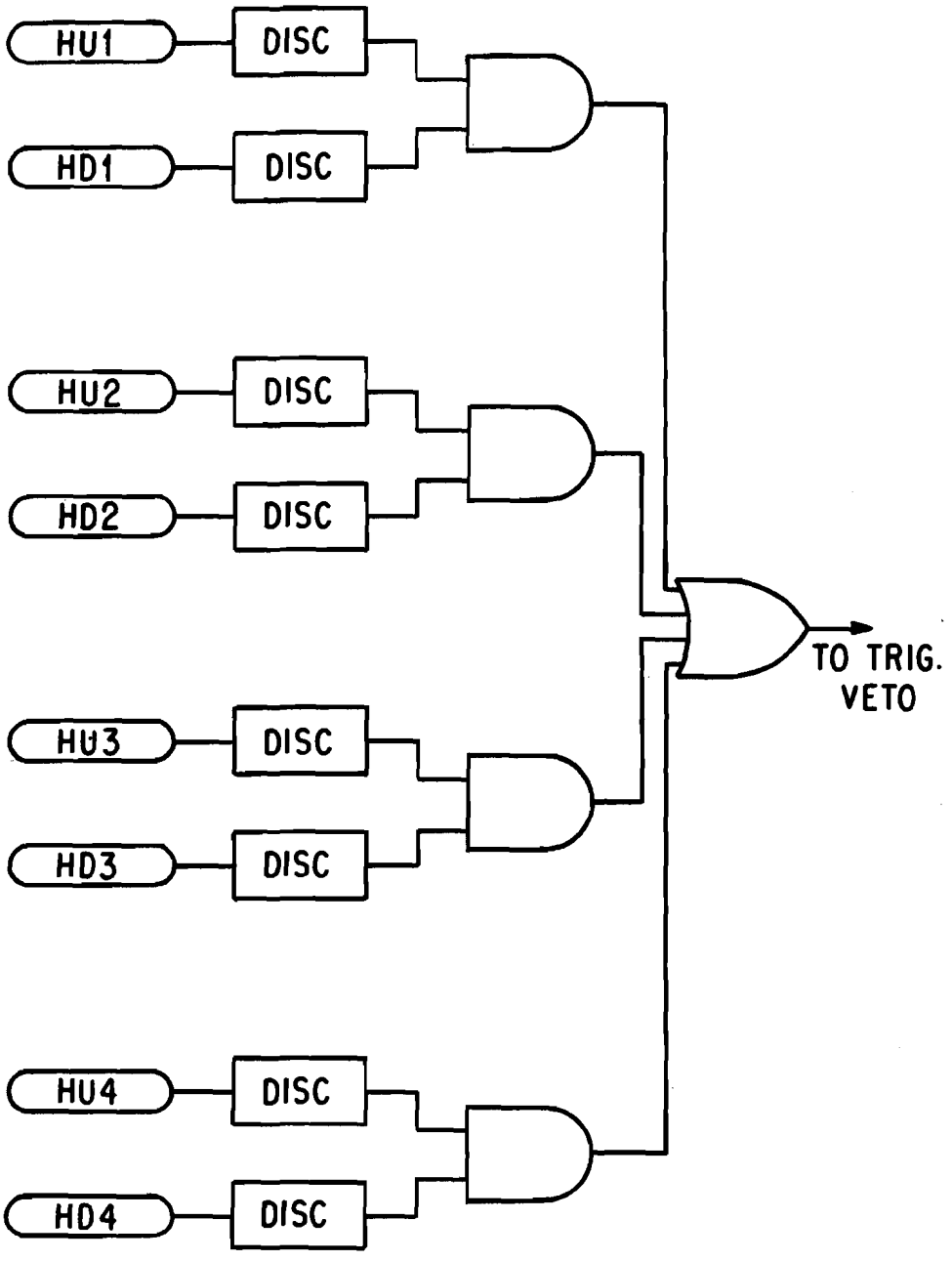
HU1
DISC
HD1
DISC
HU2
DISC
HD2
DISC
HU3
DISC
HD3
DISC
HU4
DISC
HD4
DISC
TO TRIG.
VETO

Figure 15.--Schematic diagram of the second level trigger.

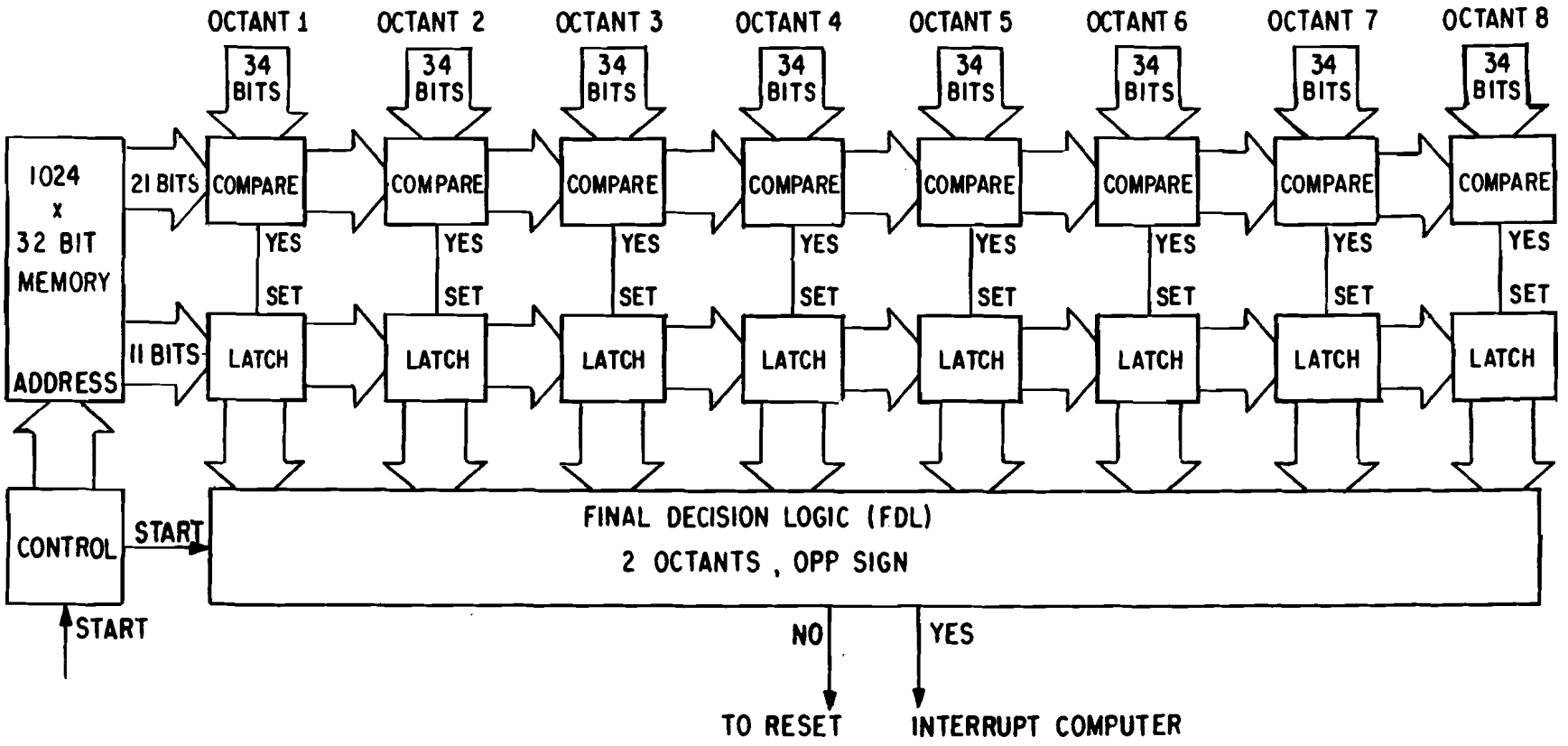
OCTANT 1
OCTANT 2
OCTANT 3
OCTANT 4
OCTANT 5
OCTANT 6
OCTANT 7
OCTANT 8
34 BITS
1024 x 32 BIT MEMORY
ADDRESS
21 BITS
11 BITS
COMPARE
YES SET
LATCH
CONTROL
START
START
FINAL DECISION LOGIC (FDL)
2 OCTANTS , OPP SIGN
NO
YES
TO RESET
INTERRUPT COMPUTER

Fig. 15

Figure 16.--A side view of several drift cells illustrating the I beam cathode construction.

Fig. 16

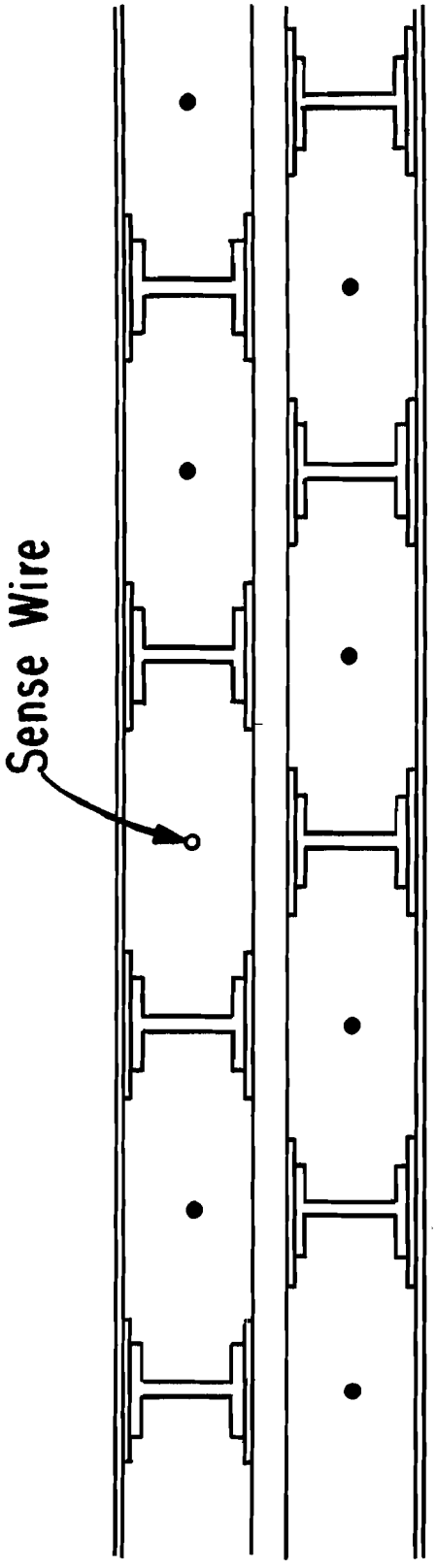

Figure 17.--A block diagram of the drift chamber electronics.

Fig. 17

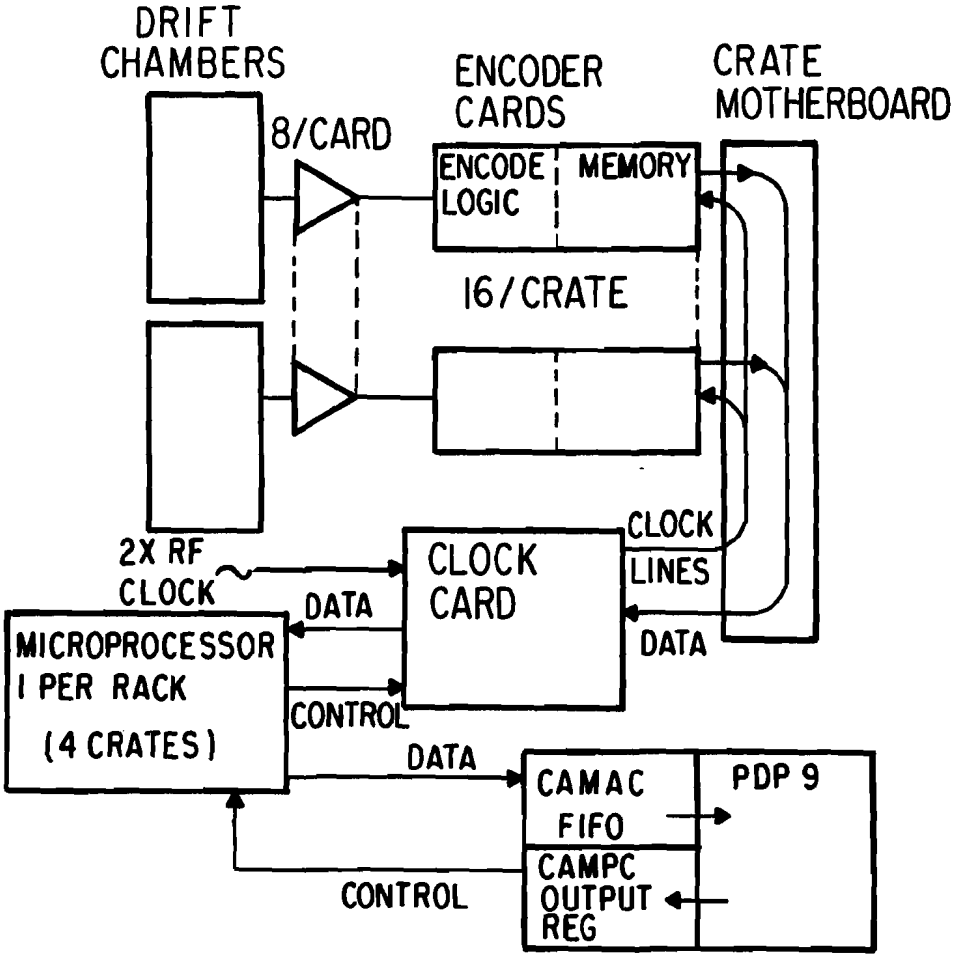

BLOCK DIAGRAM

Figure 18.--A drift chamber amplifier/discriminator channel.

Fig. 18

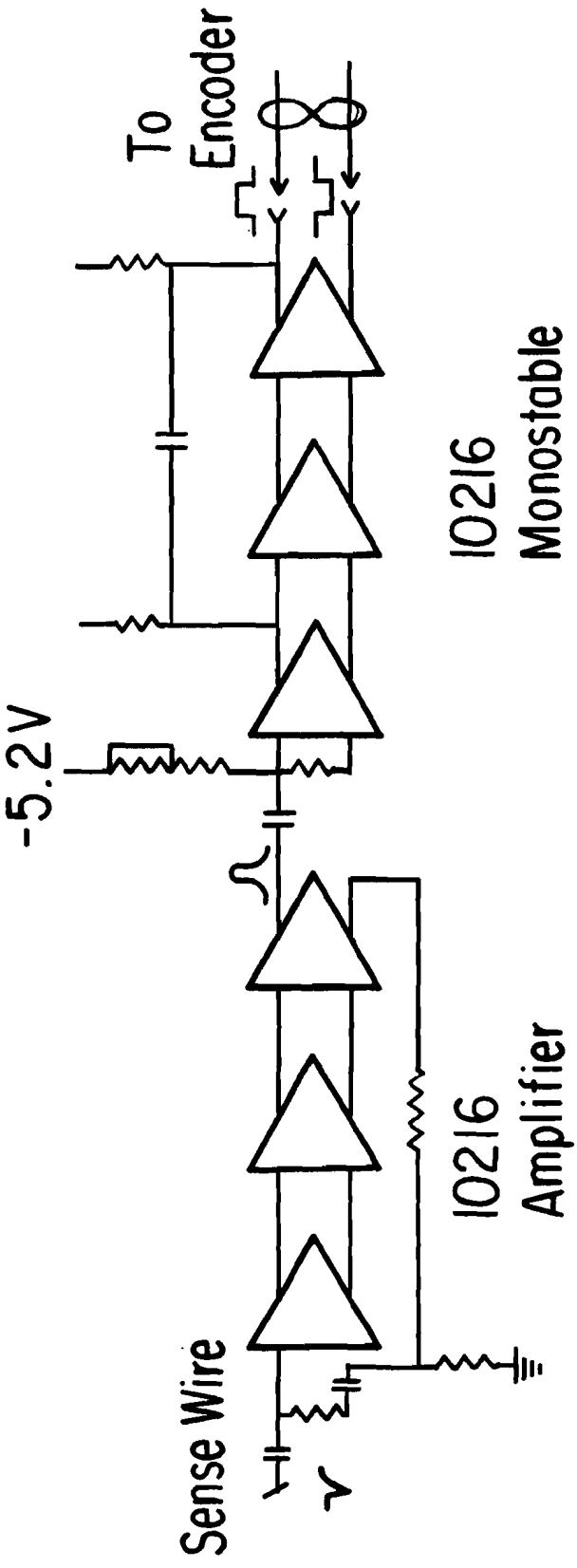
To Encoder
10216 Monostable
-5.2V
10216 Amplifier
Sense Wire

Figure 19.--Drift chamber time encoding logic. Represented is one of eight channels on each encoder card.

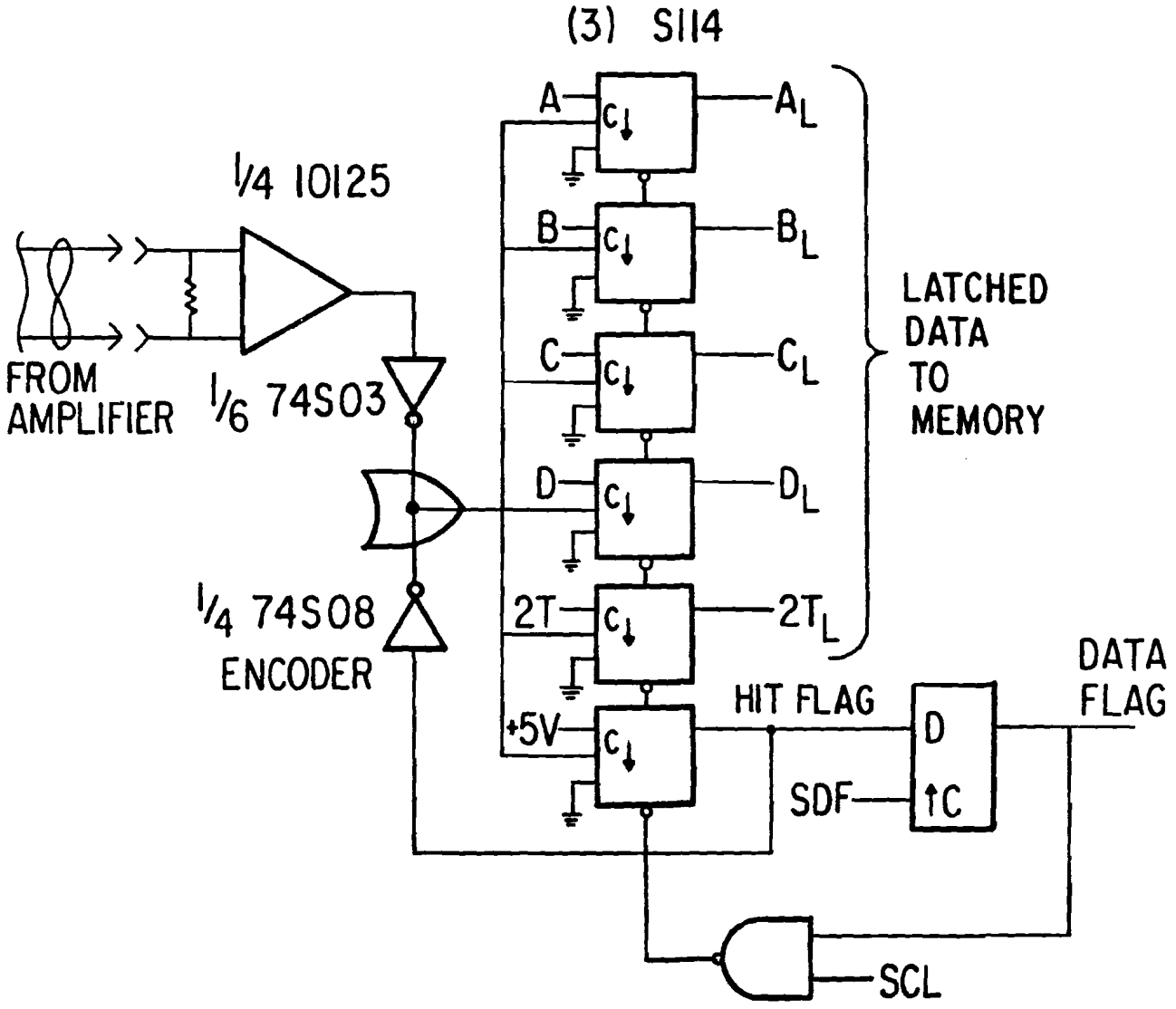
(3) S114
1/4 10125
FROM AMPLIFIER
1/6 74S03
1/4 74S08 ENCODER
A
B
C
D
2T
+5V
A_L
B_L
C_L
D_L
$2T_L$
LATCHED DATA TO MEMORY
HIT FLAG
SDF
D
↑C
DATA FLAG
SCL

Fig. 19

Figure 20.--The timing diagram for the encoder system timing signals. The four signals labeled A through D are phased to divide each 74.4 nanosecond memory cycle (defined by MA0) into eight 9.3 nanosecond bins.

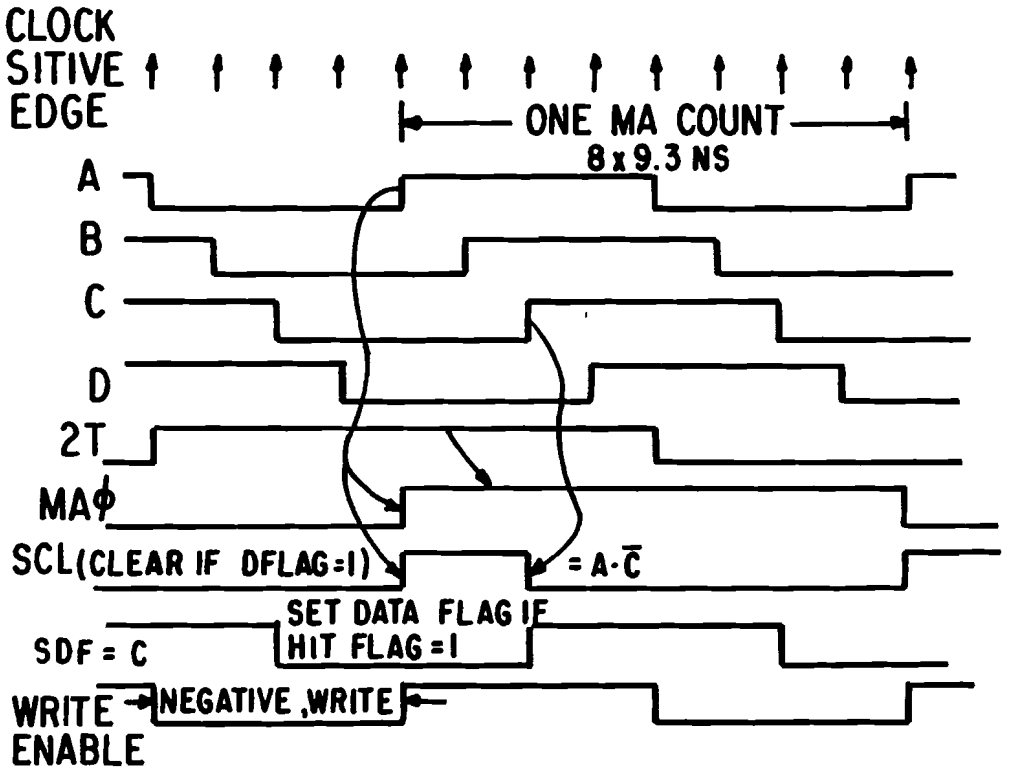
CLOCK
SITIVE
EDGE
ONE MA COUNT
8 x 9.3 NS
A
B
C
D
2T
MAϕ
SCL(CLEAR IF DFLAG=1)
= A·C̄
SET DATA FLAG IF
HIT FLAG=1
SDF = C
WRITE
ENABLE
NEGATIVE ,WRITE

Fig. 20

Figure 21.--A block diagram of the data acquisition system. The arrows indicate the direction of data flow. The inter-CAMAC crate connections are bidirectional.

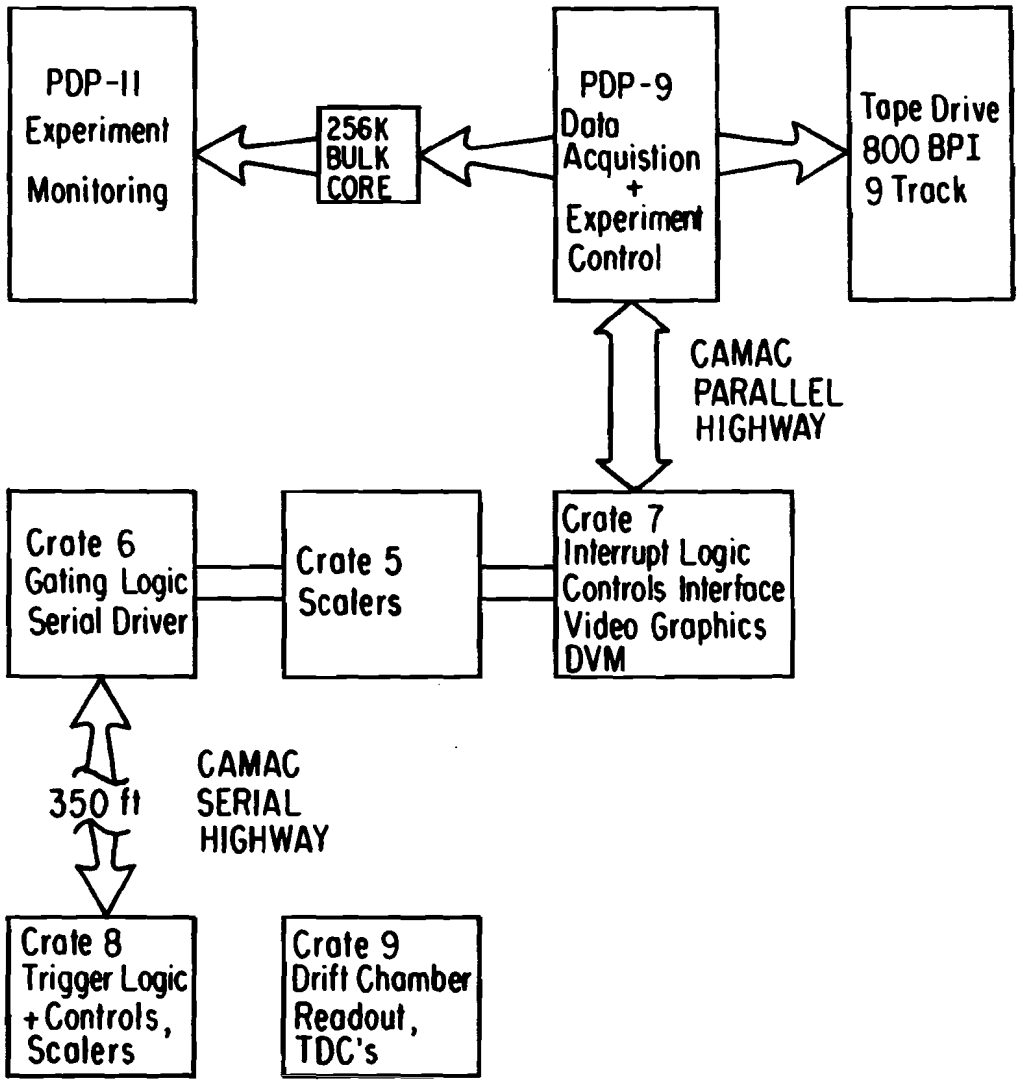
PDP-11
Experiment
Monitoring
256K
BULK
CORE
PDP-9
Data
Acquistion
+
Experiment
Control
Tape Drive
800 BPI
9 Track
CAMAC
PARALLEL
HIGHWAY
Crate 6
Gating Logic
Serial Driver
Crate 5
Scalers
Crate 7
Interrupt Logic
Controls Interface
Video Graphics
DVM
350 ft
CAMAC
SERIAL
HIGHWAY
Crate 8
Trigger Logic
+Controls,
Scalers
Crate 9
Drift Chamber
Readout,
TDC's

Fig. 21

Figure 22.--Radial Chi-Squared distribution for all tracks after the topology cut.

Fig. 22

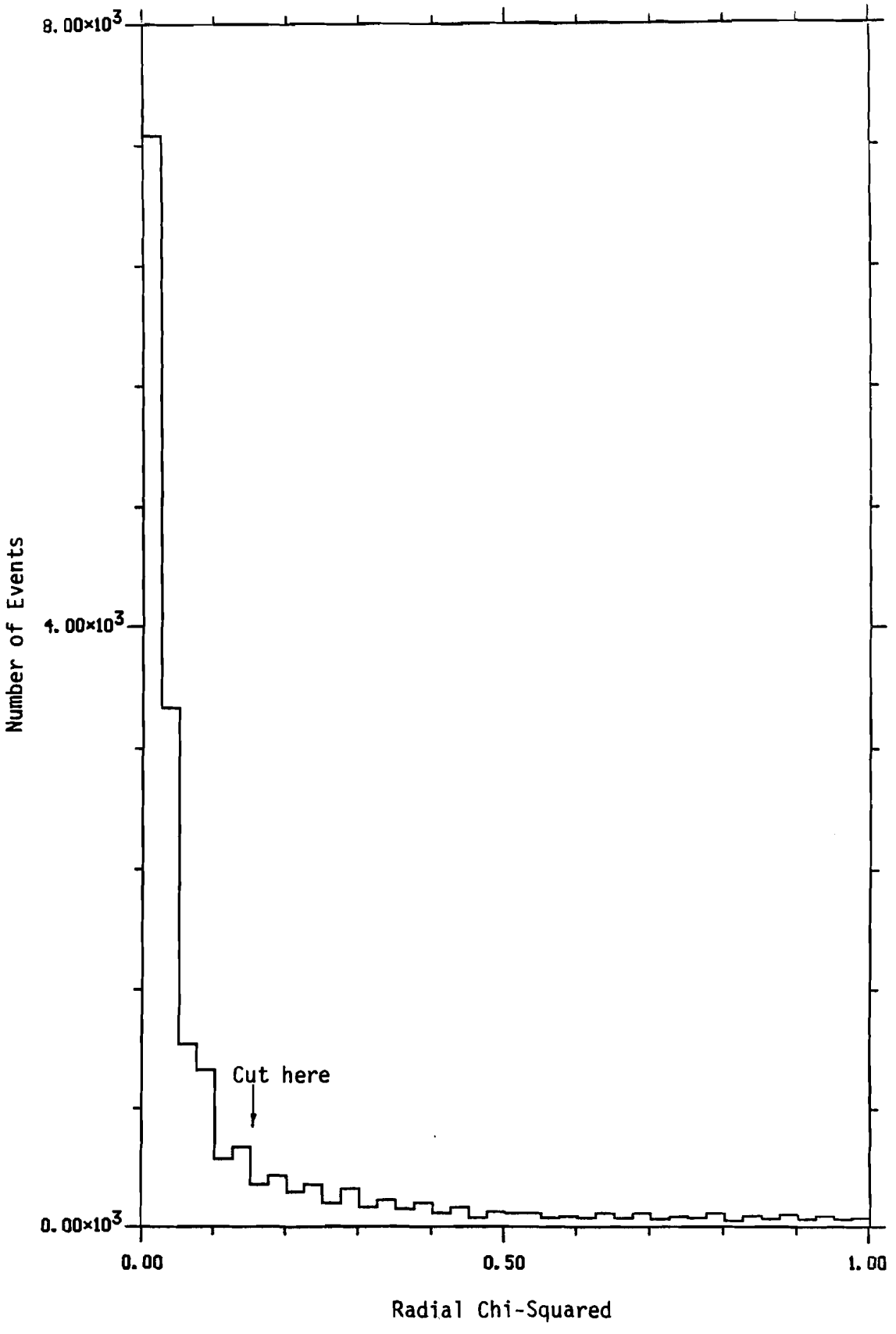
8.00×10^3
4.00×10^3
0.00×10^3
Number of Events
Cut here
0.00
0.50
1.00
Radial Chi-Squared

Figure 23.--Transverse Chi-Squared for all tracks after the topology cut.

Fig. 23

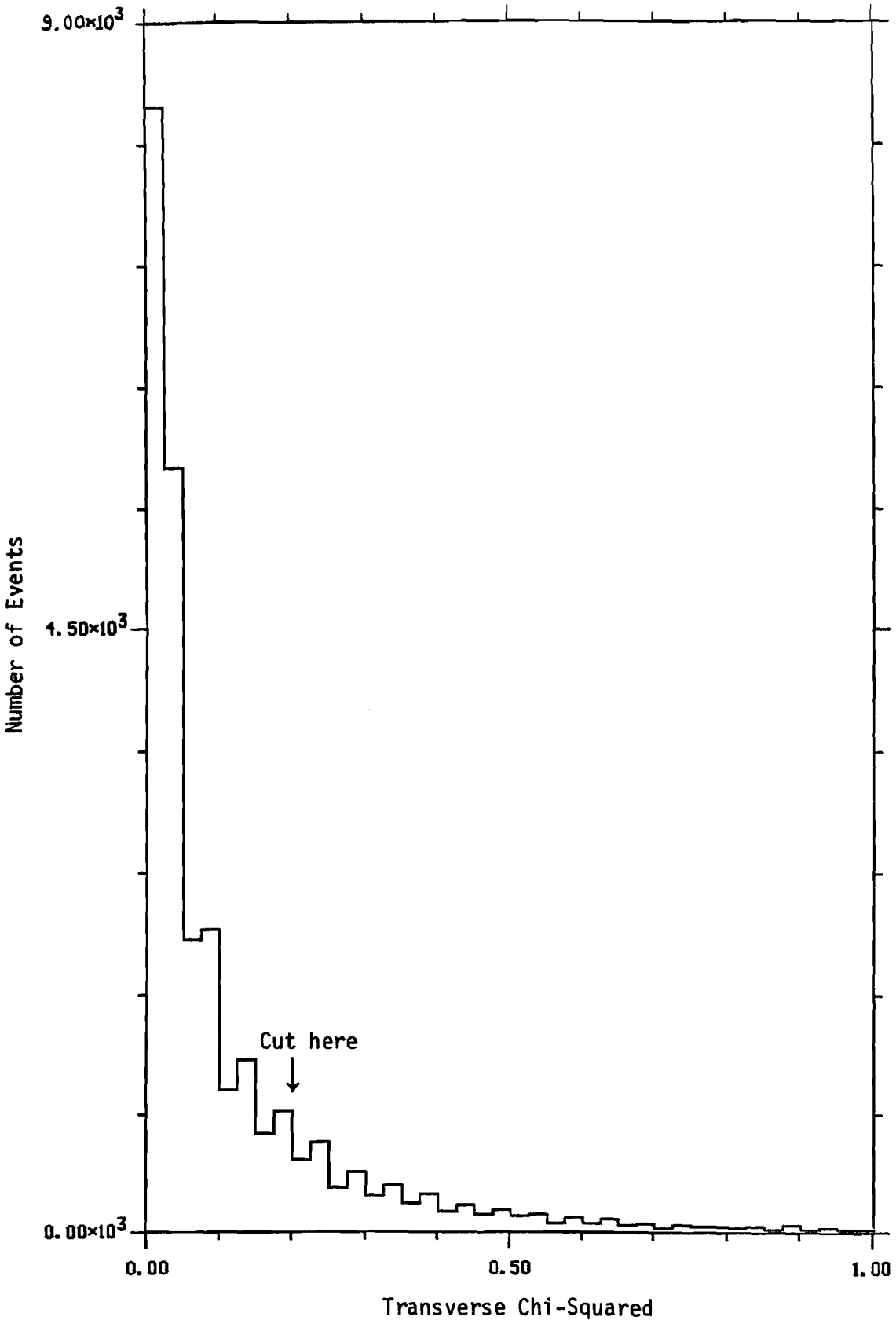
9.00×10^3
4.50×10^3
0.00×10^3
Number of Events
Cut here
0.00
0.50
1.00
Transverse Chi-Squared

Figure 24.--Target Radius for positive tracks satisfying the χ^2 cuts.

Fig. 24

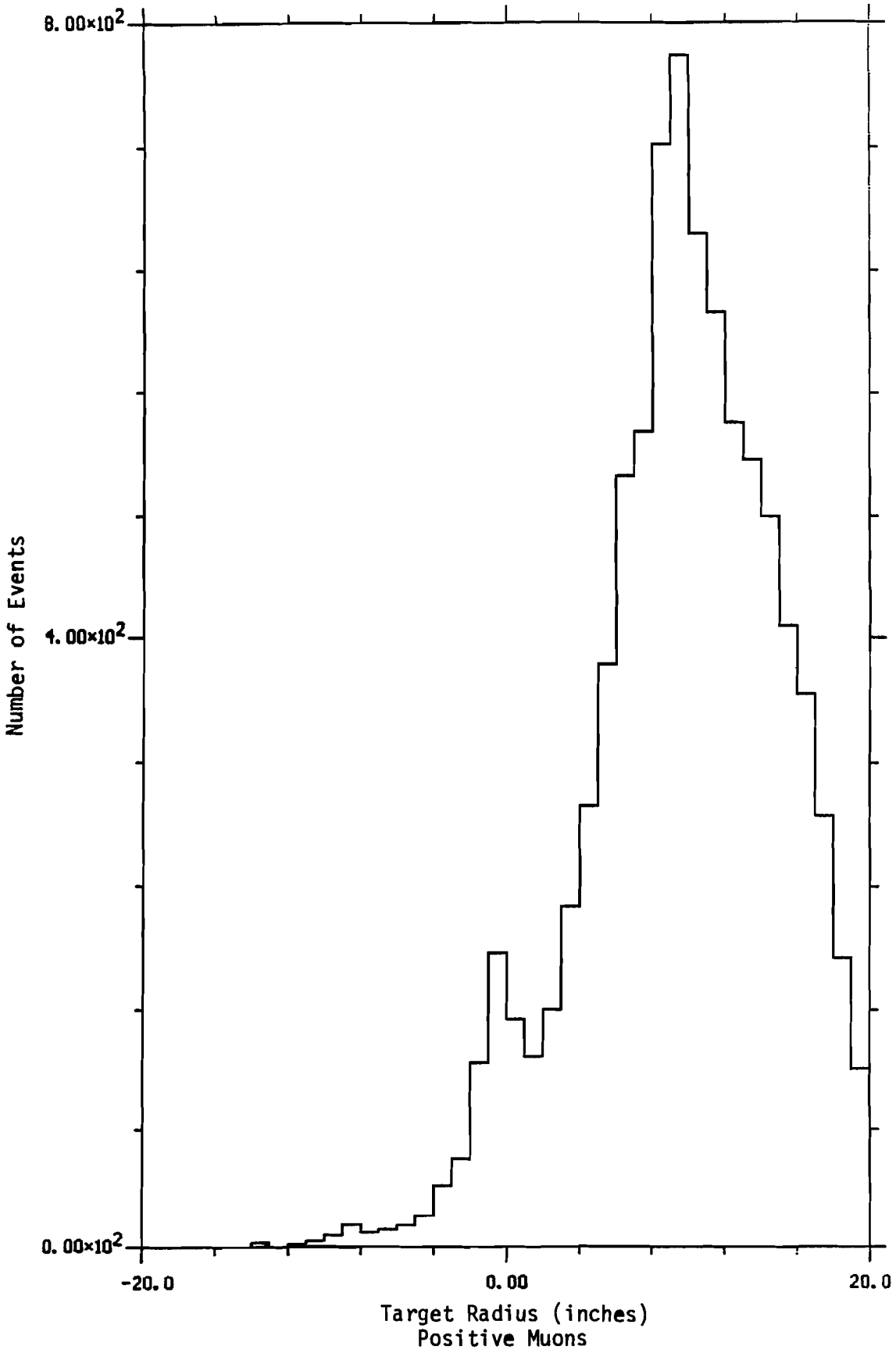
8.00×10²
4.00×10²
0.00×10²
Number of Events
-20.0
0.00
20.0
Target Radius (inches)
Positive Muons

Figure 25.--Target Radius for negative tracks satisfying the χ^2 cuts.

Fig. 25

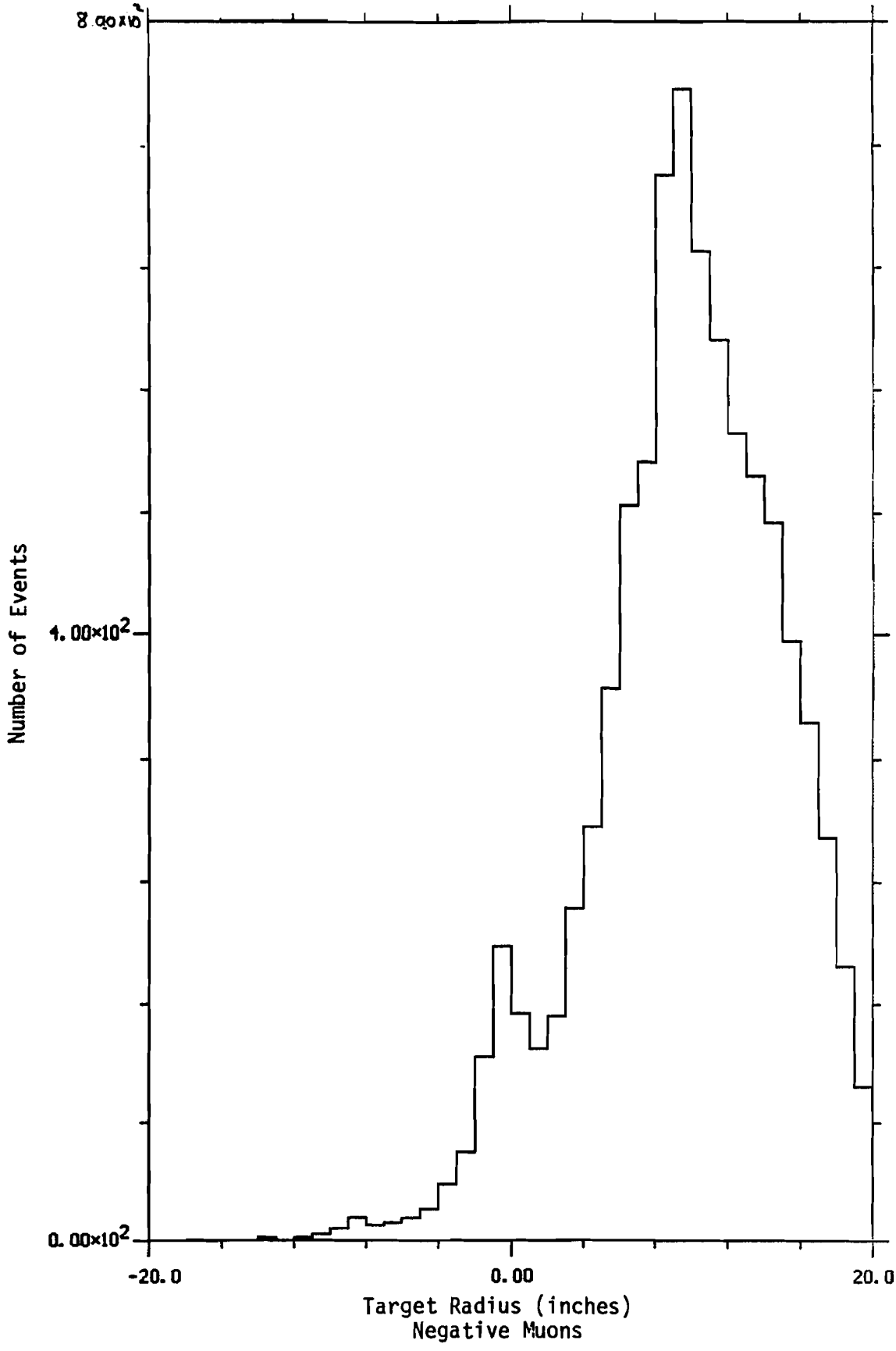
8.00x10²
4.00×10²
0.00×10²
Number of Events
-20.0
0.00
20.0
Target Radius (inches)
Negative Muons

Figure 26.--Track angle distribution for all positive tracks satisfying the χ^2 cuts.

Fig. 26

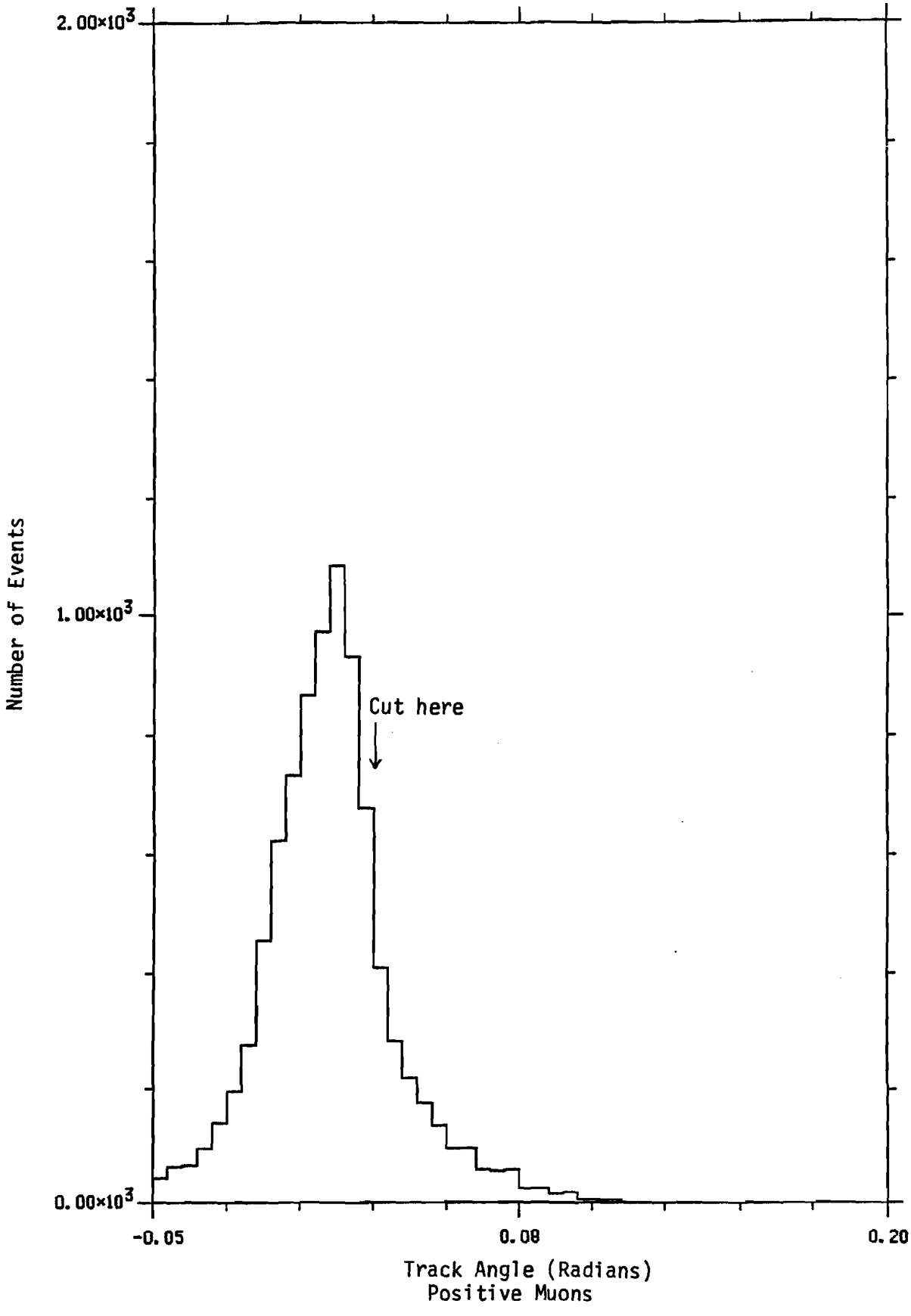
2.00×10³
1.00×10³
0.00×10³
Number of Events
Cut here
-0.05
0.08
0.20
Track Angle (Radians)
Positive Muons

Figure 27.--Track angle distribution for all negative tracks satisfying the χ^2 cuts.

Fig. 27

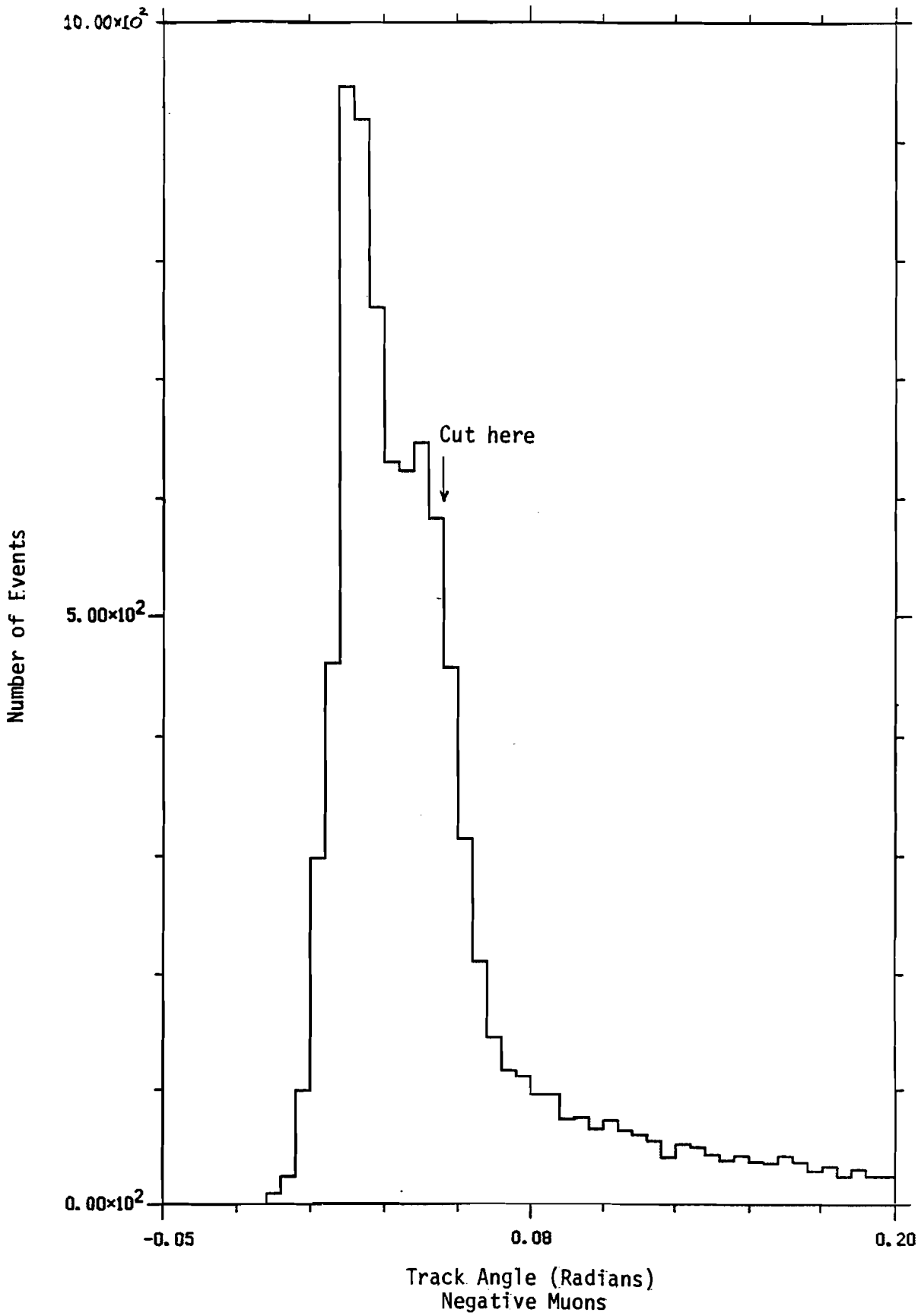
10.00×10²
5.00×10²
0.00×10²
Number of Events
Cut here
-0.05
0.08
0.20
Track Angle (Radians)
Negative Muons

Figure 28.--A Monte Carlo calculation of the expected distribution of reconstructed track angles for positive muons. The cut that was applied to the data is shown.

Fig. 28

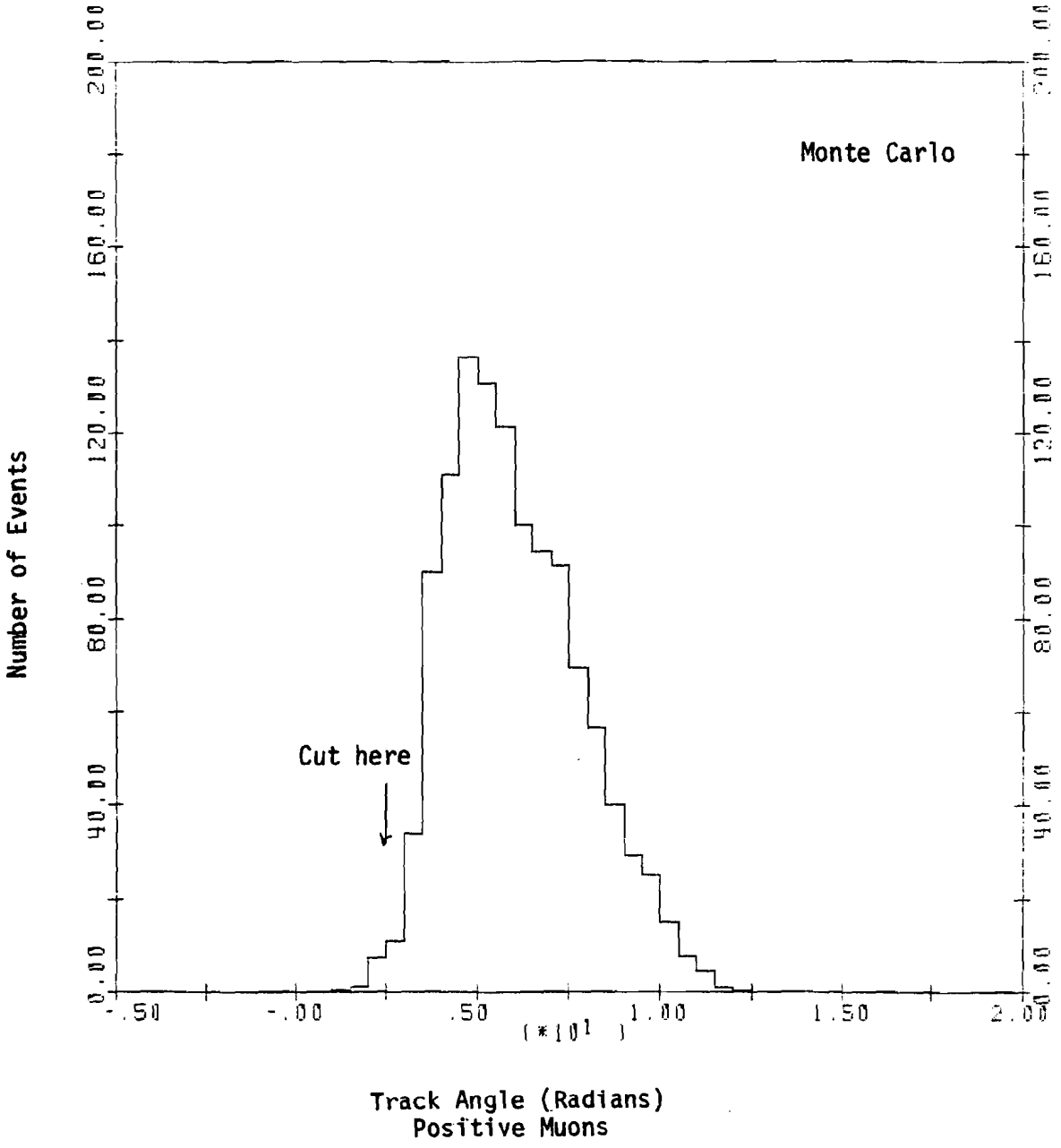
Monte Carlo
Cut here
Number of Events
200.00
160.00
120.00
80.00
40.00
0.00
-.50
-.00
.50
1.00
1.50
2.00
(*10¹)
Track Angle (Radians)
Positive Muons

Figure 29.--A Monte Carlo calculation of the expected distribution of reconstructed track angles for negative muons. The cut that was applied to the data is shown.

Fig. 29

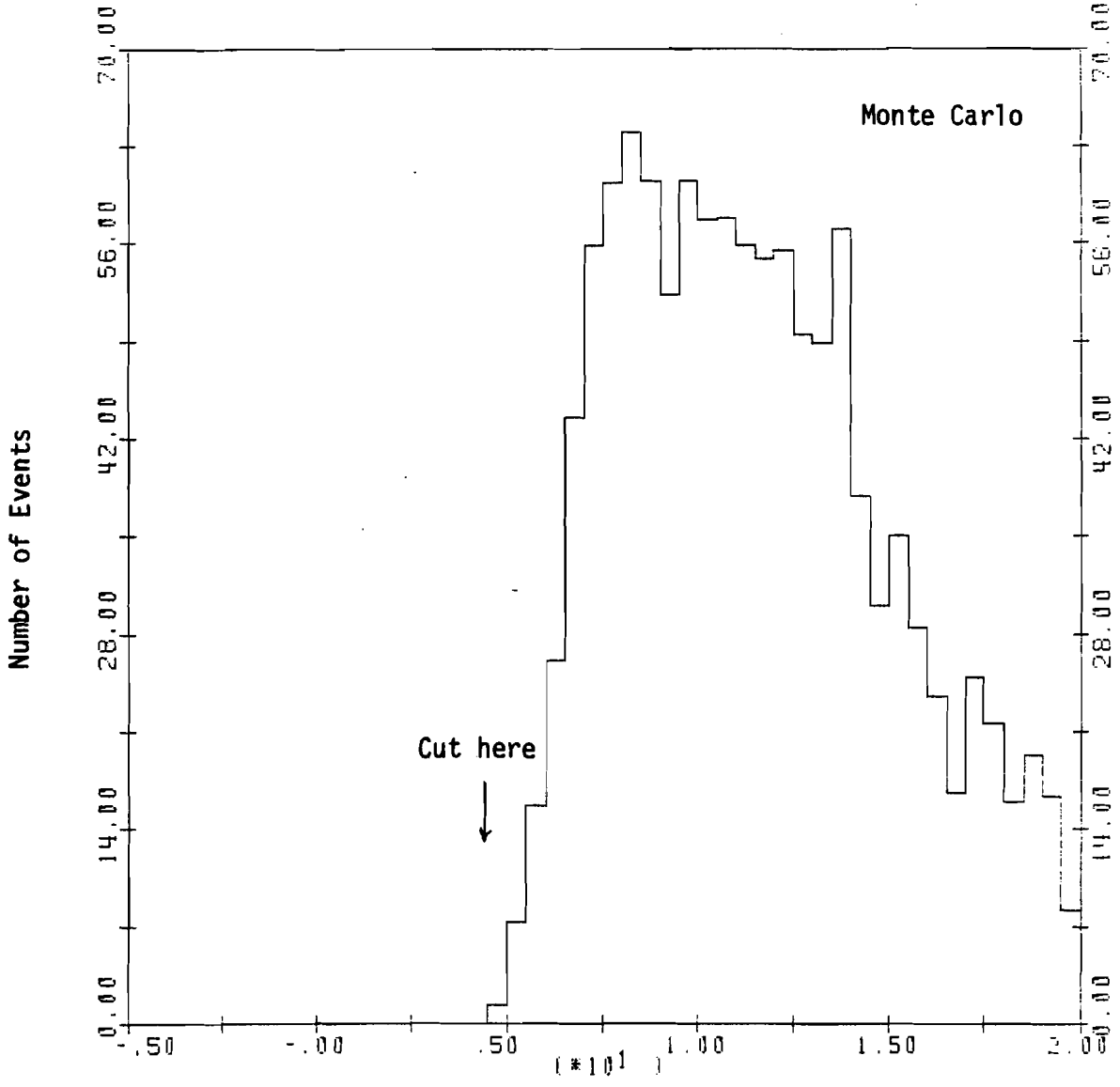
Monte Carlo
Cut here
Number of Events
70.00
56.00
42.00
28.00
14.00
0.00
-.50
-.00
.50
1.00
1.50
(*10^1)
Track Angle (Radians)
Negative Muons

Figure 30.--The target radius distribution for both sign tracks after the angle cuts.

Fig. 30

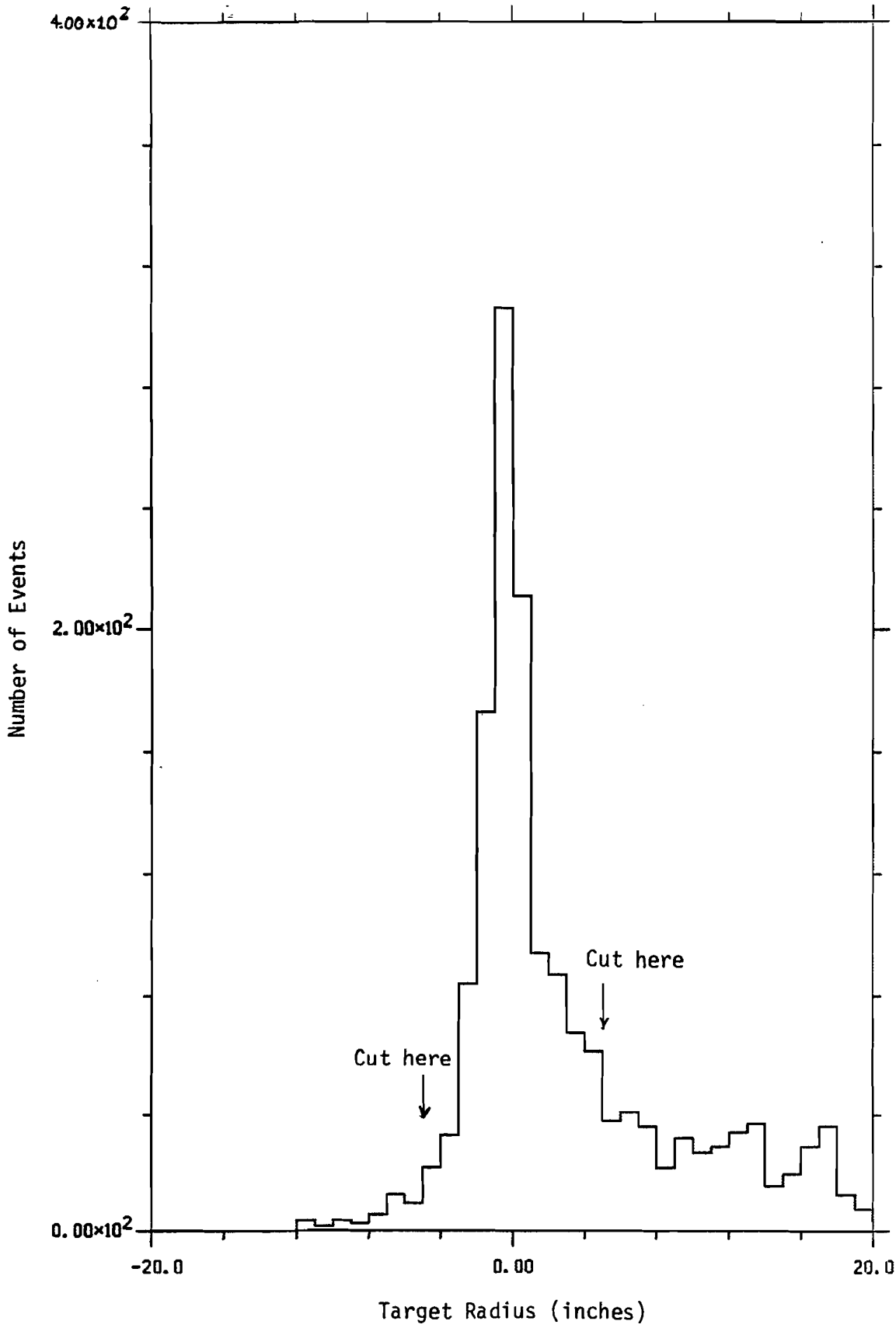
4.00x10²
2.00x10²
0.00x10²
Number of Events
Cut here
Cut here
-20.0
0.00
20.0
Target Radius (inches)

Figure 31.--A scatter plot of the target radius of the positive track versus that of the negative track for all dimuons in Figure 30.

Fig. 31

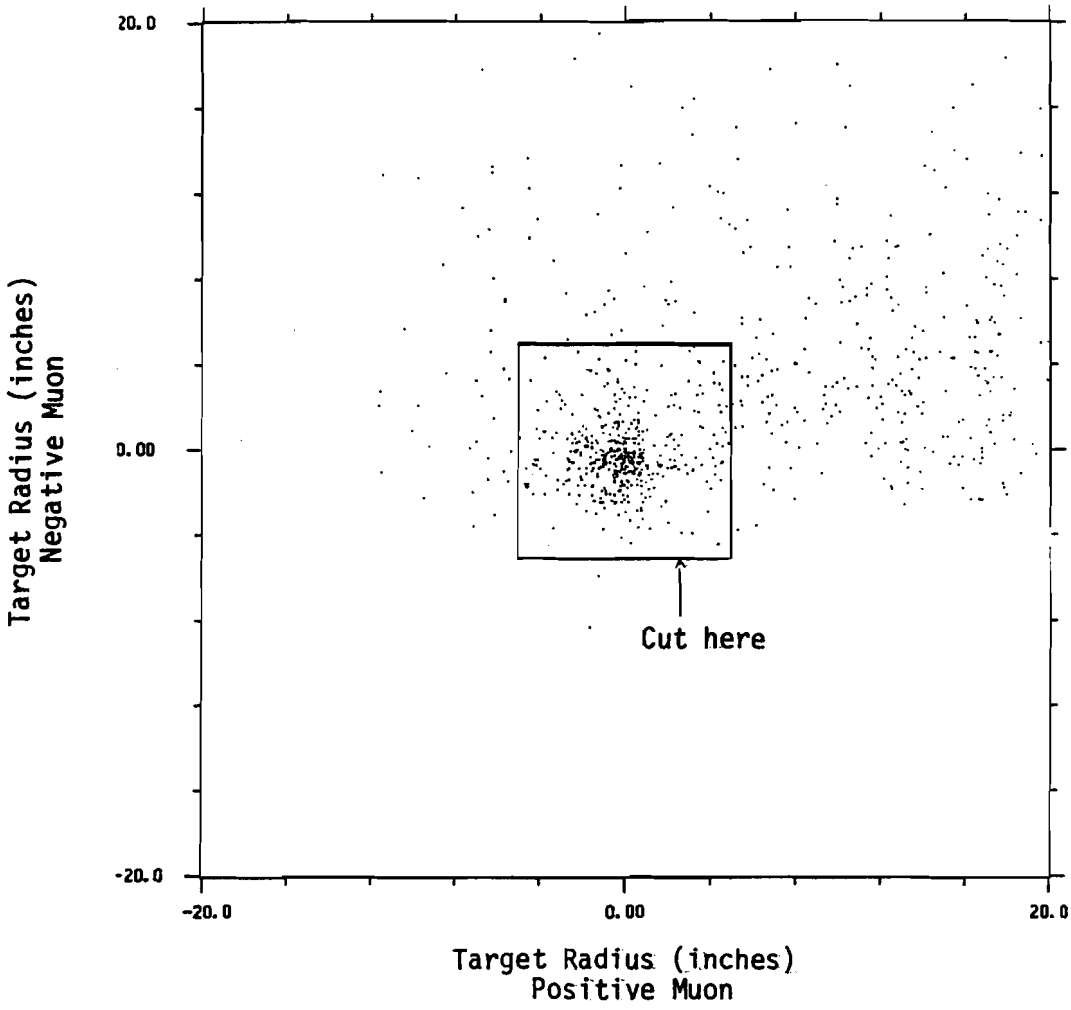
20.0
0.00
-20.0
-20.0
0.00
20.0
Target Radius (inches)
Negative Muon
Cut here
Target Radius (inches)
Positive Muon

Figure 32.--The distribution of the radial chi-squared function of the target constrained fit for all dimuon tracks that have passed the trigger pattern and target radius cuts.

Fig. 32

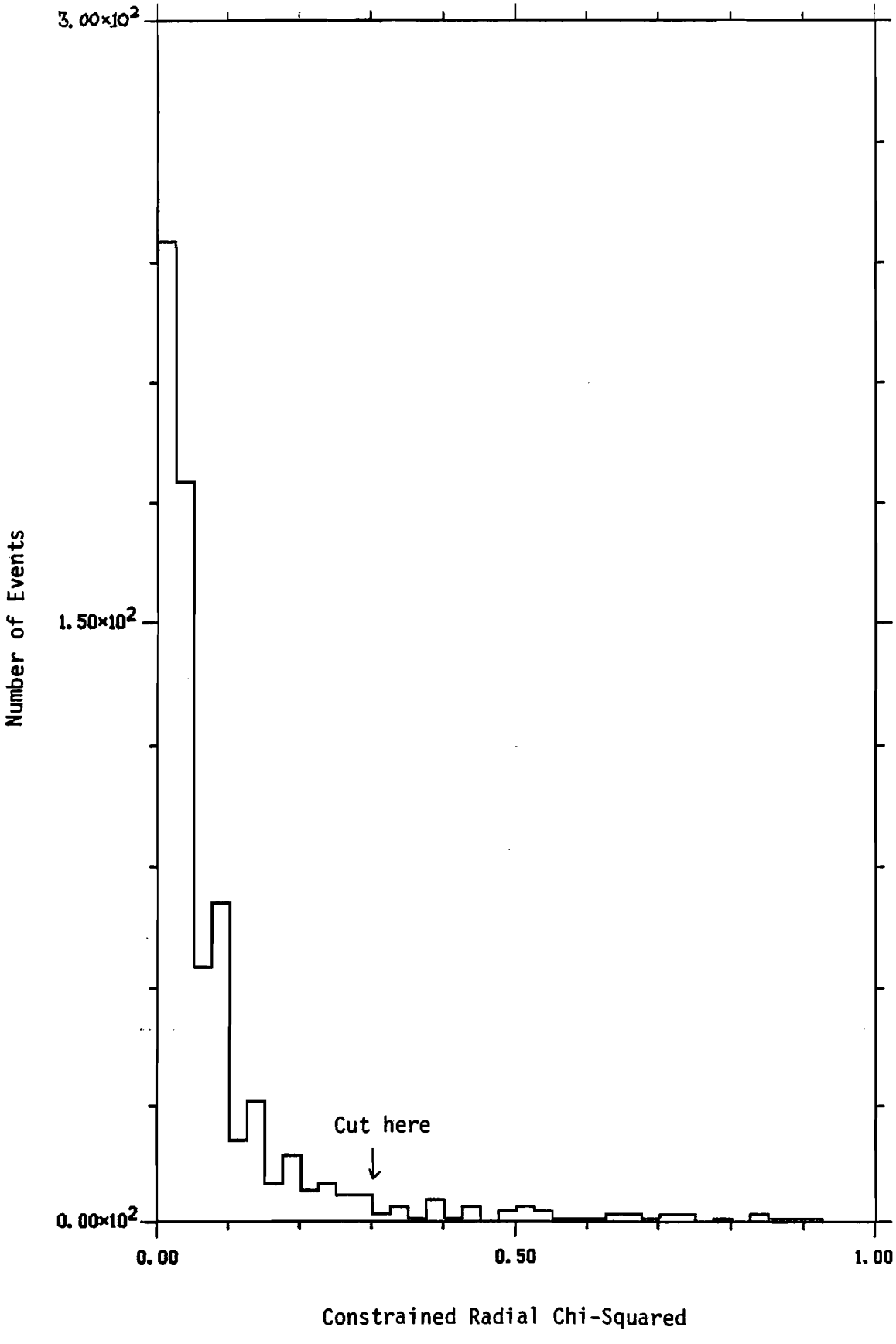
3.00×10²
1.50×10²
0.00×10²
Number of Events
Cut here
0.00
0.50
1.00
Constrained Radial Chi-Squared

Figure 33.--A scatter plot of the target constrained radial chi-squared function for the positive track versus that for the negative track for all events in Figure 32.

Fig. 33

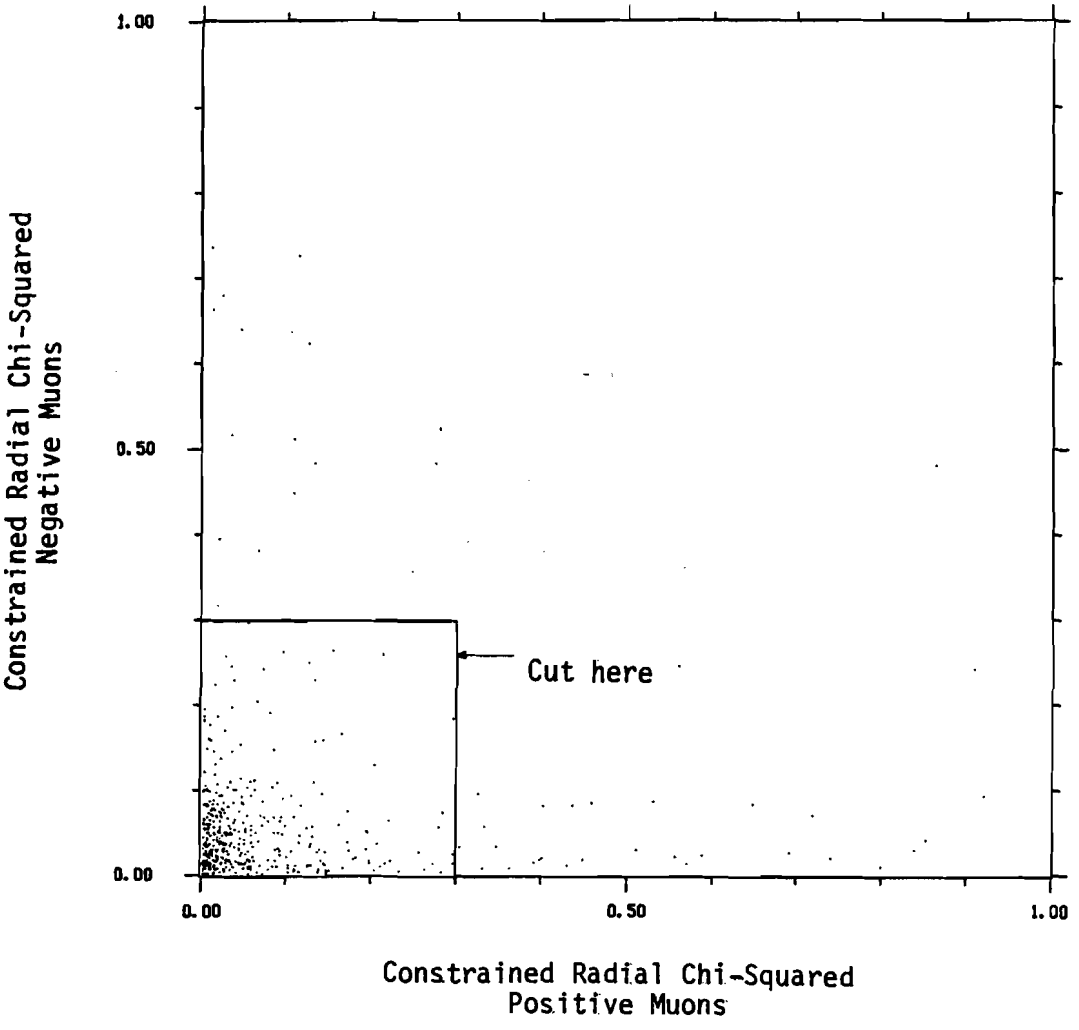
1.00
0.50
0.00
0.00
0.50
1.00
Cut here
Constrained Radial Chi-Squared
Negative Muons
Constrained Radial Chi-Squared
Positive Muons

Figure 34.--The mass distribution for the final event sample.

Fig. 34

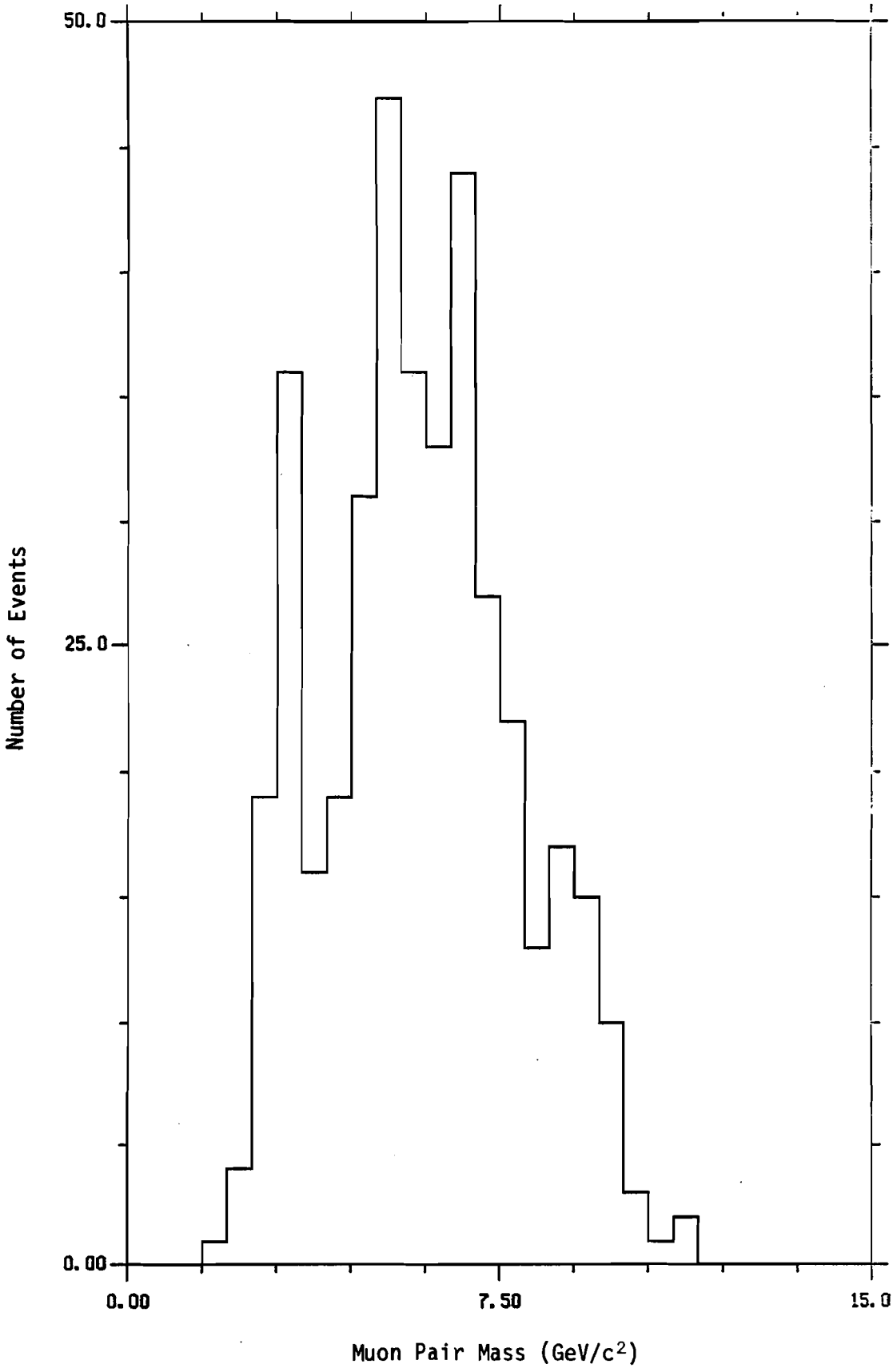

Figure 35.--Radial chi-squared distribution for the final event sample.

Fig. 35

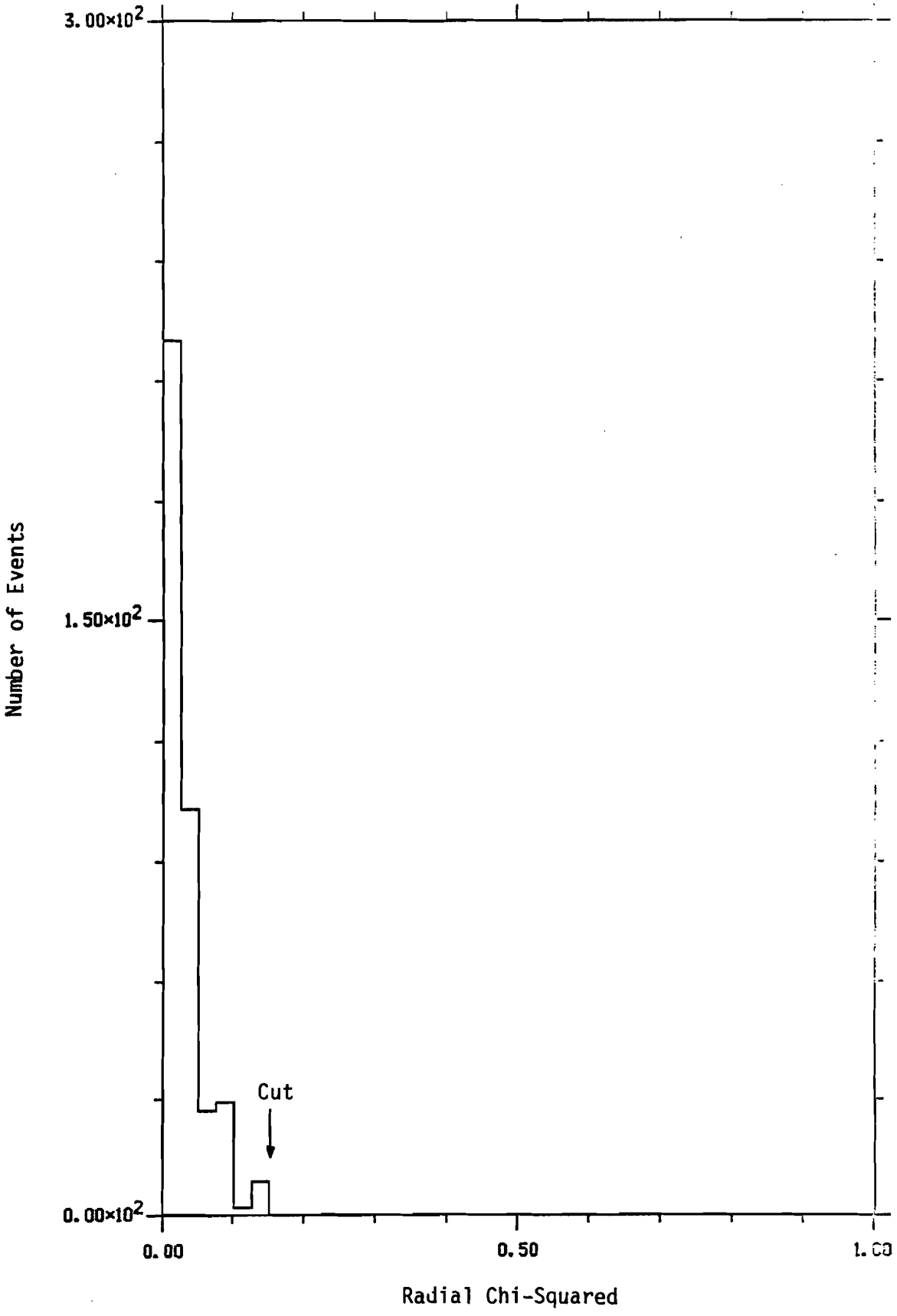
3.00×10²
1.50×10²
0.00×10²
Number of Events
Cut
0.00
0.50
1.00
Radial Chi-Squared

Figure 36.--Transverse chi-squared distribution for the final event sample.

Fig. 36

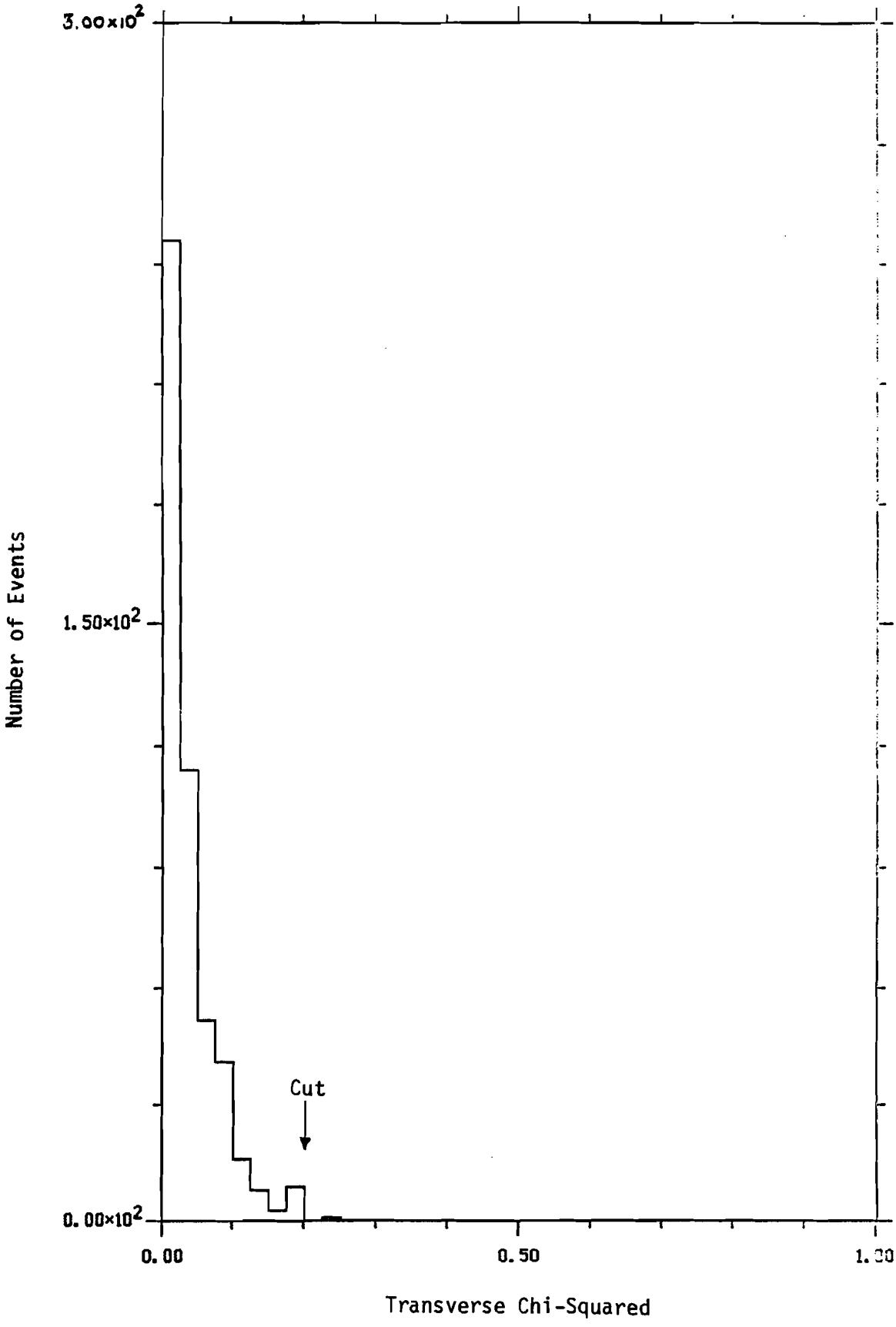
3.00×10²
1.50×10²
0.00×10²
Number of Events
Cut
0.00
0.50
1.00
Transverse Chi-Squared

Figure 37.--Target radius distribution for the positive muons of the final event sample.

Fig. 37

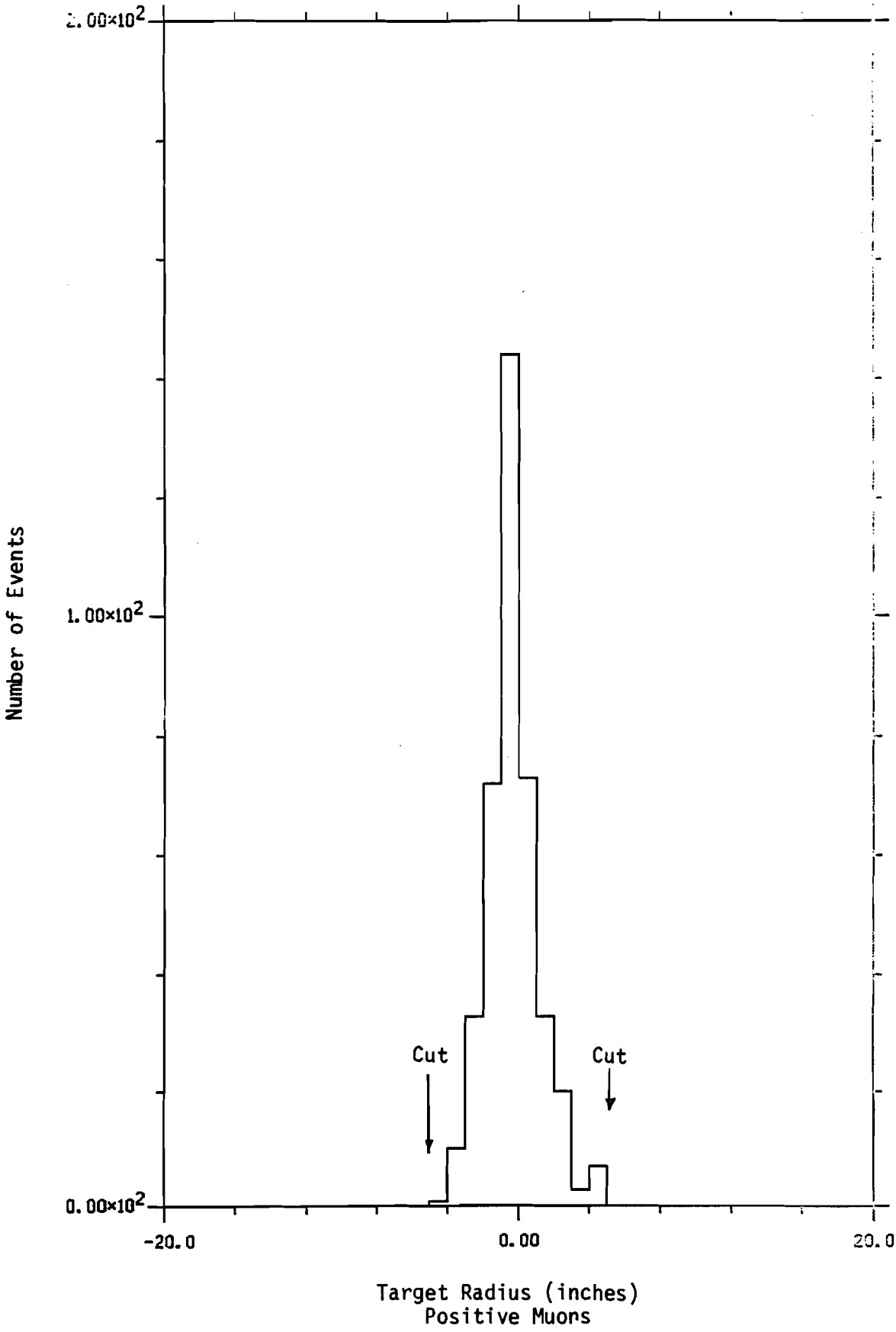
2.00×10²
1.00×10²
0.00×10²
Number of Events
Cut
Cut
-20.0
0.00
20.0
Target Radius (inches)
Positive Muons

Figure 38.--The target radius distribution for the negative muons of the final event sample.

Fig. 38

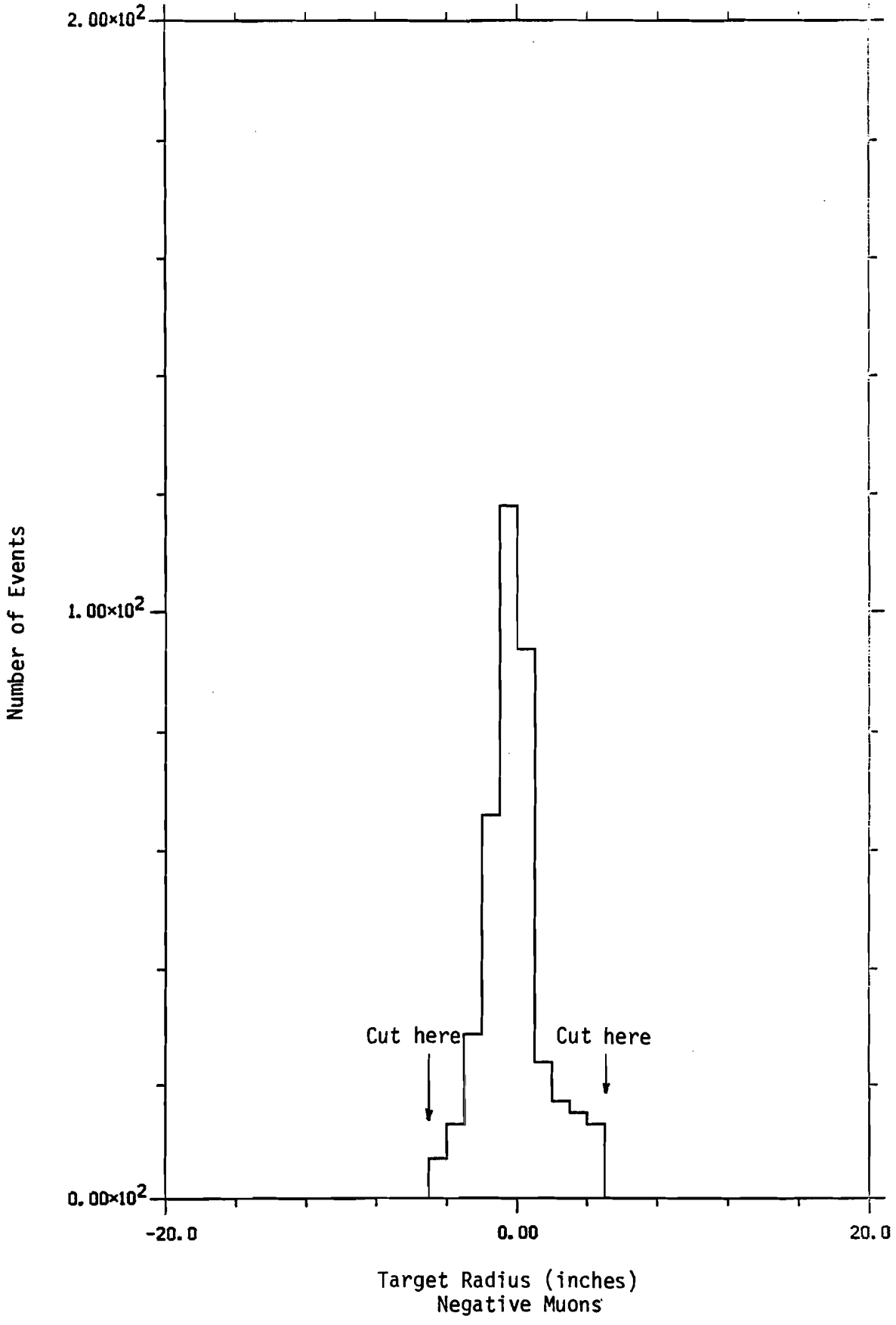
2.00×10²
1.00×10²
0.00×10²
Number of Events
Cut here
Cut here
-20.0
0.00
20.0
Target Radius (inches)
Negative Muons

Figure 39.--The track angle distribution for the positive muons of the final event sample.

Fig. 39

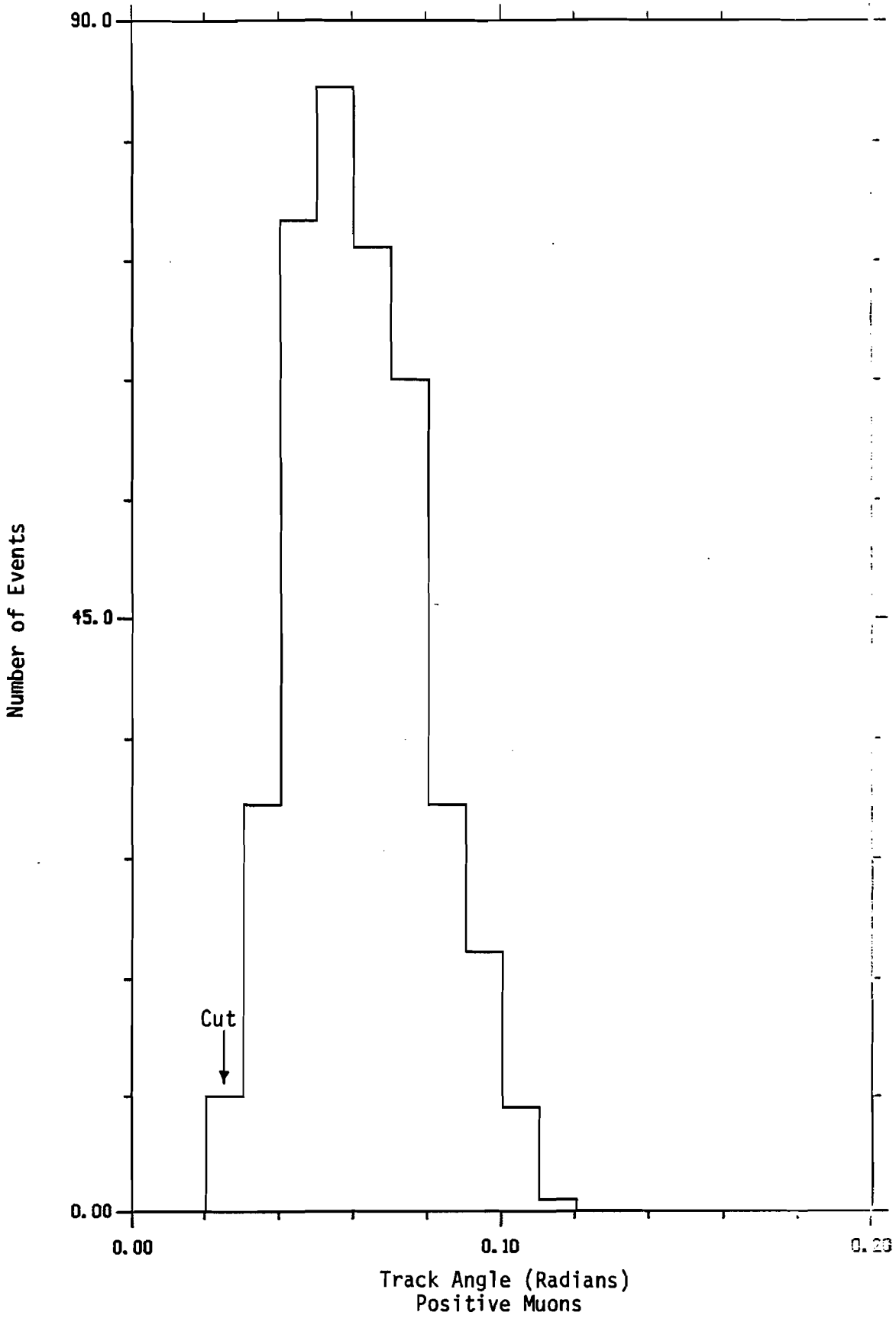
90.0
45.0
0.00
Number of Events
Cut
0.00
0.10
0.20
Track Angle (Radians)
Positive Muons

Figure 40.--The track angle distribution for the negative muons of the final event sample.

Fig. 40

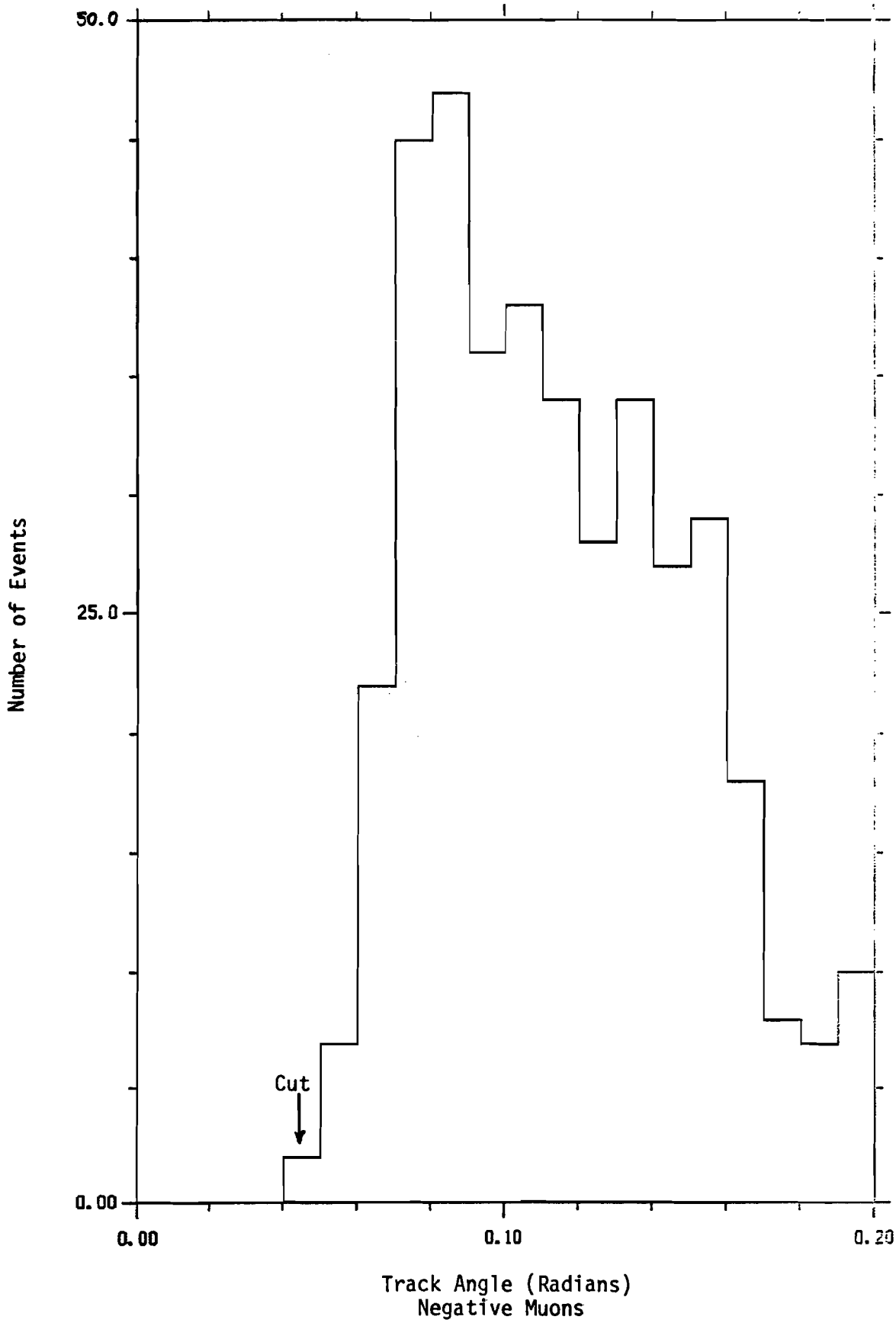
50.0
25.0
0.00
Number of Events
Cut
0.00
0.10
0.20
Track Angle (Radians)
Negative Muons

Figure 41.--The mass distribution for the accidental background subtracted, total data sample. The background mass distribution is plotted as a solid histogram.

Fig. 41

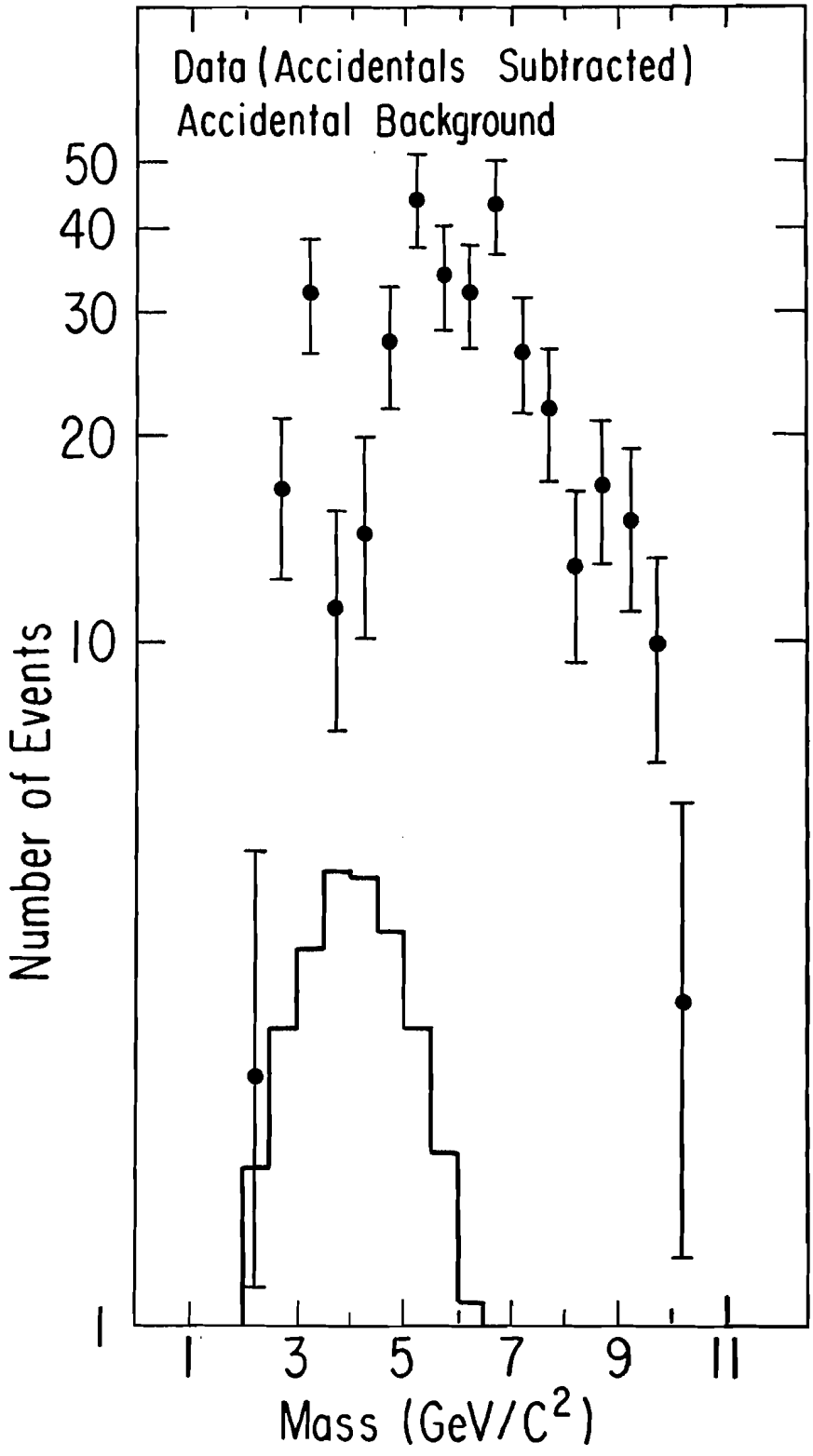
Data (Accidentals Subtracted)
Accidental Background
50
40
30
20
10
1
Number of Events
1
3
5
7
9
11
Mass (GeV/C²)

Figure 42.--The transverse momentum distribution for the accidental background subtracted total data sample with mass larger than 4.0 GeV/c^2. The accidental background P_T distribution is plotted as the solid histogram.

Fig. 42

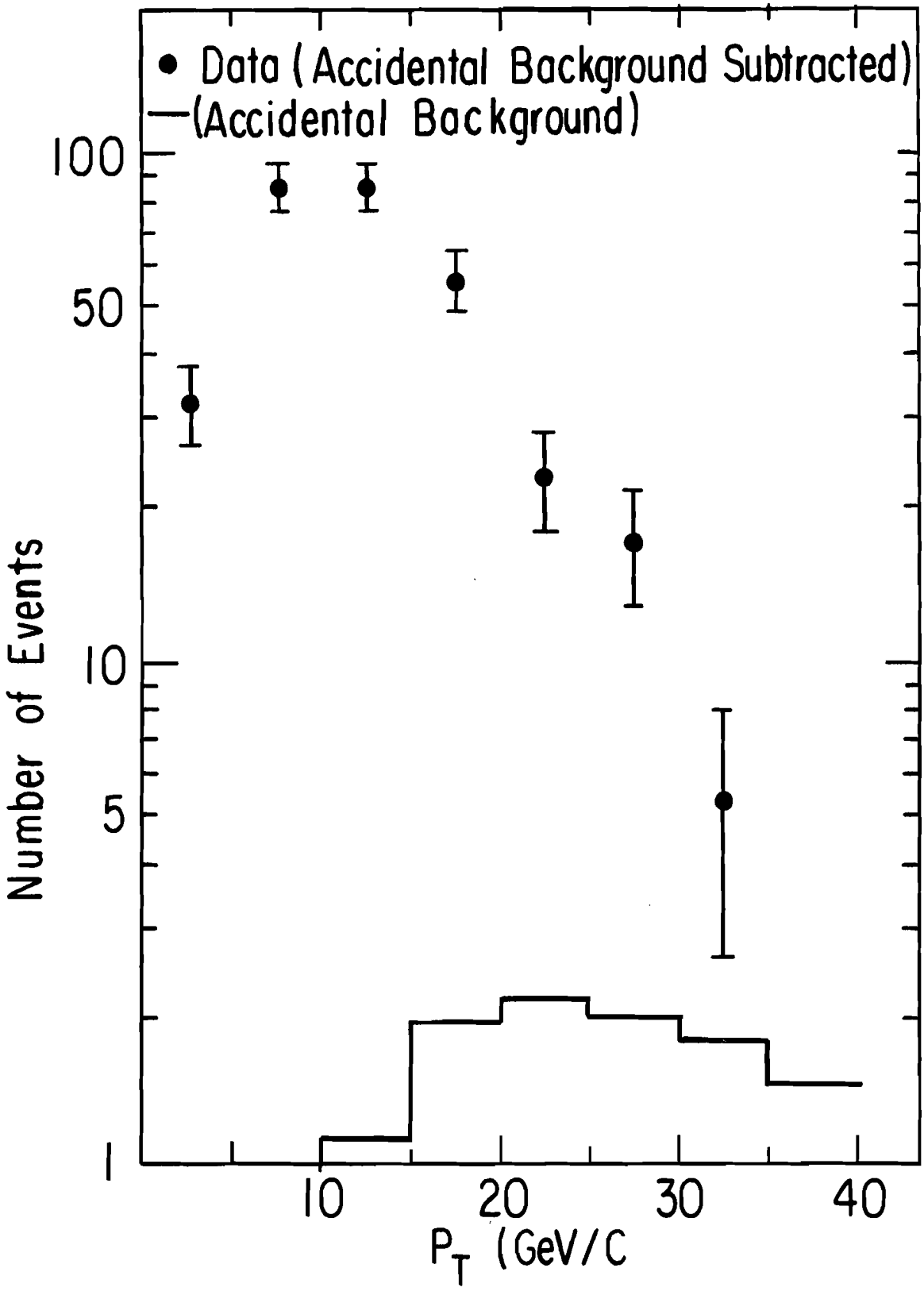
• Data (Accidental Background Subtracted)
—(Accidental Background)
100
50
10
5
1
Number of Events
10
20
30
40
P_T (GeV/C

Figure 43.--The ratio of the total segmented ion chamber output IC711 + IC712 + IC713 to the output of the adjacent ion chamber IC710.

Fig. 43

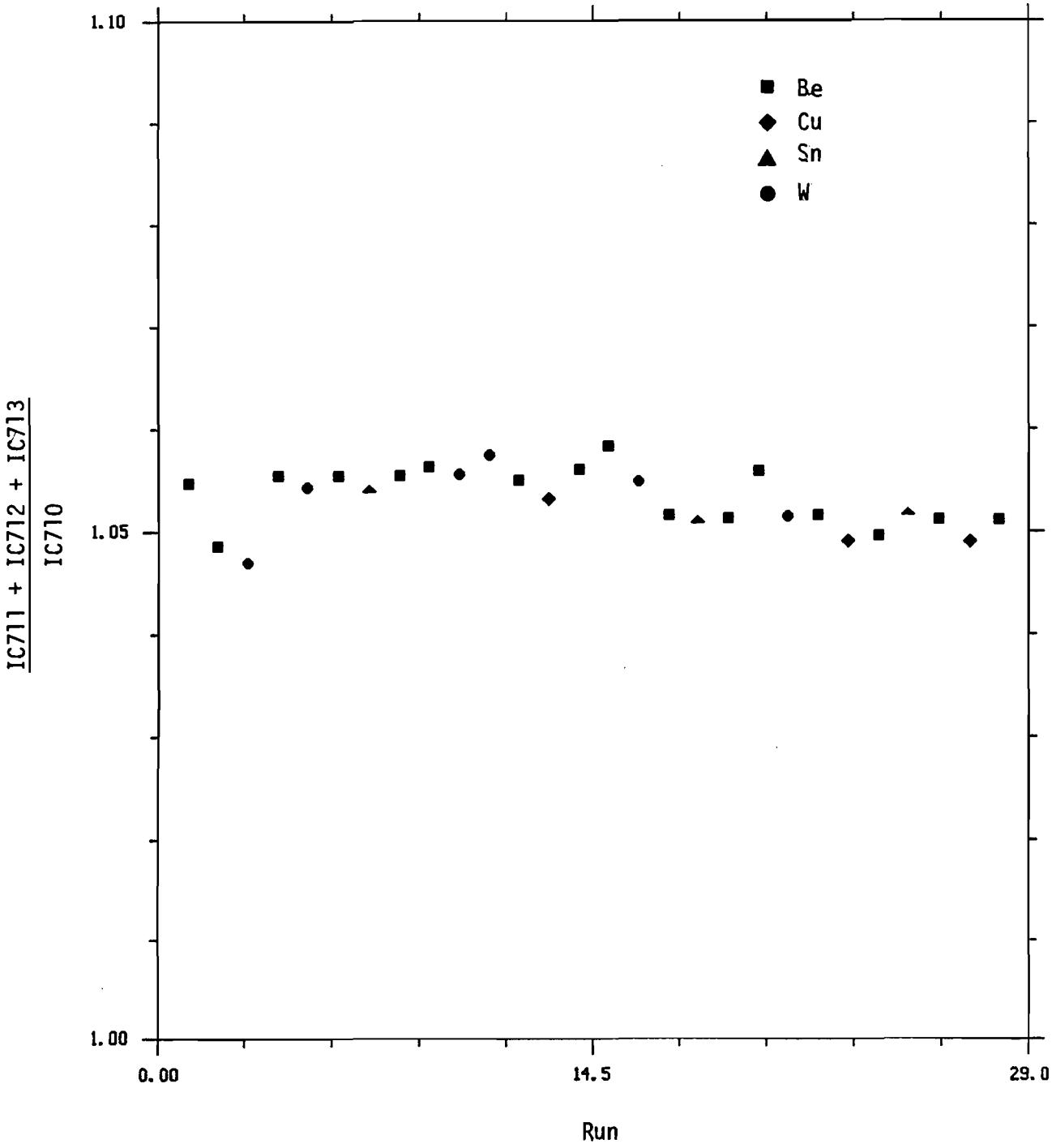

Figure 44.--The ratio of the innermost channel of the segmented ion chamber, IC712, to the secondary emission monitor that measured the primary proton flux to the P-West secondary beam production target, SE701. The ratio is proportional to the pion yield of the secondary beam.

Fig. 44

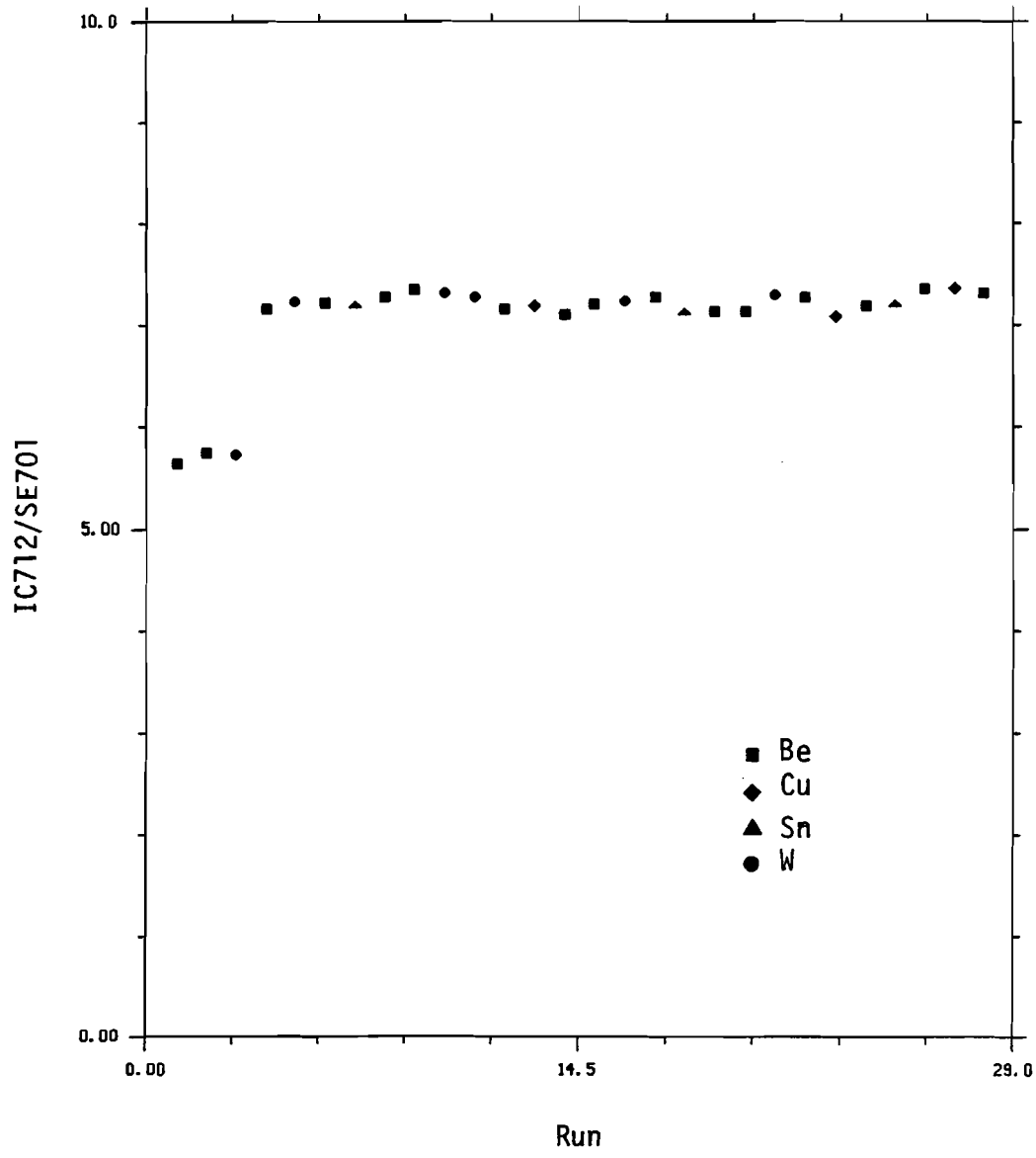

Figure 45.--The fractional livetime of the spectrometer plotted versus run.

Fig. 45

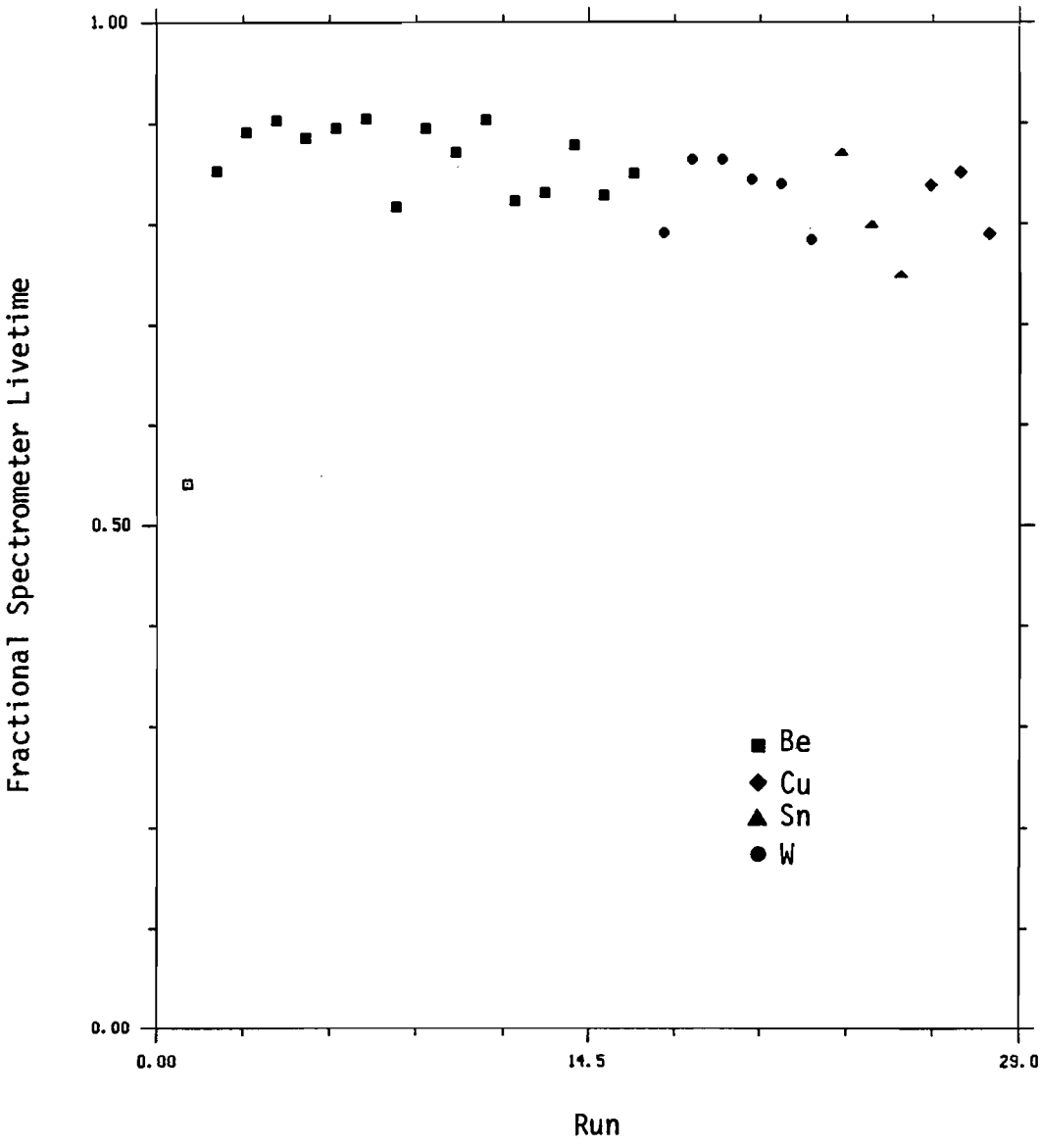
1.00
0.50
0.00
0.00
14.5
29.0
Fractional Spectrometer Livetime
Run
Be
Cu
Sn
W

Figure 46.--The raw rate of single octant matrix triggers normalized to the primary proton flux is plotted against run. The single octant trigger rate was scaled independently of livetime.

Fig. 46

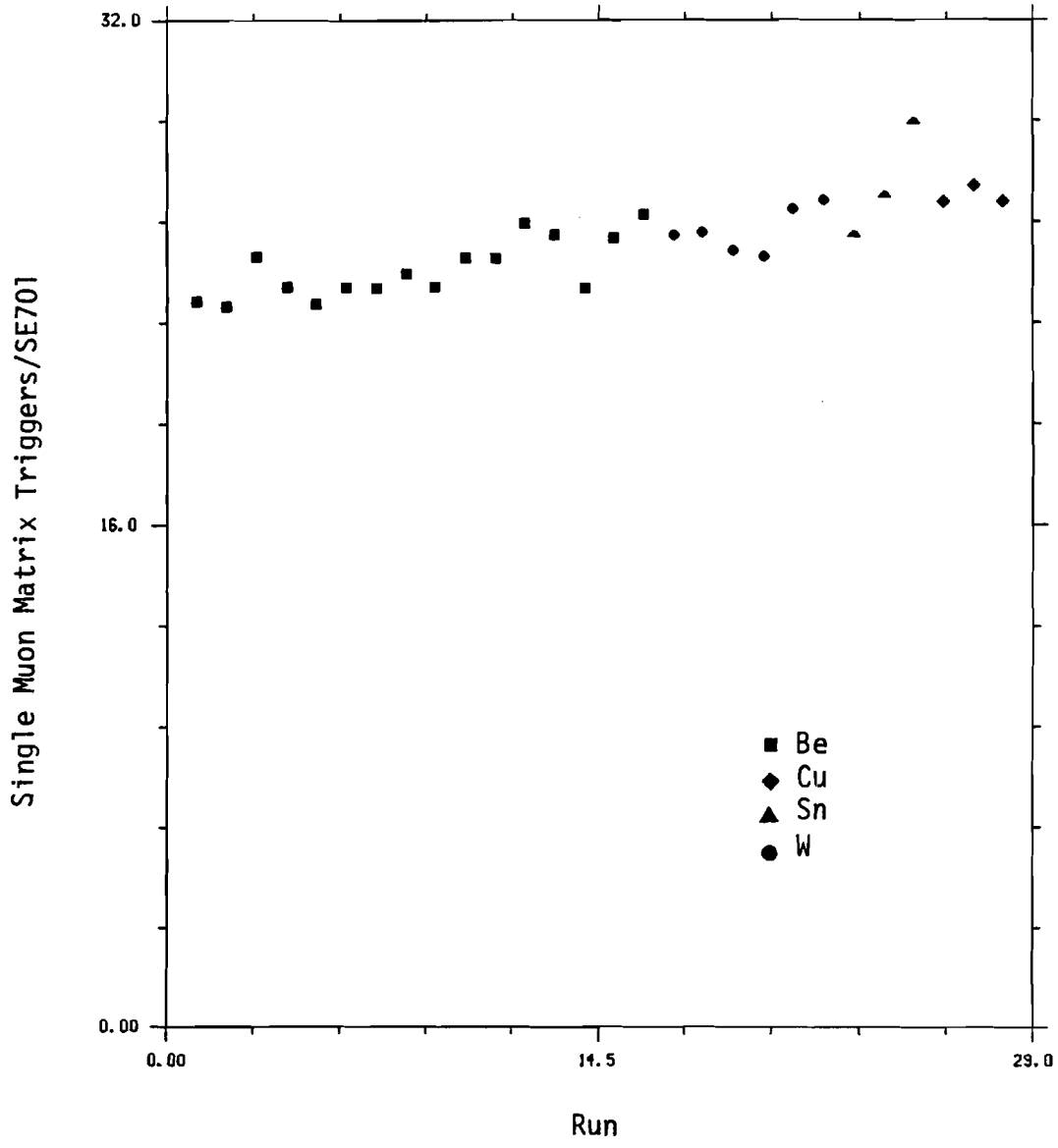
32.0
16.0
0.00
0.00
14.5
29.0
Run
Single Muon Matrix Triggers/SE701
Be
Cu
Sn
W

Figure 47.--Efficiency of the Gap 1 chamber planes as a function of distance from the first wire in the chamber.

Fig. 47

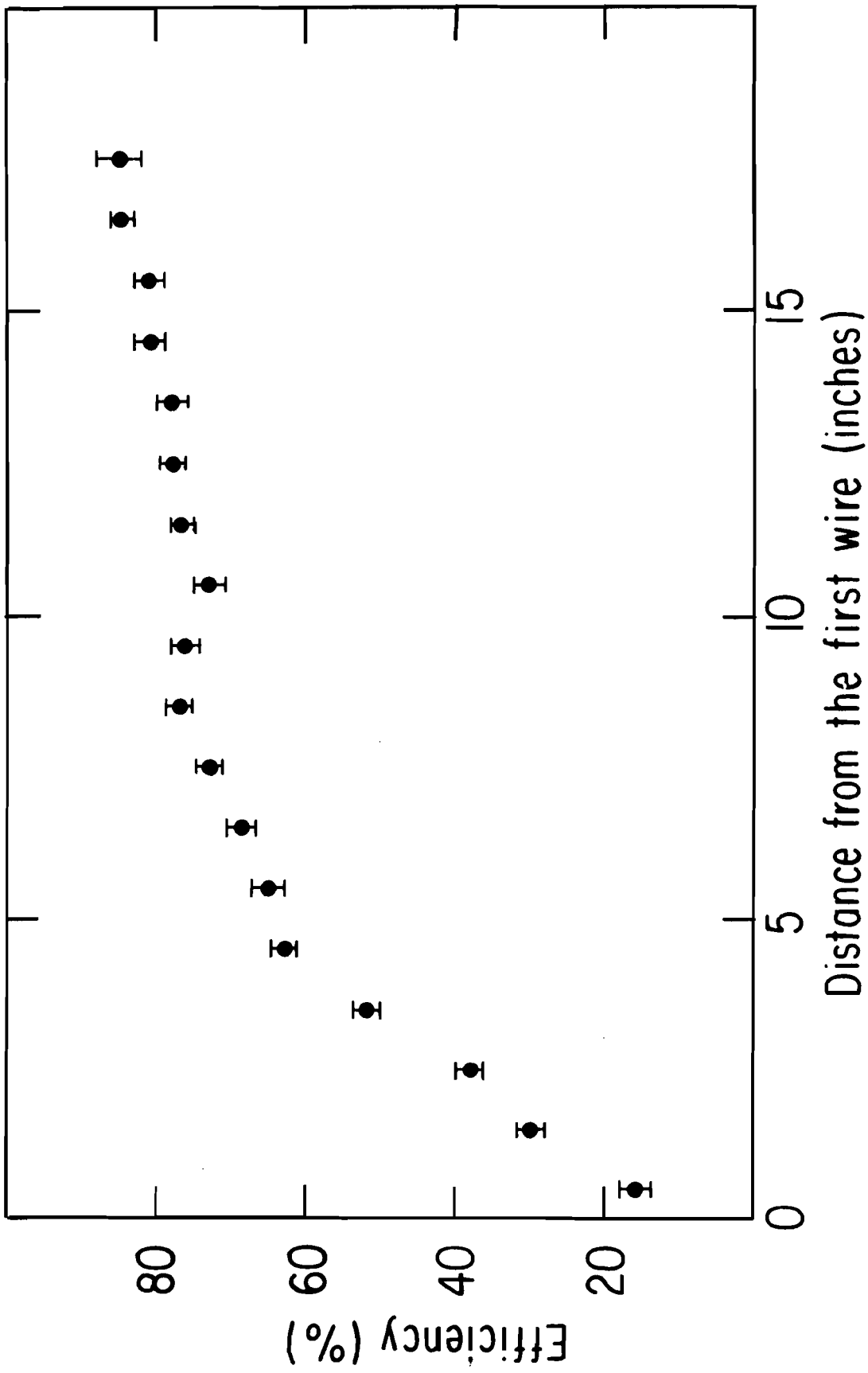
Efficiency (%)
80
60
40
20
Distance from the first wire (inches)
0
5
10
15

Figure 48.--Efficiency of the Gap 2 chamber planes as a function of distance from the first wire. The measurements at large radii have very poor statistics and are not shown.

Fig. 48

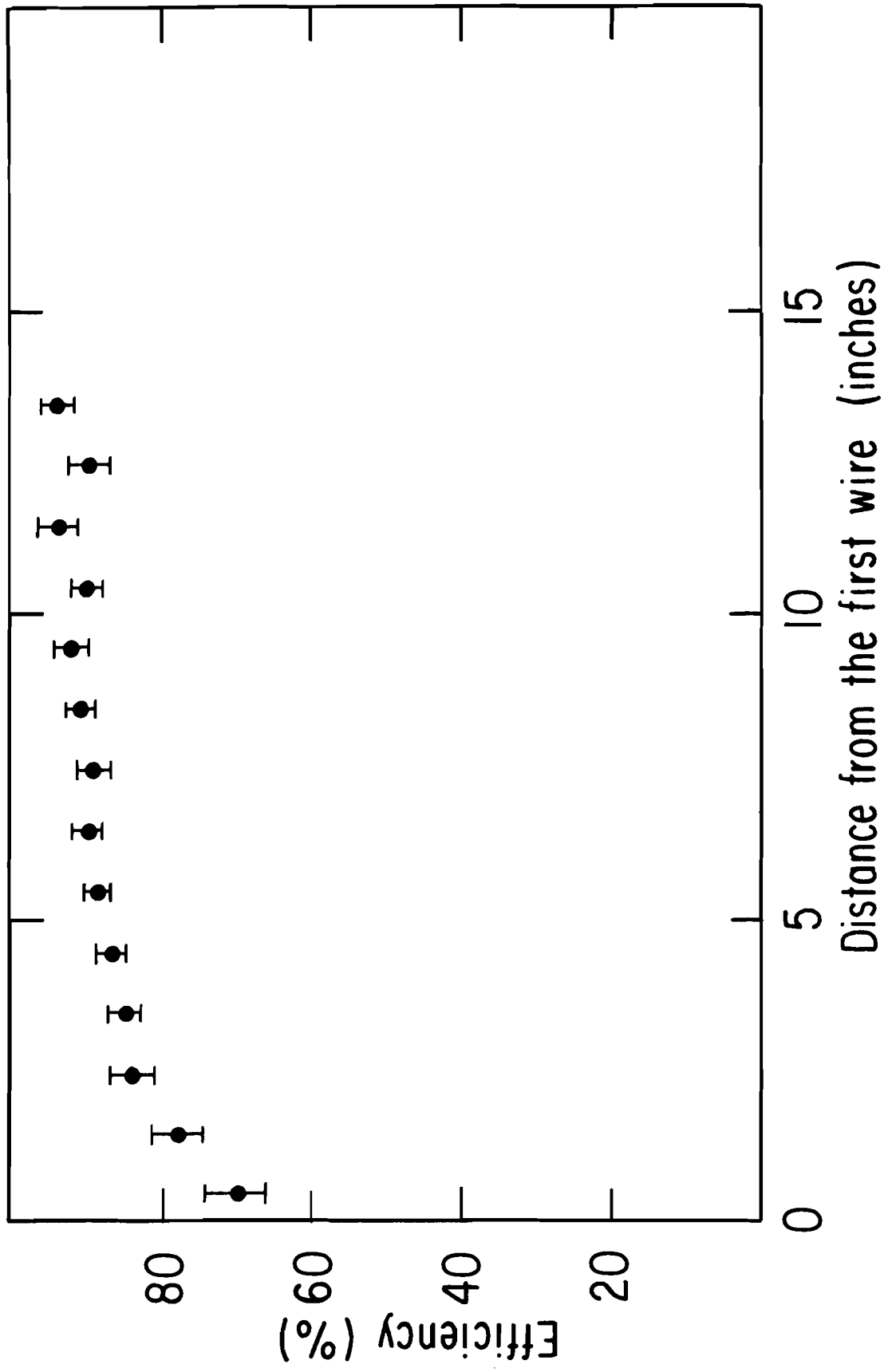
Efficiency (%)
80
60
40
20
0
5
10
15
Distance from the first wire (inches)

Figure 49.--The ratio of background subtracted events to livetime corrected flux is plotted for each run.

Fig. 49

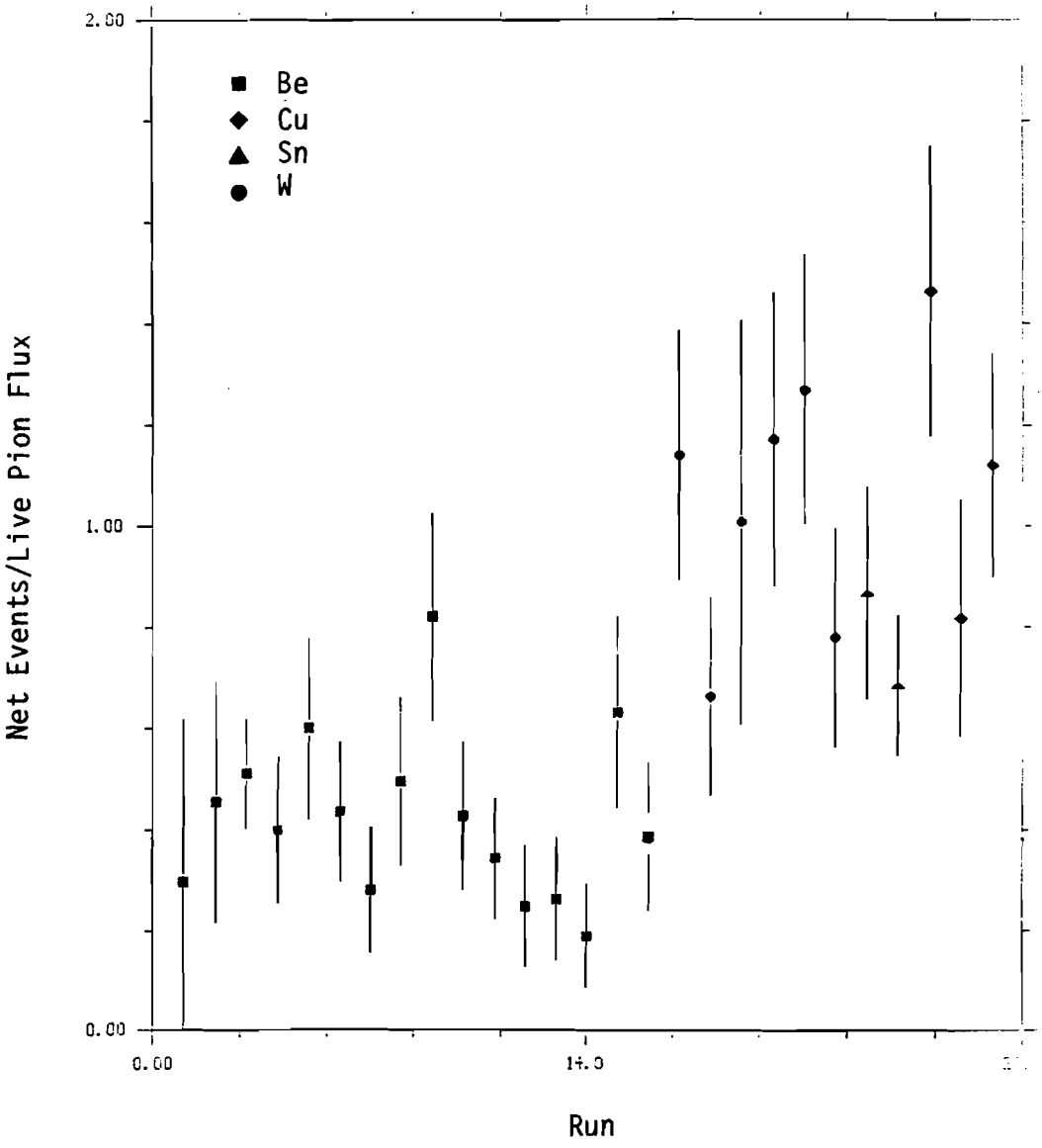

Figure 50.--A comparison of the beryllium mass distribution and the beryllium Monte Carlo.

Fig. 50

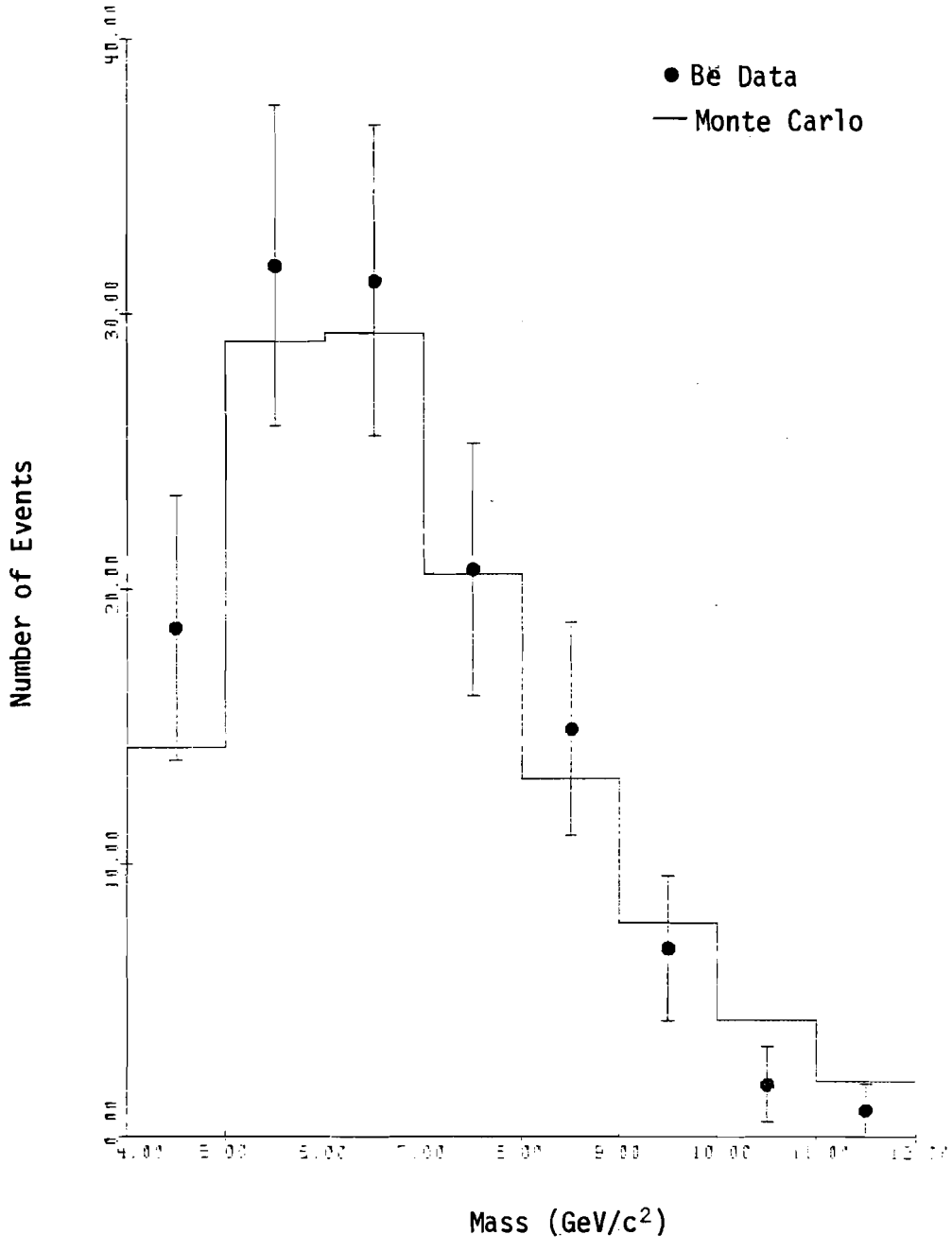

Figure 51.--A comparison of the beryllium P_T distribution and the beryllium Monte Carlo.

Fig. 51

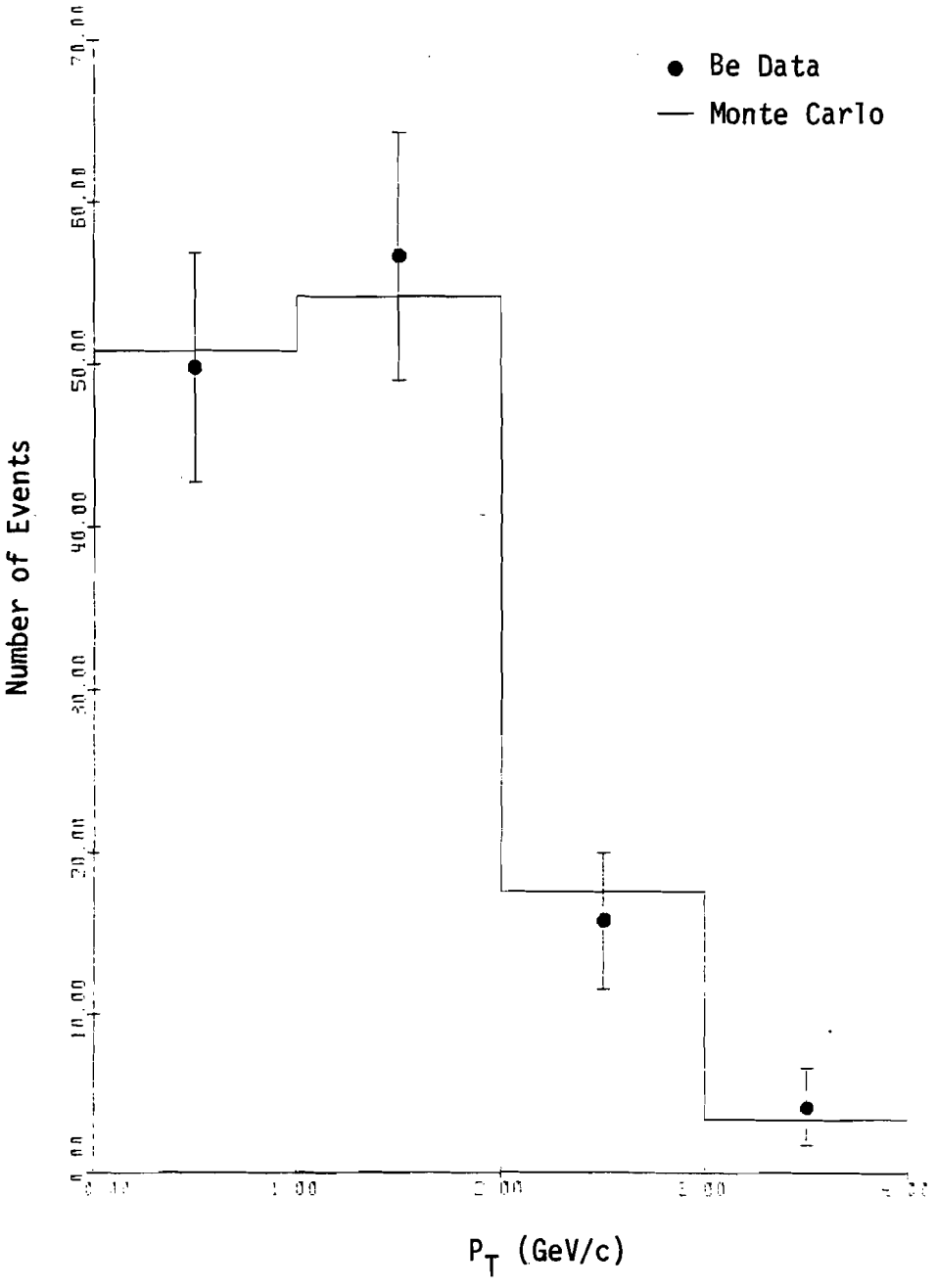
Be Data
Monte Carlo
Number of Events
70.00
60.00
50.00
40.00
30.00
20.00
10.00
0.00
1.00
2.00
3.00
P_T (GeV/c)

Figure 52.--A comparison of the tin mass distribution with the Monte Carlo.

Fig. 52

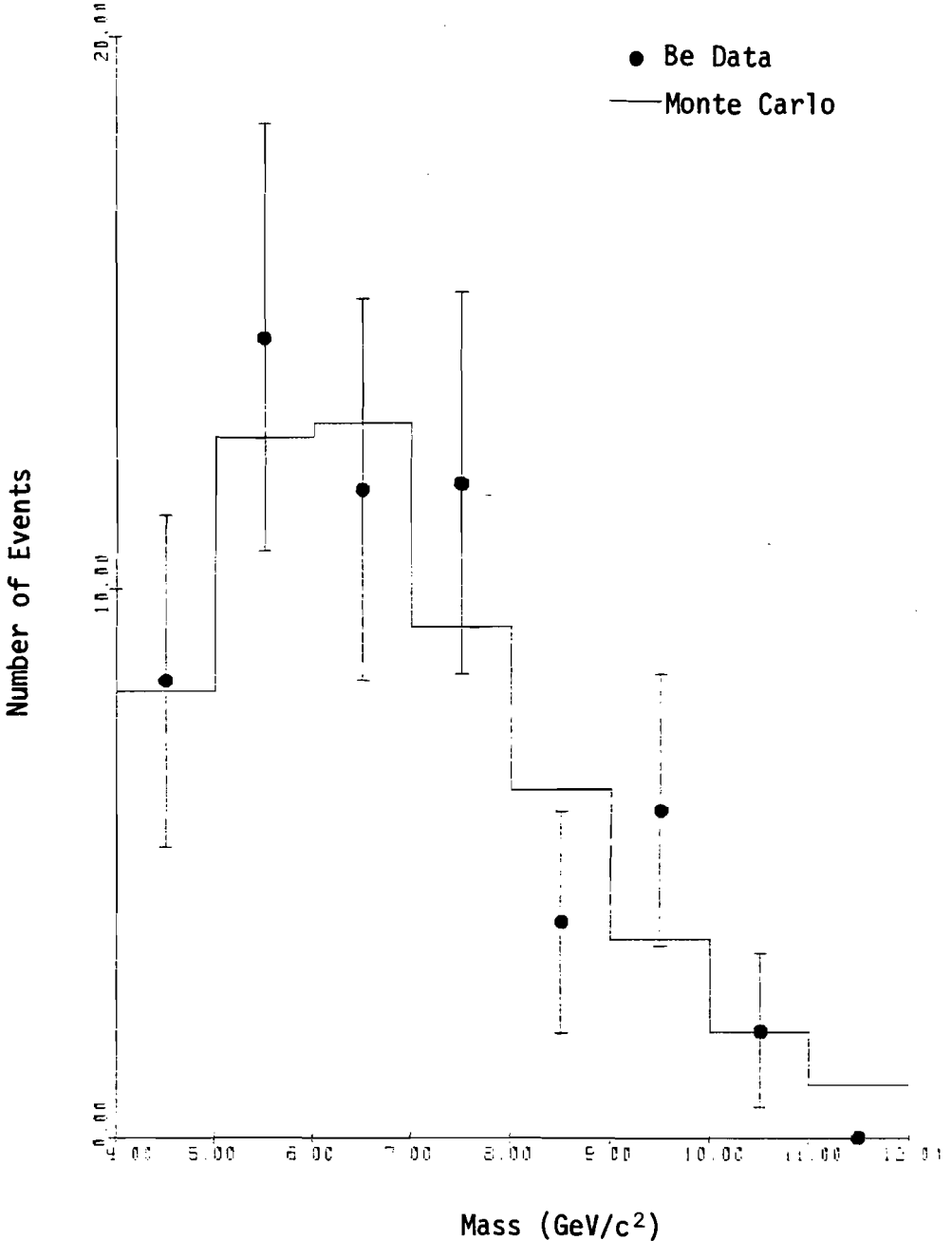
● Be Data
—— Monte Carlo
Number of Events
20.00
10.00
0.00
5.00
6.00
7.00
8.00
9.00
10.00
Mass (GeV/c²)

Figure 53.--A comparison of the tin P_T distribution with the Monte Carlo.

Fig. 53

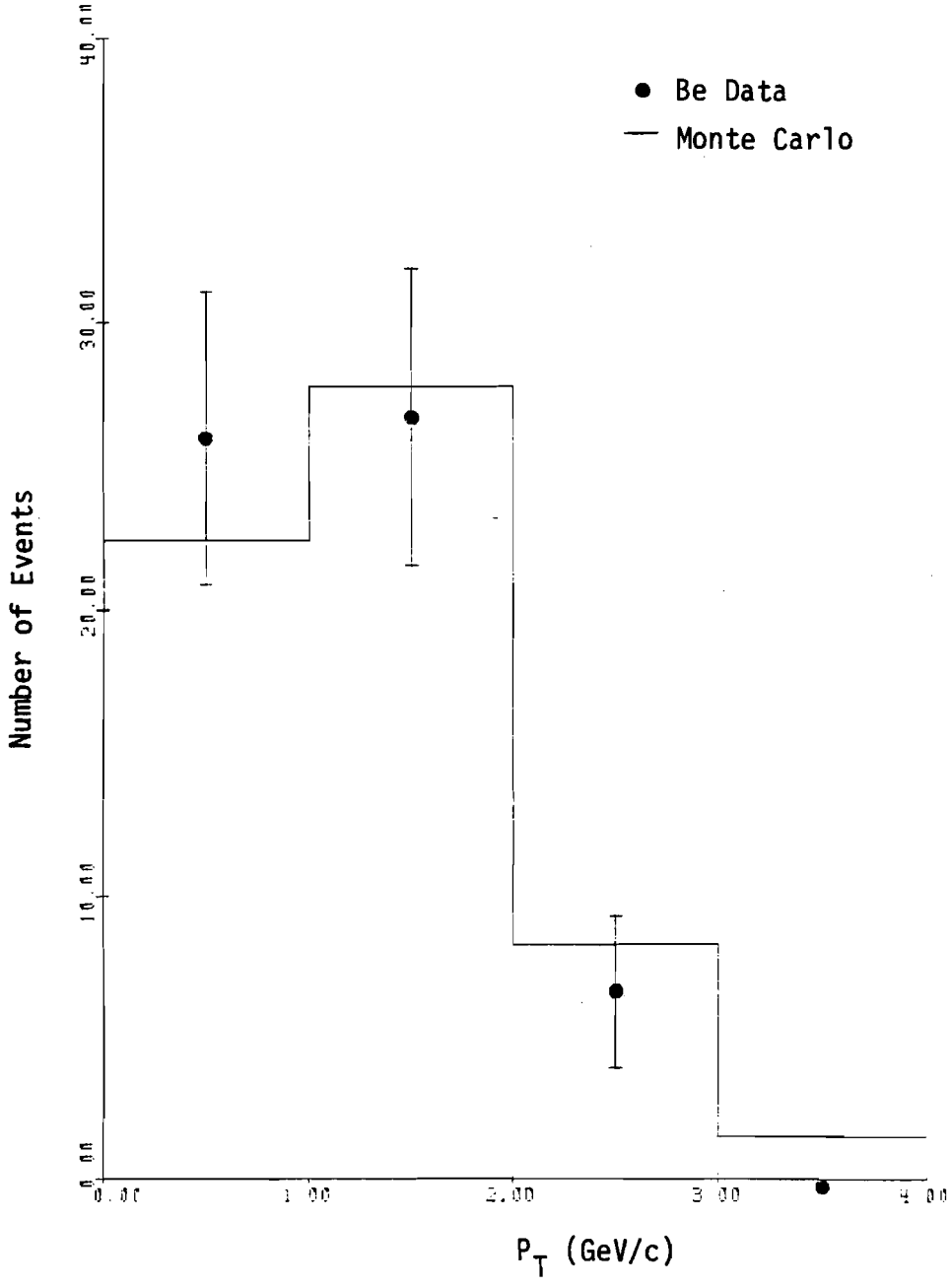
Be Data
Monte Carlo
Number of Events
40.00
30.00
20.00
10.00
0.00
0.00
1.00
2.00
3.00
4.00
P_T (GeV/c)

Figure 54.--The spectrometer acceptance as a function of the Z position of the vertex in the beryllium target.

Fig. 54

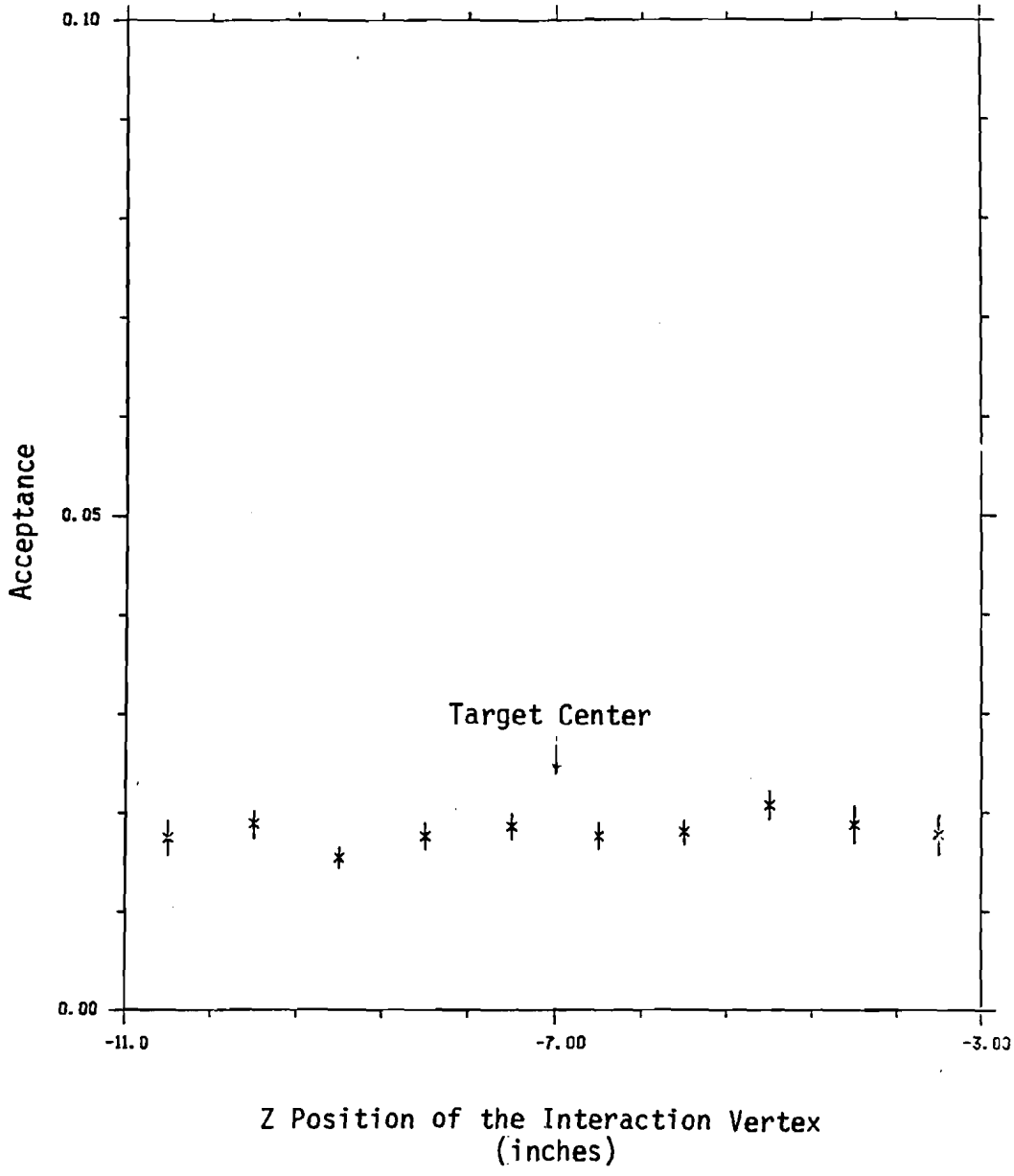
0.10
0.05
0.00
Acceptance
Target Center
-11.0
-7.00
-3.00
Z Position of the Interaction Vertex
(inches)

Figure 55.--A comparison of the psi Monte Carlo mass distribution with the total, accidentals subtracted data sample. The Monte Carlo has been normalized to the 3.0 - 3.5 GeV/c^2 data point.

Fig. 55

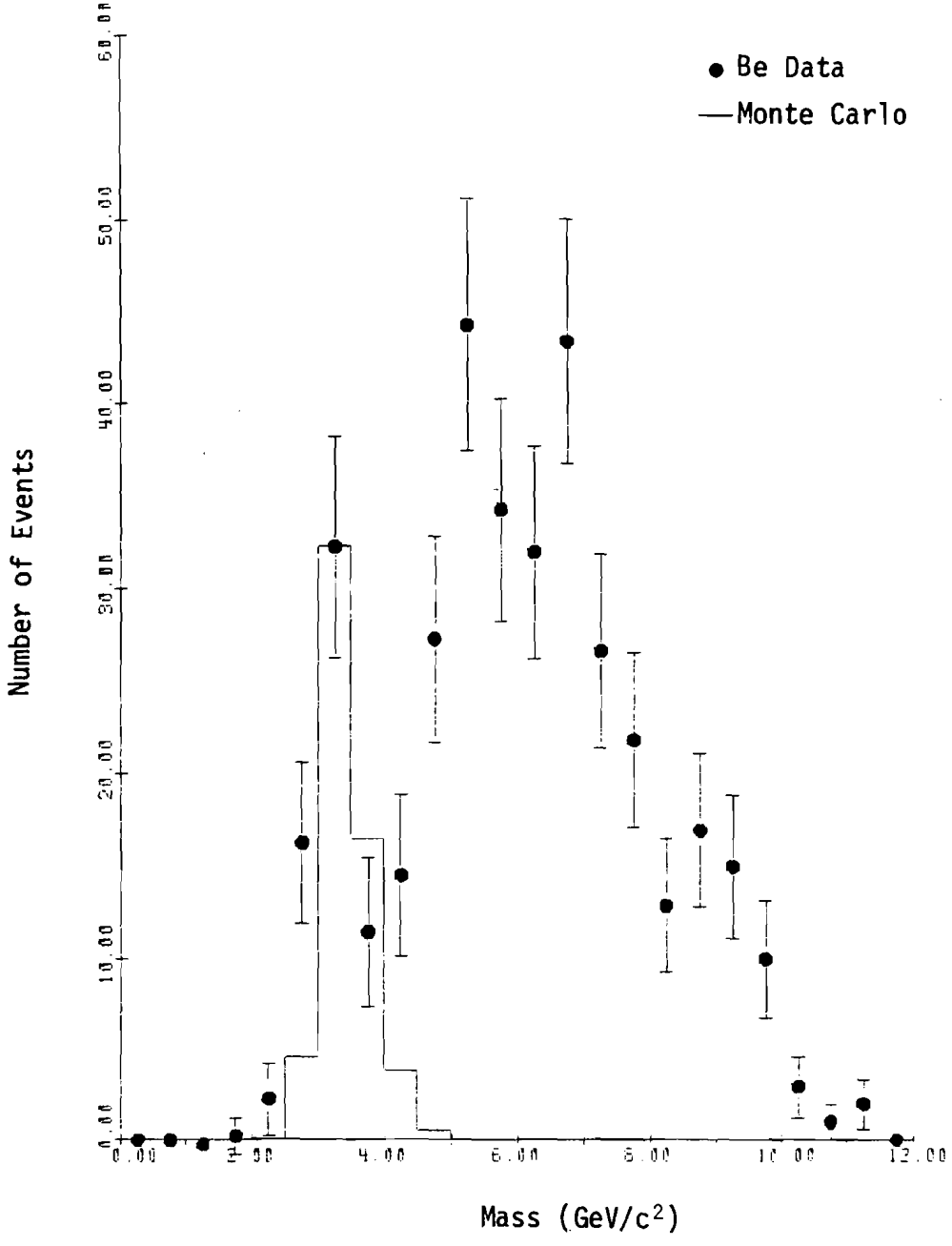
● Be Data
—Monte Carlo
Number of Events
Mass (GeV/c²)
0.00
10.00
20.00
30.00
40.00
50.00
60.00
0.00
2.00
4.00
6.00
8.00
10.00
12.00

Figure 56.--The expected shape of the upsilon family mass distribution from the Monte Carlo calculation.

Fig. 56

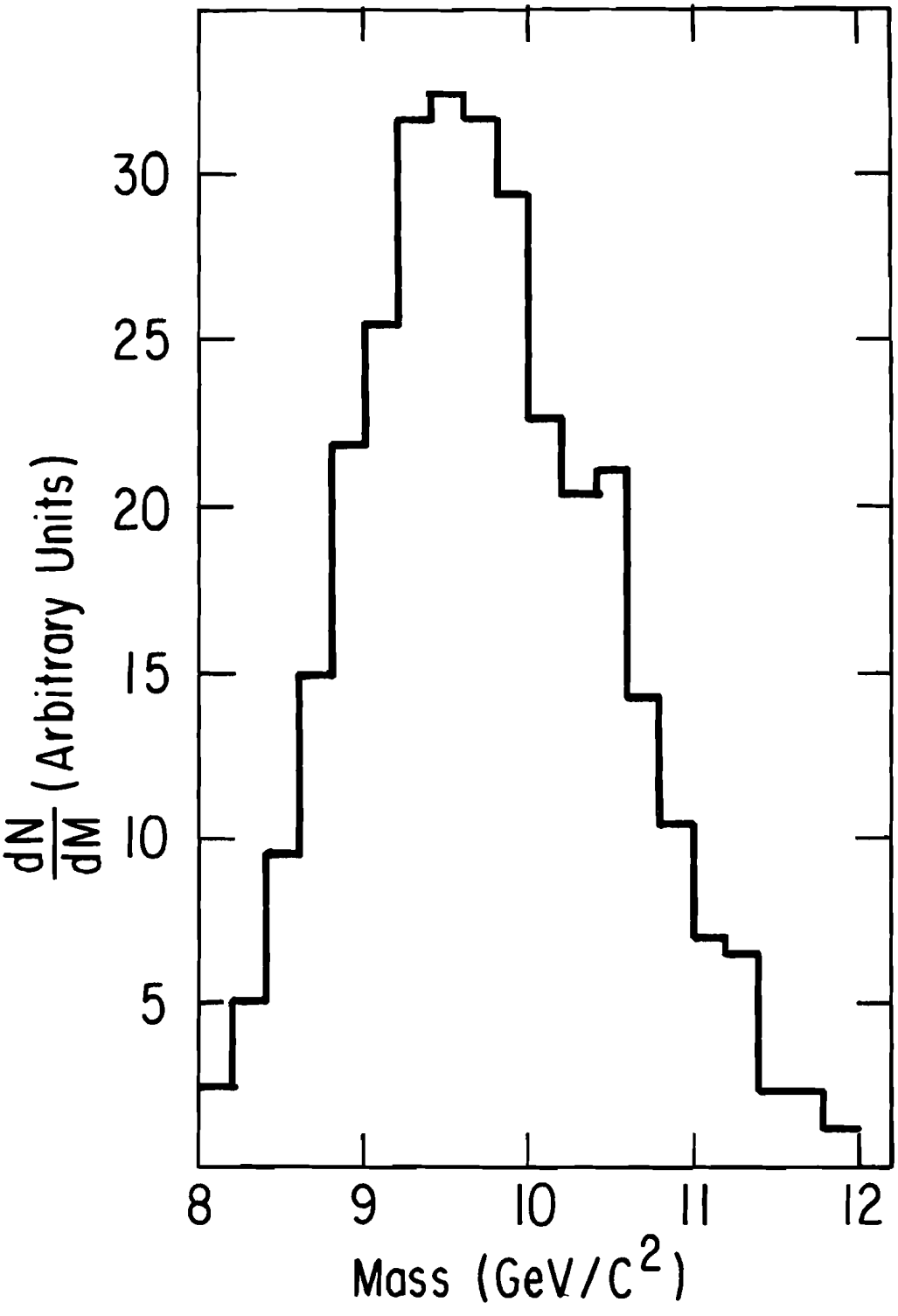
30
25
20
15
10
5
$\frac{dN}{dM}$ (Arbitrary Units)
8
9
10
11
12
Mass (GeV/C^2)

Figure 57.--The measured effective cross section per nucleon plotted against the nominal atomic mass for each target. The plotted line is the best fit to the model independent expression, equation 35.

Fig. 57

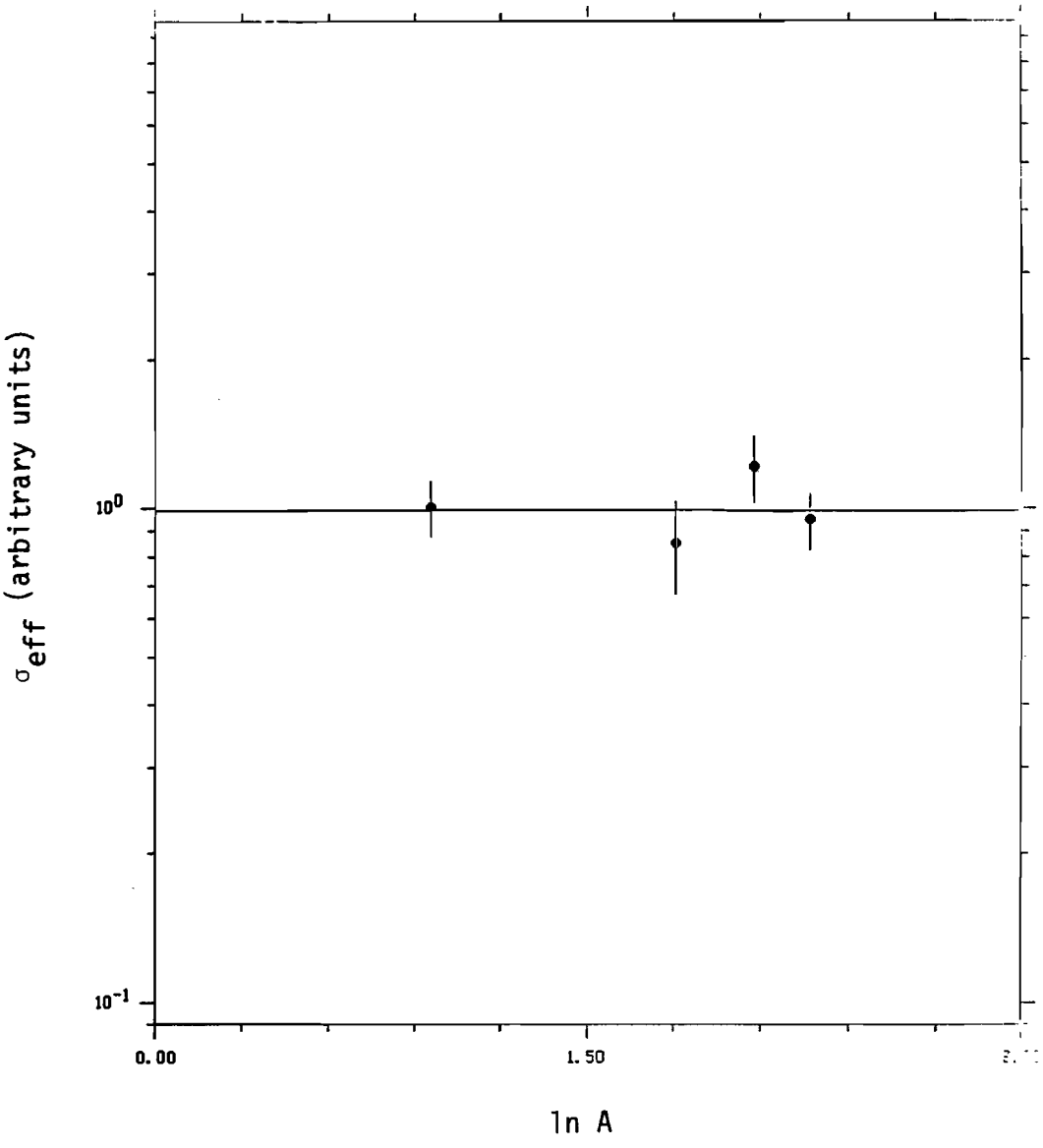

Figure 58.--A comparison of the P_T acceptances for the various targets. The Cu target acceptance has been suppressed for clarity.

Fig. 53

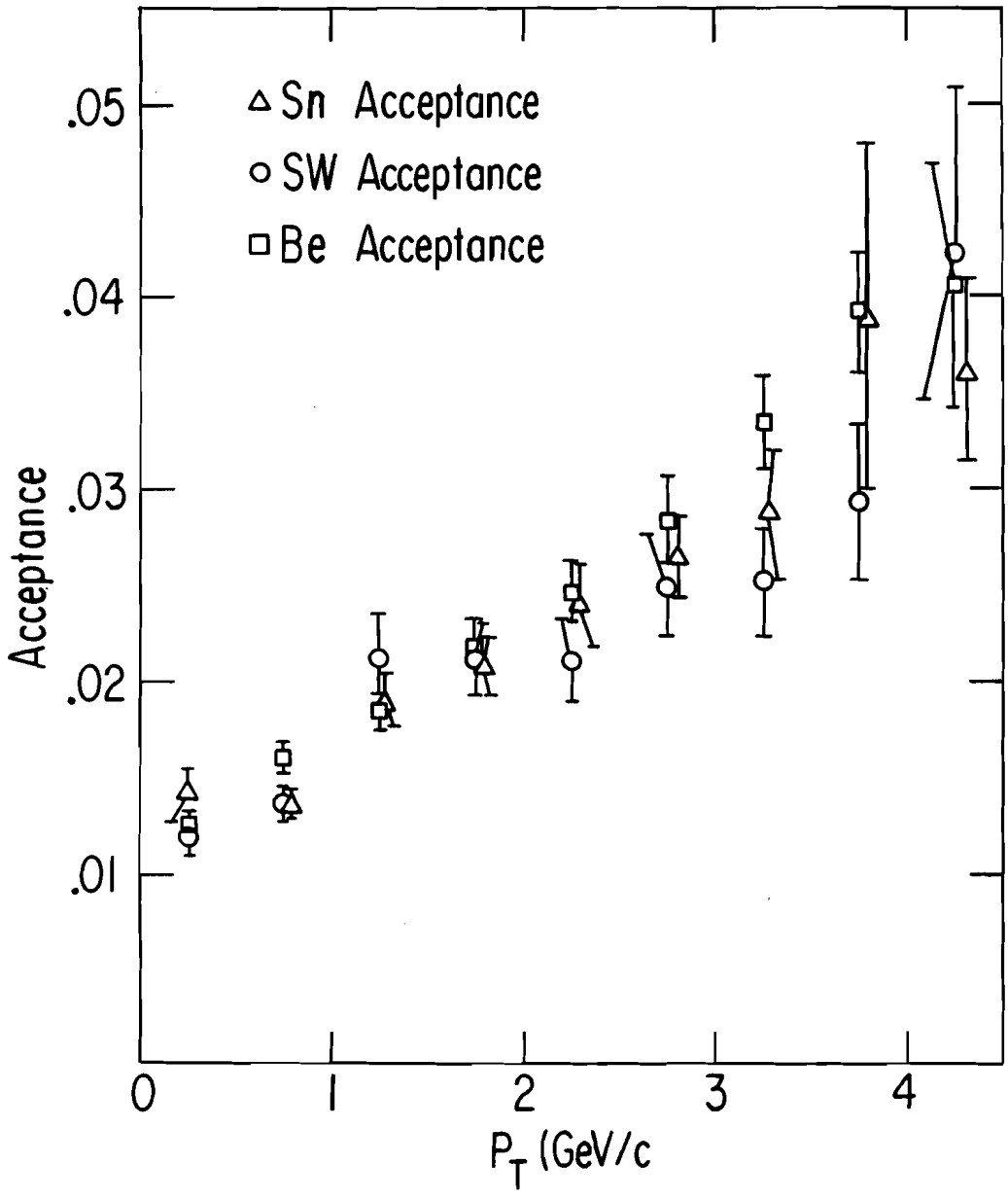
△ Sn Acceptance
○ SW Acceptance
□ Be Acceptance
.05
.04
.03
.02
.01
Acceptance
0
1
2
3
4
P_T (GeV/c

Figure 59.--The P_T acceptance is given by the data points. The "steep" and "flat" acceptance curves are one standard deviation variations in the shape. They are used to estimate the systematic uncertainties in the $\langle P_T^2 \rangle$ calculation.

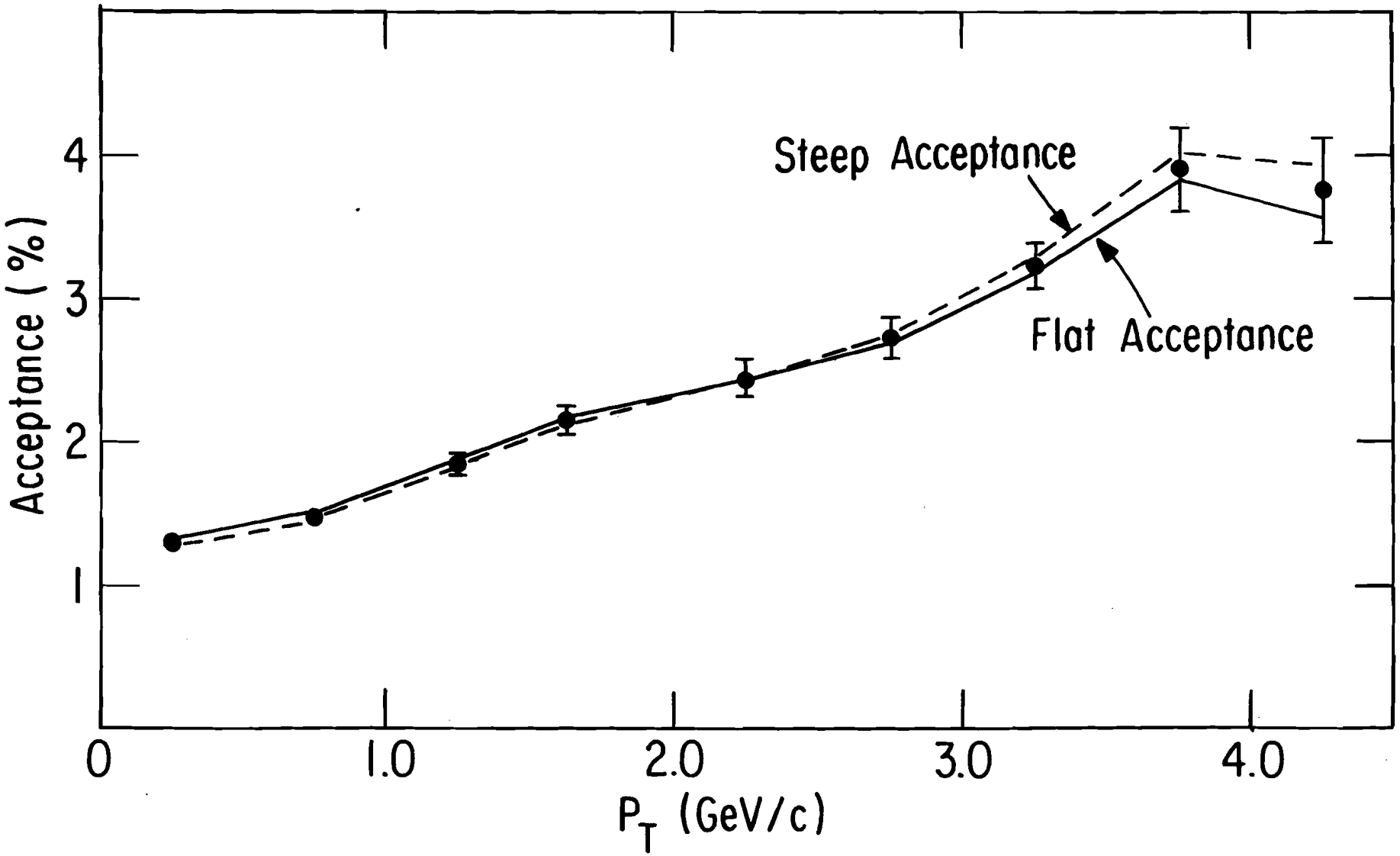
Steep Acceptance
Flat Acceptance
Acceptance (%)
1
2
3
4
0
1.0
2.0
3.0
4.0
P_T (GeV/c)

Fig. 59

Figure 60.--The calculated value of $\langle P_T^2 \rangle$ is plotted against $A^{1/3}$ for each target. The superimposed line is the result of the "constant" fit.

Fig. 60

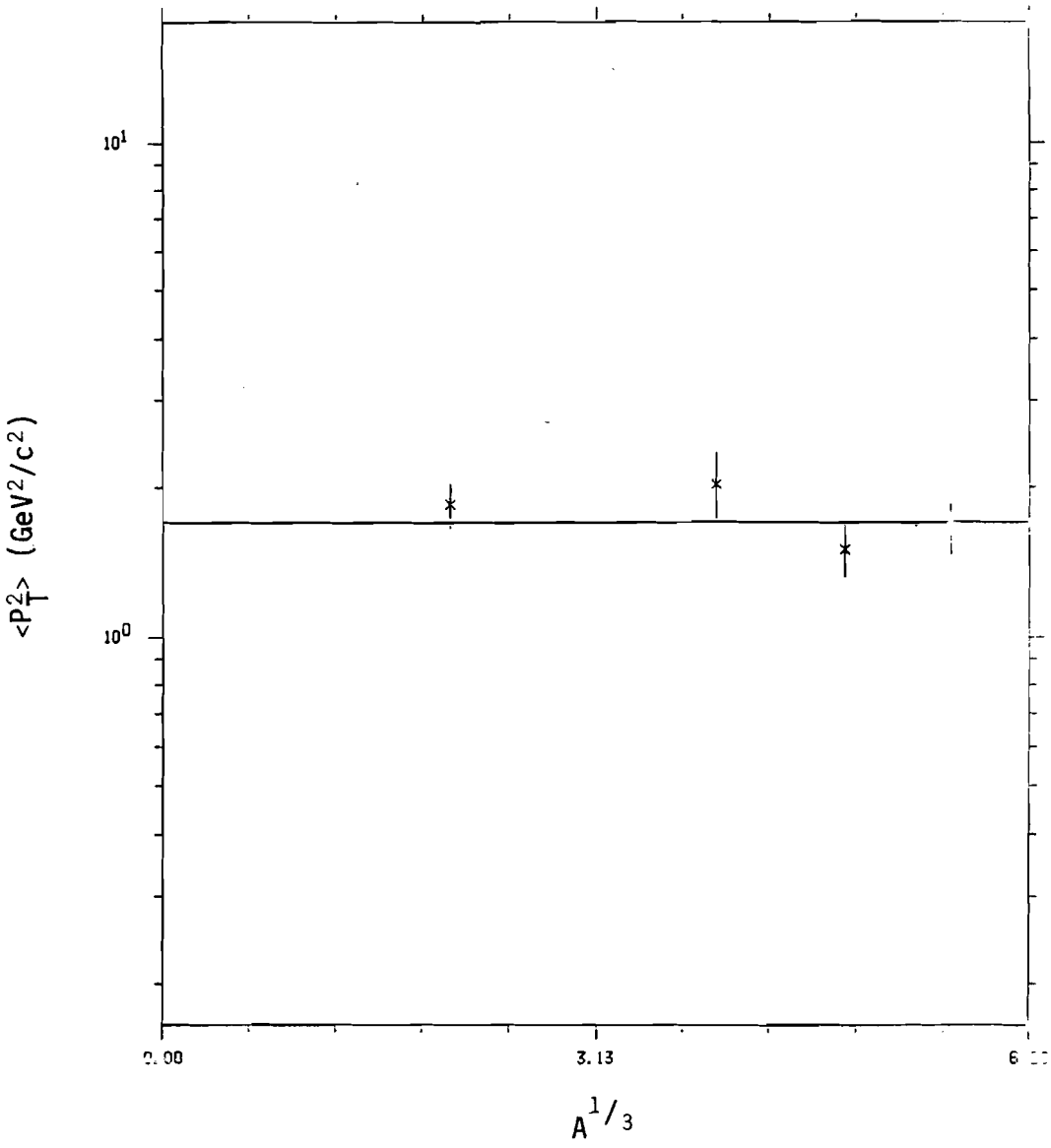

Figure 61.--A longitudinal section of the drift chambers at some plane. The geometrical conventions used in hit reconstruction are defined.

Fig. 61

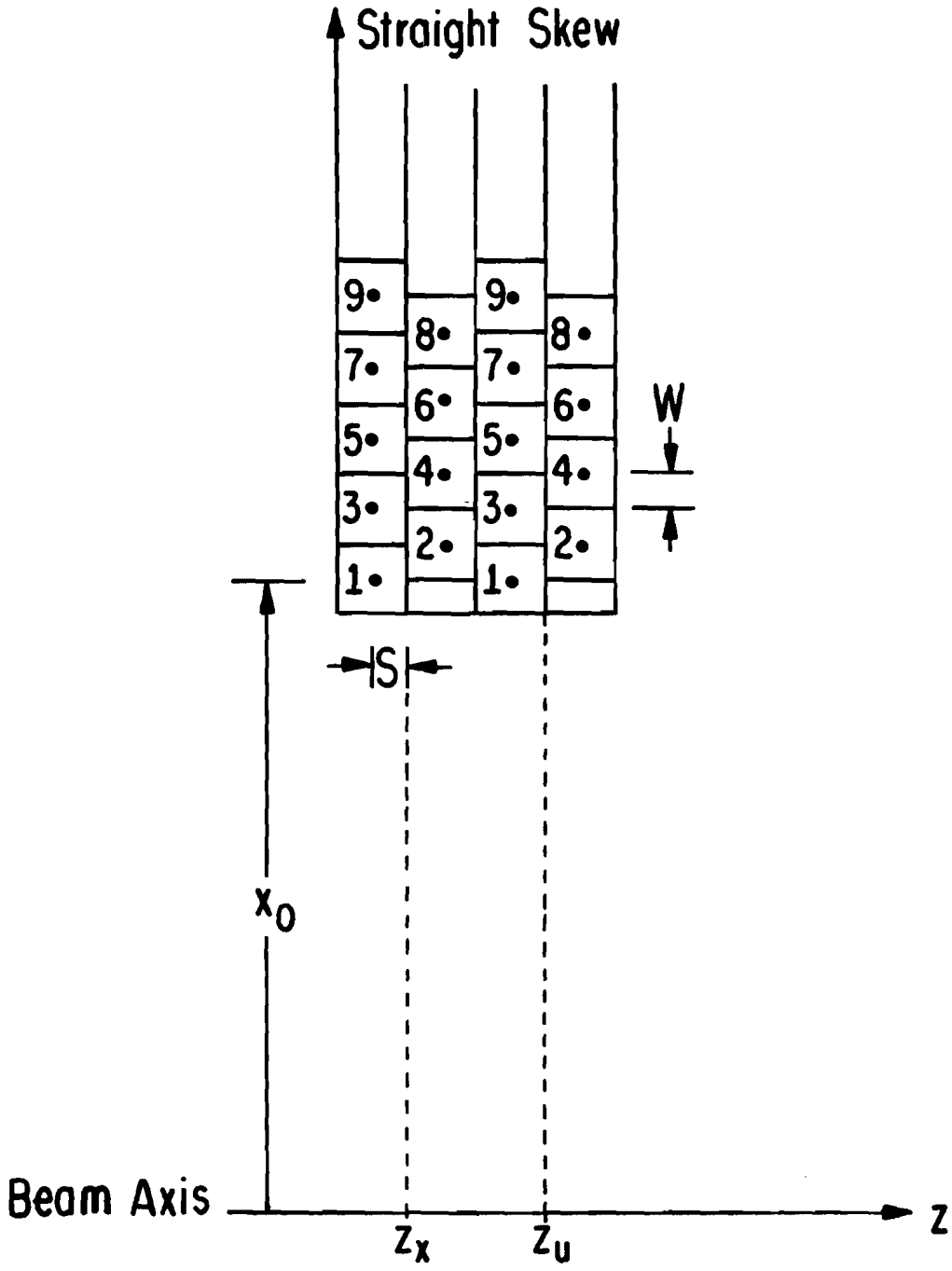

Figure 62.--The local x-u coordinate system for some octant and gap.

Fig. 62

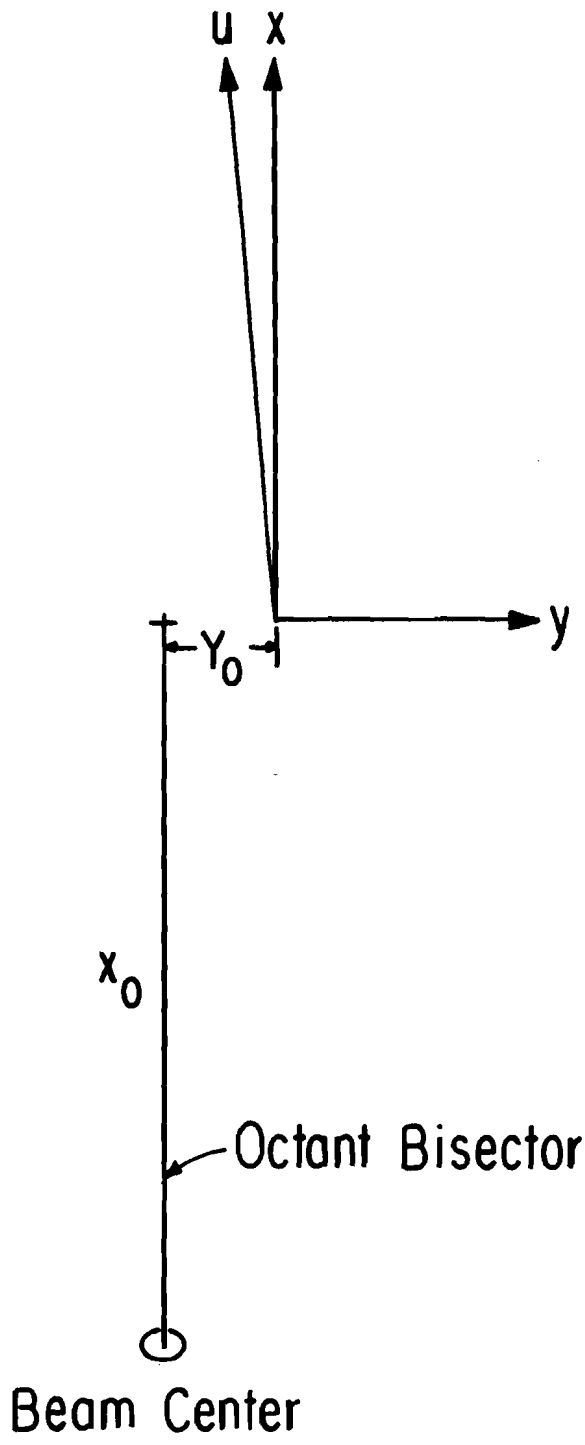

Figure 63.--The best fit of the energy loss of a free parameter in equation A9 to Monte Carlo tracks is plotted as a function of momentum. The mean and most probable values of the distribution are also plotted.

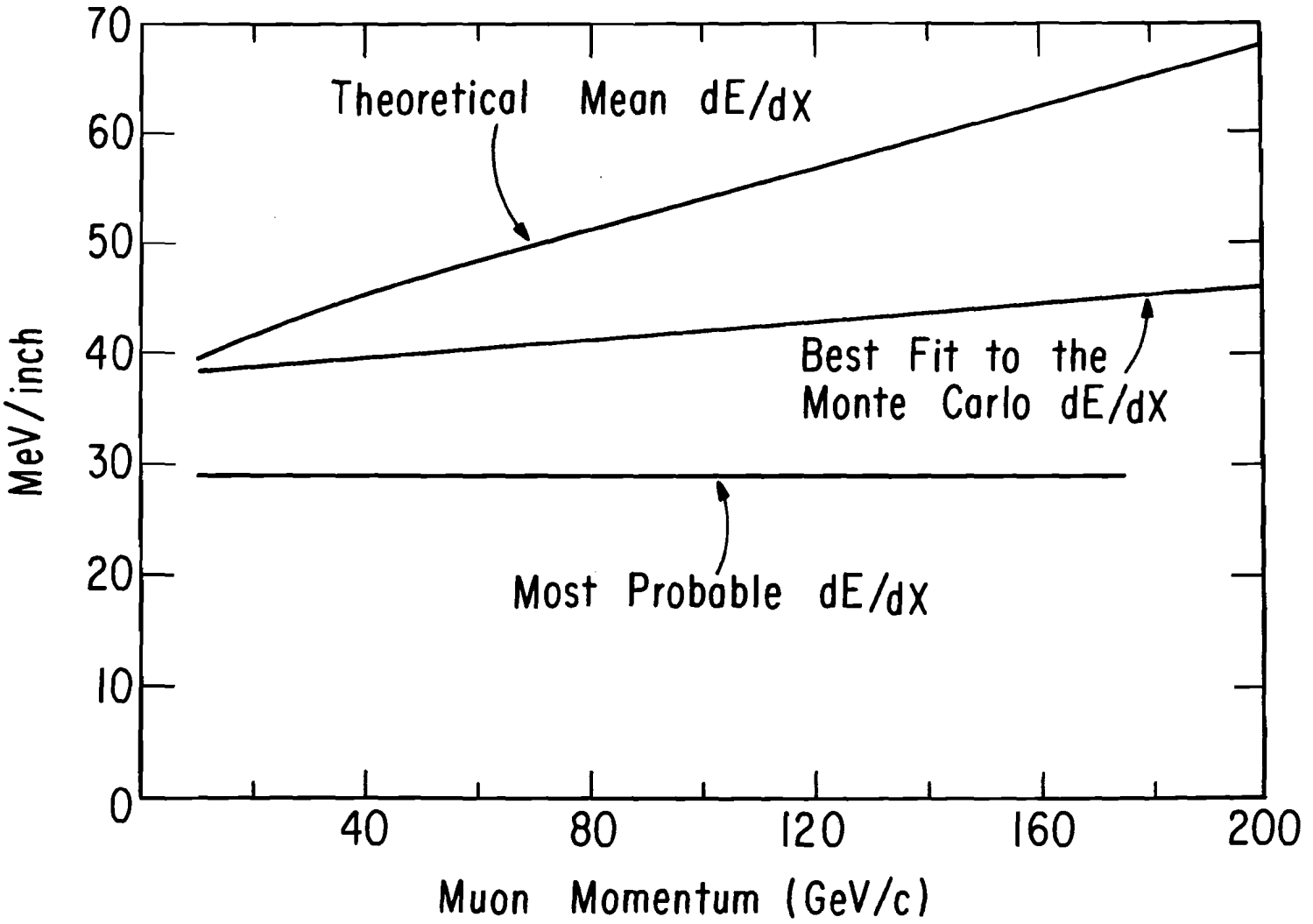
70
60
50
40
30
20
10
0
MeV/inch
Theoretical Mean dE/dX
Best Fit to the
Monte Carlo dE/dX
Most Probable dE/dX
40
80
120
160
200
Muon Momentum (GeV/c)

Fig. 63

Figure 64.--A plot of the P_T integrated inelastic plan scattering cross section for H_z is shown. A fit to the form of equation A29 is also presented.

Fig. 64

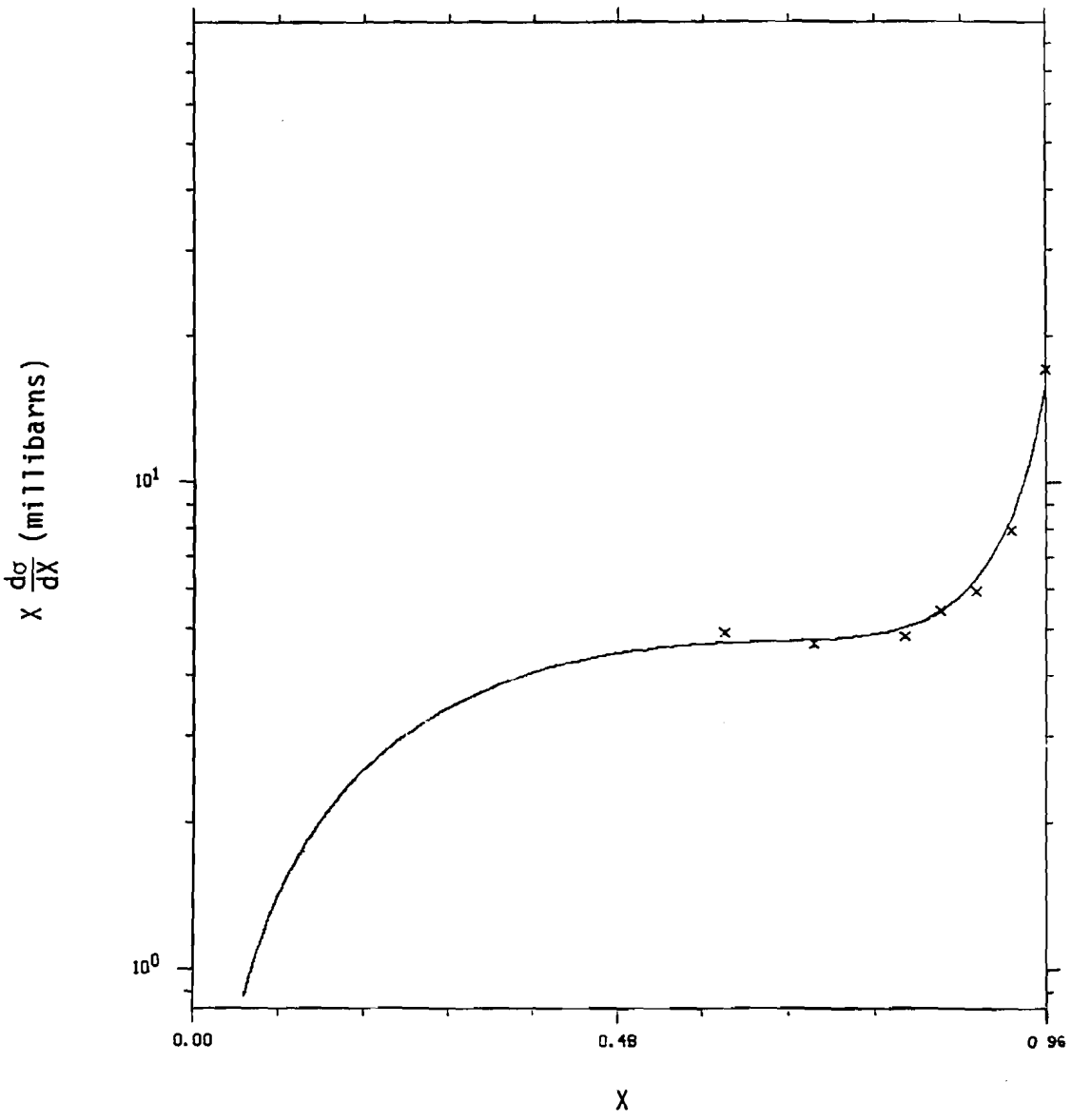

Figure 65.--The beam energy distribution for the beryllium target. The dashed curve is the incident distribution and the solid curve is the distribution at the downstream end of the target.

Fig. 65

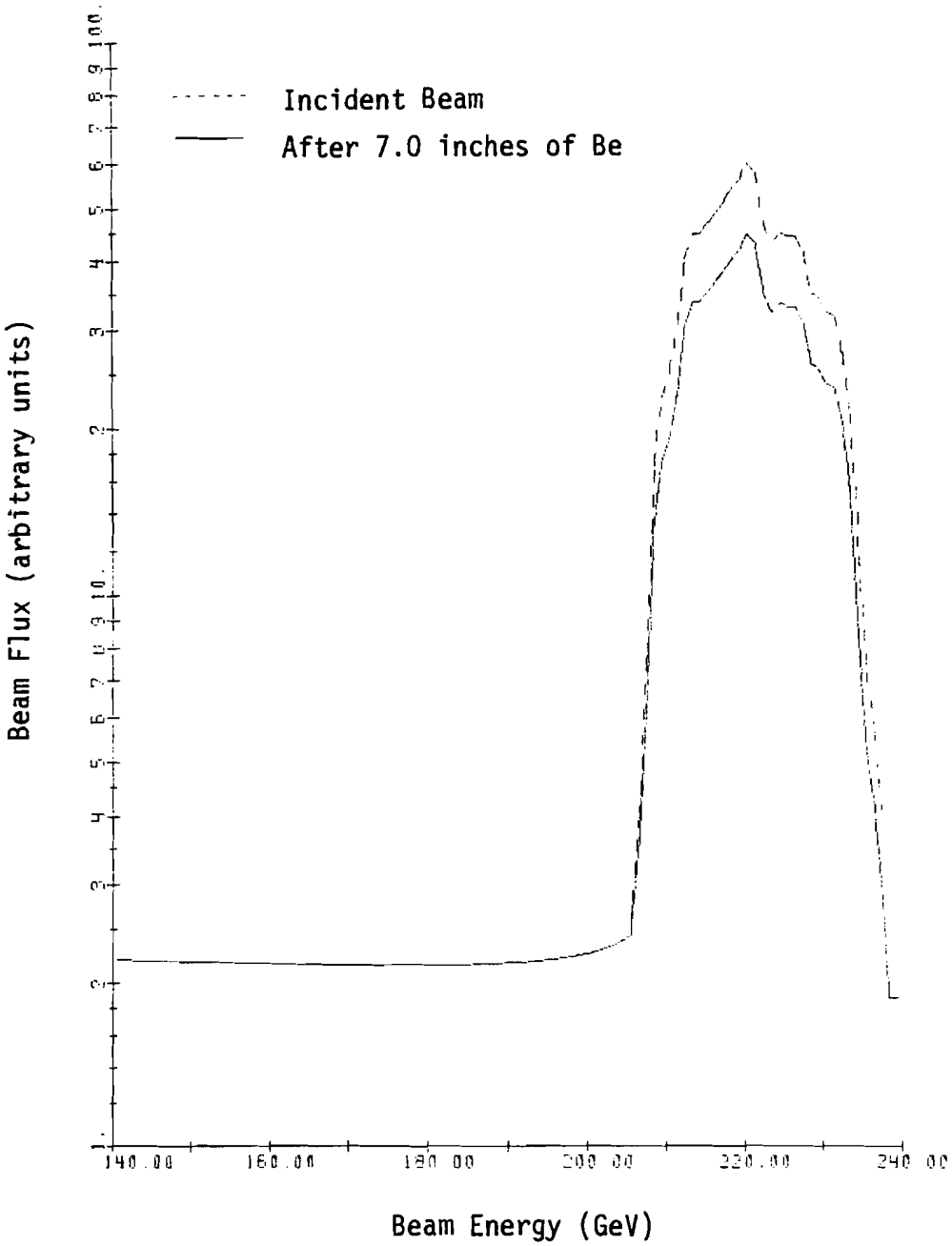
Incident Beam
After 7.0 inches of Be
Beam Flux (arbitrary units)
Beam Energy (GeV)
140.00
160.00
180.00
200.00
220.00
240.00

Figure 66.--The beam energy distribution for the tungsten target. The dashed curve is the incident distribution and the solid curve is the distribution of the downstream end of the target.

Fig. 66

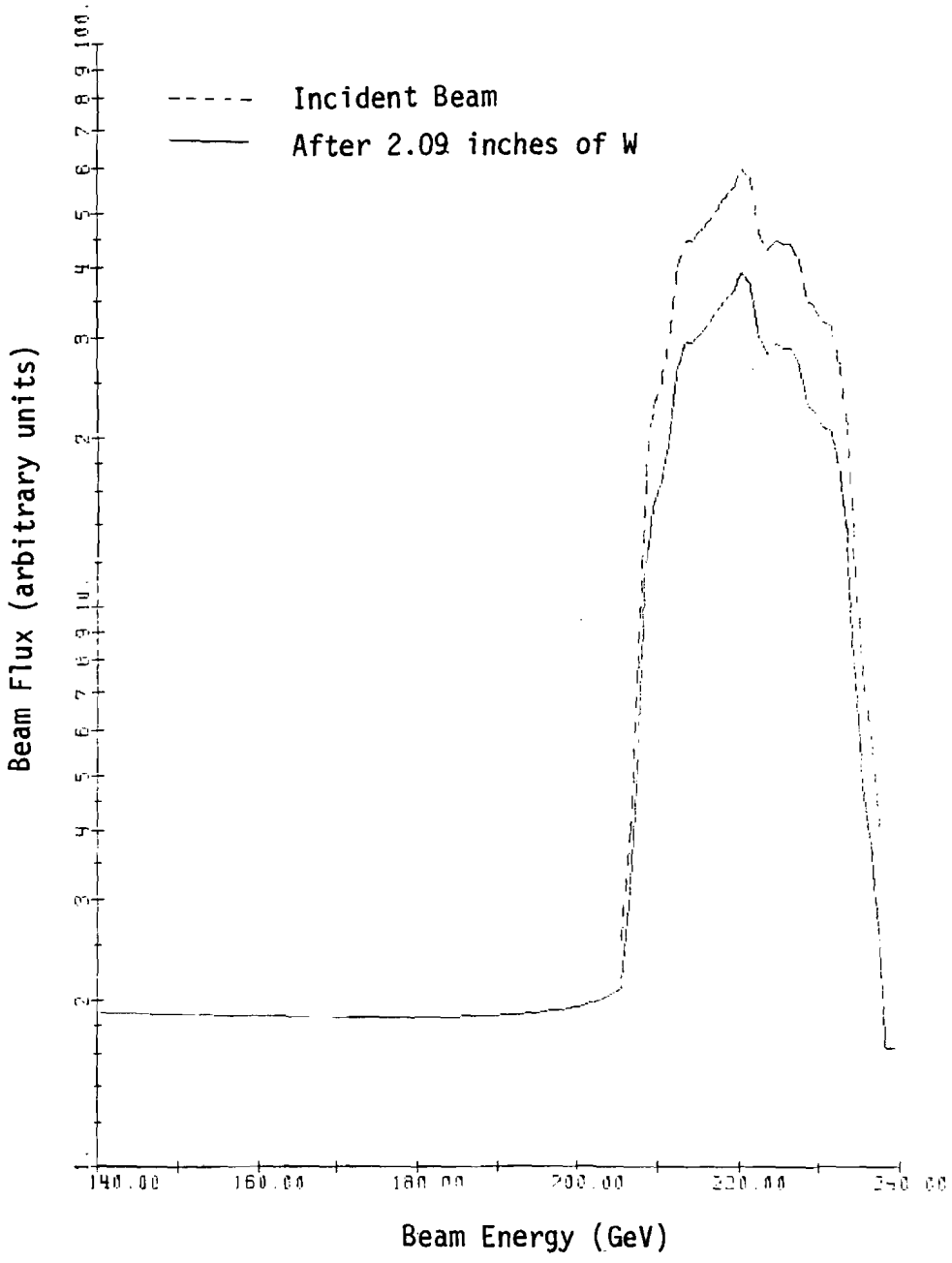
Incident Beam
After 2.09 inches of W
Beam Flux (arbitrary units)
Beam Energy (GeV)
140.00
160.00
180.00
200.00
220.00